PHILOSOPHICAL MAGAZINE

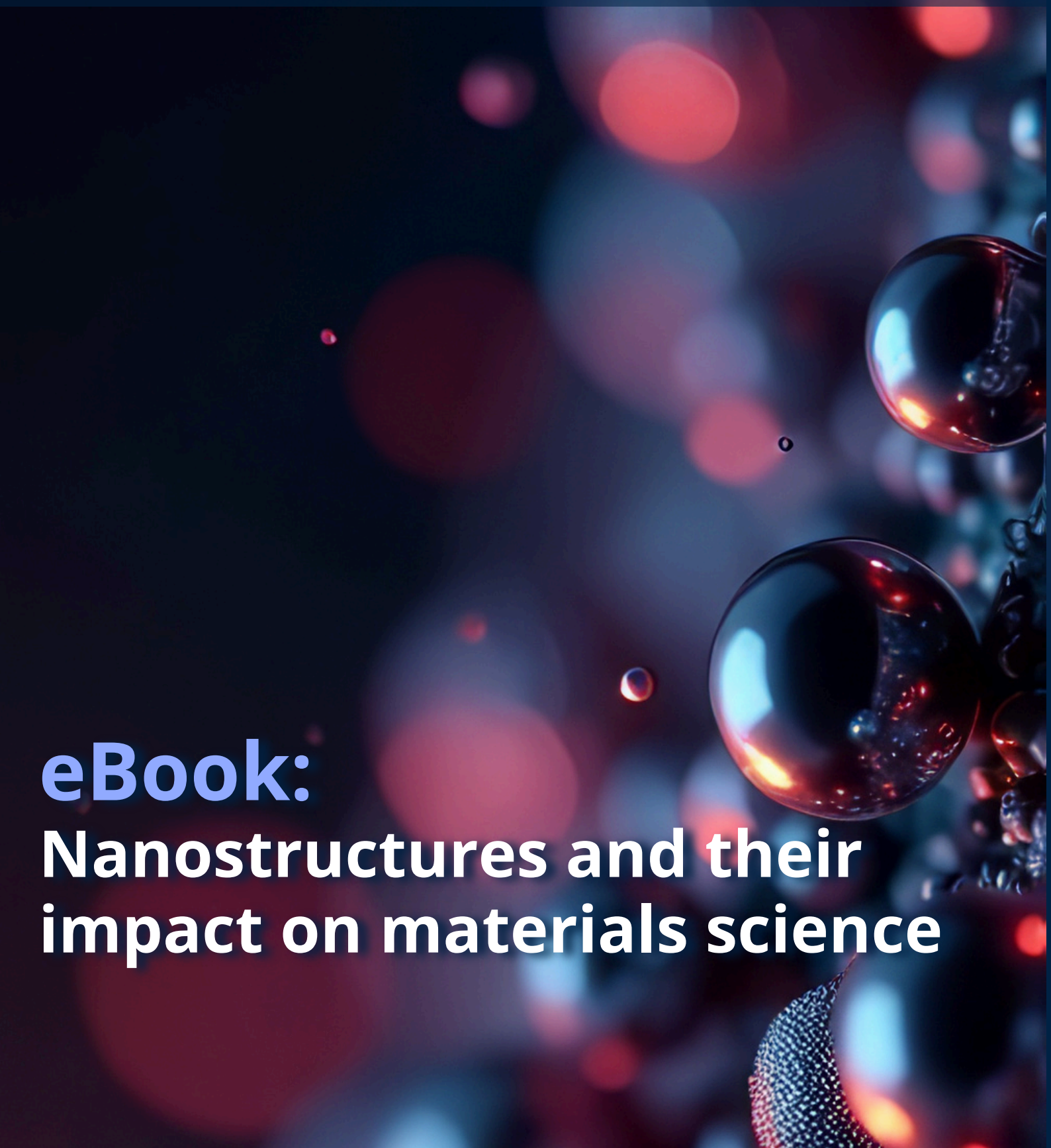

eBook:
Nanostructures and their impact on materials science

Taylor & Francis
by informa

eBook

Nanostructures and their impact on materials science

Contents

Taylor & Francis
Taylor & Francis Group

Philosophical Magazine

ISSN: 1478-6435 (Print) 1478-6443 (Online) Journal homepage: www.tandfonline.com/journals/tphm20

Evaluating the corrosion and tribological performance of nanostructured CrN/TiN and TiN/CrN configurations applied on 410 stainless steel

Zahra Afshar, Meisam Nouri, Hassan Elmkhah, Naiming Lin & Arash Fattah-alhosseini

To cite this article: Zahra Afshar, Meisam Nouri, Hassan Elmkhah, Naiming Lin & Arash Fattah-alhosseini (2024) Evaluating the corrosion and tribological performance of nanostructured CrN/TiN and TiN/CrN configurations applied on 410 stainless steel, Philosophical Magazine, 104:13-14, 590-613, DOI: 10.1080/14786435.2024.2341322

To link to this article: https://doi.org/10.1080/14786435.2024.2341322

PHILOSOPHICAL MAGAZINE
2024, VOL. 104, NOS. 13–14, 590–613
https://doi.org/10.1080/14786435.2024.2341322

Taylor & Francis
Taylor & Francis Group

Evaluating the corrosion and tribological performance of nanostructured CrN/TiN and TiN/CrN configurations applied on 410 stainless steel

Zahra Afshar[a], Meisam Nouri [a], Hassan Elmkhah[a], Naiming Lin[b] and Arash Fattah-alhosseini[a]

[a]Department of Material Engineering, Bu-Ali Sina University, Hamedan, Iran; [b]College of Materials Science and Engineering, Taiyuan University of Technology, Taiyuan, People's Republic of China

ABSTRACT

This study aims to compare the corrosion and tribological performance of TiN/CrN and CrN/TiN nanostructured multi-layer coatings deposited through cathodic arc evaporation PVD on 410-grade stainless steel. Both coating configurations were available in smooth (polished) and rough states. For the deposition of multi-layer coatings, a middle layer containing Cr and CrN was deposited to the substrate, followed by alternating nanolayers of TiN and CrN. finally, an upper layer of either CrN or TiN was applied. The nanoindentation test revealed that the hardness, Young's modulus, H/E, and H^3/E^2 ratios of the coating with a TiN upper layer were 5.57, 1.42, 3.86, and 85.39 times of the substrate, respectively. At the coating with CrN upper layer, these values were 4.04, 1.13, 3.53, and 51.68 times of the substrate, respectively. Results showed that increasing the H/E and H^3/E^2 ratios increased wear resistance. Wear rates of smooth and rough TiN coatings and smooth and rough CrN coatings were reduced by 86%, 99%, 53%, and 26%, respectively, compared to the substrate. Results of the corrosion test showed that the rough CrN coating had greater corrosion resistance than the coating with a TiN upper layer and the substrate due to its higher hydrophobicity.

ARTICLE HISTORY
Received 10 November 2023
Accepted 26 January 2024

KEYWORDS
Roughness; TiN/CrN nanostructure coating; CAE-PVD; wear properties; corrosion properties

1. Introduction

Stainless steels are an important group of steels, the main alloying elements of which are nickel and chromium [1]. Among these alloys are 410 stainless steels, which exhibit beneficial in-service properties such as quench-ability, high strength and toughness, and strong resistance to wear and corrosion [2,3]. One of the important applications of 410 stainless steel is in producing turbine blades [4]. A significant issue for turbine blades is their exposure to

CONTACT Meisam Nouri m.nouri@basu.ac.ir Department of Material Engineering, Bu-Ali Sina University, Hamedan 65178-38695, Iran

This article has been corrected with minor changes. These changes do not impact the academic content of the article.

the destructive phenomena of wear and corrosion, which greatly affect the performance and service life of the parts [5,6]. In order to solve this challenge, various coatings can be used to prevent surface damage to 410 stainless steels [7]. By using coating techniques, it is possible to deposit a wide range of single-layer and multi-layer coatings, such as nitride coatings, on the surface of the parts [8,9]. Physical vapour deposition (PVD) using cathodic arc evaporation is a superior coating deposition method due to its low deposition temperature, high deposition speed, ability to create coatings with various structures and architectures, creating coatings with good adhesion to the substrate, providing coatings with high density, and the ability to control the thickness of the coatings and is commercially used for the deposition of hard nitride coatings [10].

TiN and CrN single-layer nitride coatings are widely used in industries such as machining and cutting tools [11,12] due to high hardness, good wear and corrosion resistance and their properties have been studied by researchers [13,14]. It has been shown that although TiN coating has relatively good mechanical properties and thermal stability, it is easily oxidised to TiO_2 when exposed to temperatures above 500°C, leading to the formation of cracks in the coating layer. Meanwhile, CrN coating is softer and tougher than TiN coating, and due to the formation of a dense protective layer of Cr_2O_3 on its surface, it has better oxidation resistance than TiN coating. However, when CrN coating is exposed to temperatures above 800°C, its mechanical strength decreases due to the loss of nitrogen [15]. In other words, the CrN coating undergoes thermal decomposition, and the decomposition pathway includes two main reactions: CrN converting to Cr_2N and subsequently, Cr_2N converting to Cr through the simultaneous loss of nitrogen [16]. To improve mechanical properties and resistance to erosion, corrosion, and wear, researchers are working on coatings with greater performance. It has been shown that the multi-layer architecture of the coating can significantly improve mechanical, chemical, and tribological properties [17,18]. In a multi-layer coating, each layer exhibits its specific properties, such as thermal blocking, adhesion to the substrate, load-bearing, lubrication, or wear resistance [15].

Lotfi-Khojasteh et al. [19] applied a TiN/CrN nanolayer coating to a H13 carburised hot-deformed substrate using PVD with cathodic arc evaporation and studied the corrosion and tribological performance of the coating. Results showed that the coated sample had the lowest friction factor and wear loss compared to the uncoated substrate, which was attributed to the high hardness of the coated sample, the strong bonding of the coating to the substrate, and the different nature of the coating and rubbing pin. Pogrebnjak et al. [20] investigated the structure and properties of binary nitride coatings and found that as the H/E^{*} and $H3/E^{*2}$ ratios increased, the friction coefficient and wear rate of the TiN/CrN coated sample

decreased. Kolaklieva et al. [21] investigated the physical and wear characteristics of a CrN/TiN multi-layer coating applied by sputtering on an HSS substrate. Results showed that the presence of a large number of phase interfaces in the CrN/TiN coating led to an increase in hardness, crack deflection, and dissipation of defects and crack energy, which improved the tribological behaviour.

Olia et al. [22] investigated the corrosion and wear performance of TiN and CrN coatings applied to UNS S17400 stainless steel. Results showed that, in general, the use of nitride coatings improved the chemical stability of stainless steel. Additionally, the corrodibility of the CrN coating was greater than that of the TiN coating. Faghani et al. [23] studied the corrosion behaviour of a steel substrate, TiN and CrN coatings, and a TiN/CrN nanoscale multi-layer coating in Ringer's solution. Results showed that the coated samples had better corrosion resistance against chloride ions, meaning that the coatings shifted the corrosion potential to more positive values and provided greater protection for the substrate against corrosion. The corrosion resistance of the CrN monolayer coating was also better, due to its dense structure with fewer cracks, which prevented the corrosion solution from penetrating the substrate. Forouzanmehr et al. [24] investigated the corrosion behaviour of TiN and CrN coatings deposited by the CAE-PVD method on 410 stainless steel in Ringer's solution. Their results showed that the CrN coating had the lowest corrosion rate and the greatest corrosion resistance. The higher corrosion performance of the CrN coating is due to surface activities and the formation of layers in contact with the electrolyte solution, which slows down electrochemical reactions. Therefore, according to the studies conducted to investigate the corrosion and wear properties of single-layer or multi-layer TiN and CrN coatings, it was observed that these coatings have significantly higher resistance to wear and corrosion. Despite the studies conducted on the properties of these coatings, little information is available regarding the effect of the chemical composition and surface roughness of the coating on corrosion [25,26] and wear properties [27]. Research has shown that surface roughness can have different effects on the surface properties of a material, in some situations, smooth surfaces perform better while in others, rough surfaces work better. Additionally, the properties of a multi-layer coating are greatly influenced by the composition of the upper layer, which is in contact with the service environment [28,29].

Therefore, considering the lack of knowledge about the effect of surface roughness and chemical composition on the surface properties of TiN and CrN coatings, the aim of the current research is to compare the tribological and corrosion performance of two TiN/CrN nanostructured multi-layer coatings deposited by CAE-PVD on a 410 stainless steel substrate, which have different surface roughness and TiN or CrN upper layers.

2. Experimental methods

2.1. Sample preparation and coating process

The 410 stainless steel was used as the coating substrate. The composition of these pieces is presented in Table 1. Figure 1 shows a schematic of the research process. To evaluate the wear and corrosion behaviour of the steel, disc-shaped samples with an approximate diameter of 33 mm and a thickness of 4 mm were prepared. The samples were wet ground using SiC papers with grits ranging from 60 to 2000. After preparing the samples, TiN/CrN nanostructured multi-layer coatings were applied using the cathodic arc evaporation method in two types: with TiN as the upper layer and with CrN as the upper layer. In the deposition of multi-layer coatings, a middle layer containing Cr and CrN was applied to the substrate, followed by alternating nanolayers of TiN and CrN, and finally, an upper layer of either CrN or TiN was applied. Table 2 shows the deposition conditions of the coatings. After the deposition of the coatings, half of the coated specimens were polished to study the effect of roughness. Figure 1 shows a schematic of TiN/CrN nanostructured coatings with TiN and CrN upper layers, with smooth and rough surfaces. To present the test results for the samples, the abbreviations introduced in Figure 1 have been used. In cases where the test result does not depend on surface roughness, only the TiN or CrN symbol is used. In this sense, the TiN symbol refers to the TiN/CrN bilayer coating with a TiN upper layer, and the CrN symbol refers to the TiN/CrN bilayer coating with a CrN upper layer.

2.2. Characterisation of the coatings

To distinguish different compounds in the coatings, an XRD instrument (Bruker D8 advance) was used in the angular range of 30–90 degrees at a scan speed of 0.05°/sec. Cu-Kα radiation (λ = 0.154 nm) was used as the incident beam. A JEOL JSM-840A SEM and a FESEM MIRA3 were used to examine the morphology of the coating surface and cross-section, respectively. The adhesion of the coatings to the substrate was evaluated using a Rockwell tester in accordance with the VDI 3198 standard, with an applied force of 588 N (equivalent to 60 kgf) and a test duration of 35 s. To measure the roughness of the substrate and coatings, a PCE RT2200-Roughness tester was used.

To measure the wettability of the surfaces, a CAG-20 wettability device equipped with a camera and a syringe with an external diameter of 700 μm was used to inject distilled water. During the test, the ambient

Table 1. Chemical composition of 410 stainless steel used in the research.

Element	Fe	Cr	Ni	Si	Mn	C	Cu	W	*P*	Mo	V	Co
wt. %	85.7	12.4	0.5	0.437	0.433	0.112	0.09	0.05	0.04	0.03	0.02	0.02

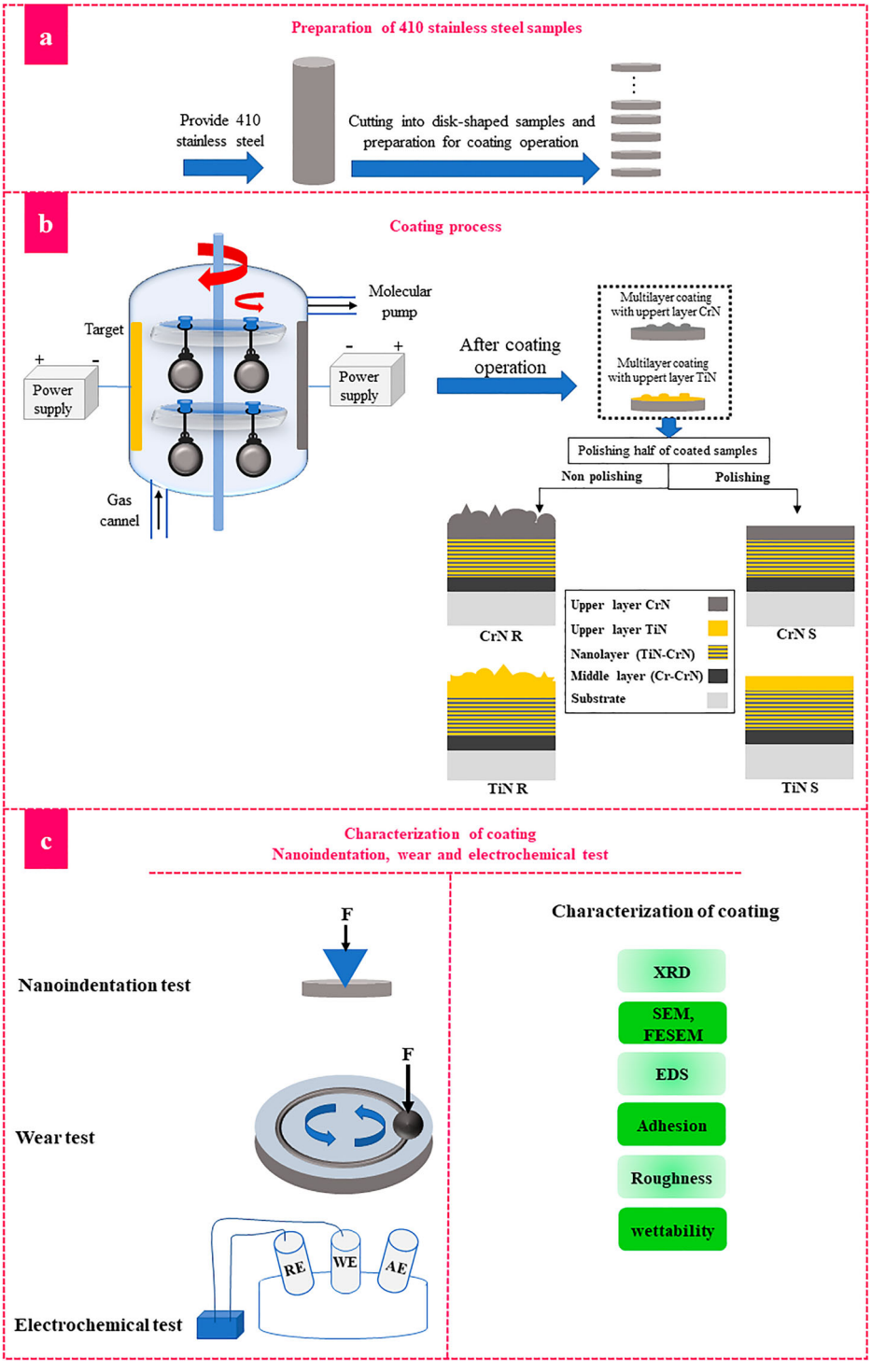

Figure 1. Schematic diagram of the experimental process: (a) sample preparation process, (b) deposition process, and (c) characterization, nanoindentation, wear and corrosion tests.

Table 2. Deposition conditions of the deposited TiN/CrN bilayer coatings.

Coating parameters	Upper layer CrN, Upper layer TiN
Target material	Cr (99.6%), Ti (99.7%)
Samples rotating rate (rpm)	5
Distance target-substrate (cm)	15
Working pressure (Pa)	0.67
Deposition temperature (°C)	300
Target evaporation current (A)	130
Deposition time (min)	120
Substrate bias voltage (V)	−100
Duty cycle (%)	50

temperature was 25 °C, the pressure was 88 kPa, the humidity was 33%, and the fluid injection speed was 0.2 μm/s. To ensure the repeatability of the test, it was performed three times on each sample. The images were analyzed using ImageJ software.

2.3. Mechanical and tribological evaluation

A nanoindentation instrument (Hysitron Inc. Triboscope) was used to determine the hardness and Young's modulus of the substrate and polished coatings. To achieve accurate results, the measurement was performed on specimens with smooth surfaces. The applied force was 10 mN and the creep time was 10 s. The loading and unloading times were 30 s, and for each specimen, the measurement was repeated 5 times. A ball-on-disk sliding wear tester was used to perform wear tests in dry mode. A normal load of 5 N was applied to a 6 mm diameter alumina ball to rub over the surface of the specimens at a linear speed of 0.1 m/s. The sliding distance was 300 m and the resulting wear scars had a radius of 13 mm. The weight loss was measured with a digital scale with an accuracy of 1×10^{-4} g.

2.4. Electrochemical test

The corrosion behaviour of the substrate and coatings was investigated through potentiodynamic polarisation and EIS tests in a 3.5 wt.% NaCl solution. Before performing the corrosion tests, the samples were immersed in a sodium chloride solution for 2 hours to measure the open circuit potential. The specimens were tested in a standard three-electrode flat cell, with the examined specimens serving as working electrodes, silver/silver chloride serving as reference electrodes, and platinum electrodes serving as auxiliary electrodes. NOVA 2.1 software was used to analyze the corrosion test results. Potentiodynamic polarisation experiments were carried out at a rate of 1 mm/s, while EIS testing was carried out at a frequency range of 10 mHz to 10 kHz and a wavelength range of 10 mV (in open circuit potential).

3. Results and discussion

3.1. Microstructure and phases

Figure 2 represents the X-ray diffraction (XRD) patterns of the coated specimens. Both coatings with FCC crystal structures have (111), (200), and (311) diffraction peaks. The TiN and CrN phases shown in the XRD patterns correspond to the reference pattern numbers 00-019-0323, 00-038-1420, and 01-076-2494, respectively. The peak related to the substrate is also observed and the reason for this is that the thickness of the coating is a few micrometers (TiN and CrN coatings thickness are 6.1 and 5.56 μm, respectively) and due to the small thickness of the coating, the incident beam penetrated the substrate and therefore, the diffracted beam by the substrate was observed in the XRD pattern. From the higher magnification of the diffraction pattern, it is observed that the diffraction peaks of the (200) plane corresponding to the two phases of TiN and CrN, instead of appearing separate from each other, have overlaps, which indicates the nanolayer structure of the coatings. It is also observed that the diffraction peaks in the TiN coating are shifted to smaller angles compared to the CrN coating, and this could be attributed to the smaller lattice parameter of the phases in the CrN coating compared to the TiN coating. The smaller lattice parameter in the CrN coating indicates a higher density of this coating compared to the TiN coating and the difference in the density could result in different properties of the coatings. In other words, the chemical

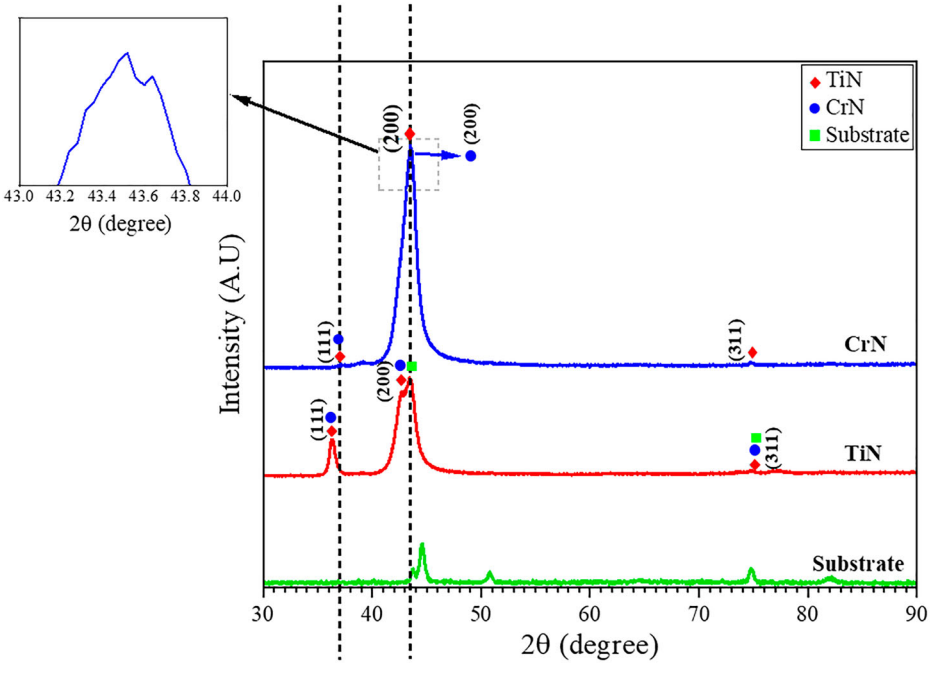

Figure 2. XRD plots of TiN S and CrN S coated samples.

composition of the top layer of the coating has an influence on the lattice parameters and thus on the properties [22,30].

3.2. Surface morphology and adhesion of the coatings

Figure 3 (a-d) displays the SEM images of the surface of TiN S, TiN R, CrN S, and CrN R specimens. The black dots represent voids on the coating surface (thin yellow arrows in Figure 3) and the white dots on rough samples represent macroparticles on the coating surface (thick red arrows in Figure 3). The white

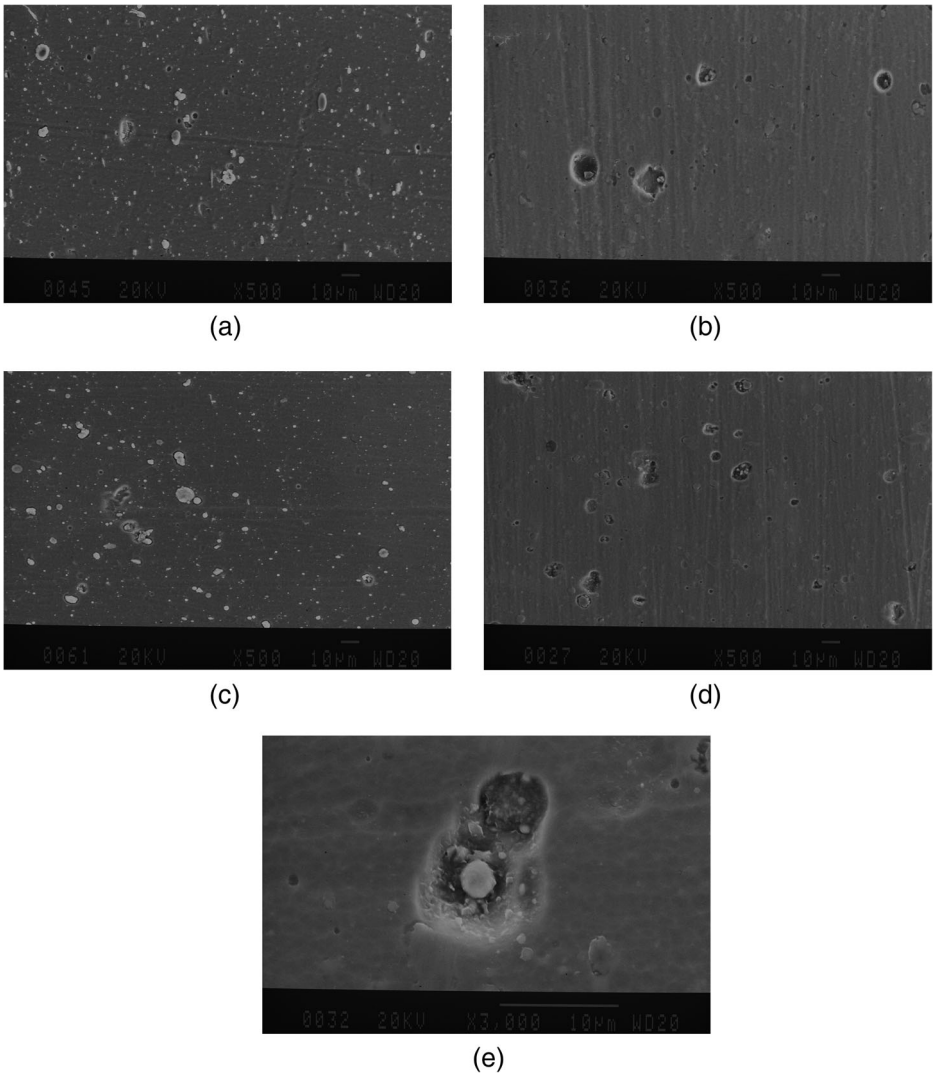

Figure 3. SEM images from the surface of the coating: (a) TiN R, (b) TiN S, (c) CrN R, (d) CrN S (×500) Thin arrows indicate voids and thick arrows indicate macroparticles, and (e) the effect left by removal of macroparticles from the surface of CrN coating (×3000).

colour of the macroparticles in the SEM images describes that they are in the shape of protrusions and bulges. The presence of macroparticles and holes is a well-known characteristic of cathodic arc evaporation method [31,32]. As can be seen, in general, the amount of fine and coarse macroparticles in CrN R coating is more than that of TiN R. According to Figure 3, it can be seen that in the smooth specimens (TiN S and CrN S), the macroparticles have been largely removed from the surface of the coating as the result of polishing. The SEM image of the surface defect of the CrN specimen after being polished (CrN S) at the magnification of 3000x is shown in Figure 3(e). As can be seen, the macroparticles have been rubbed off and the debris has filled the holes.

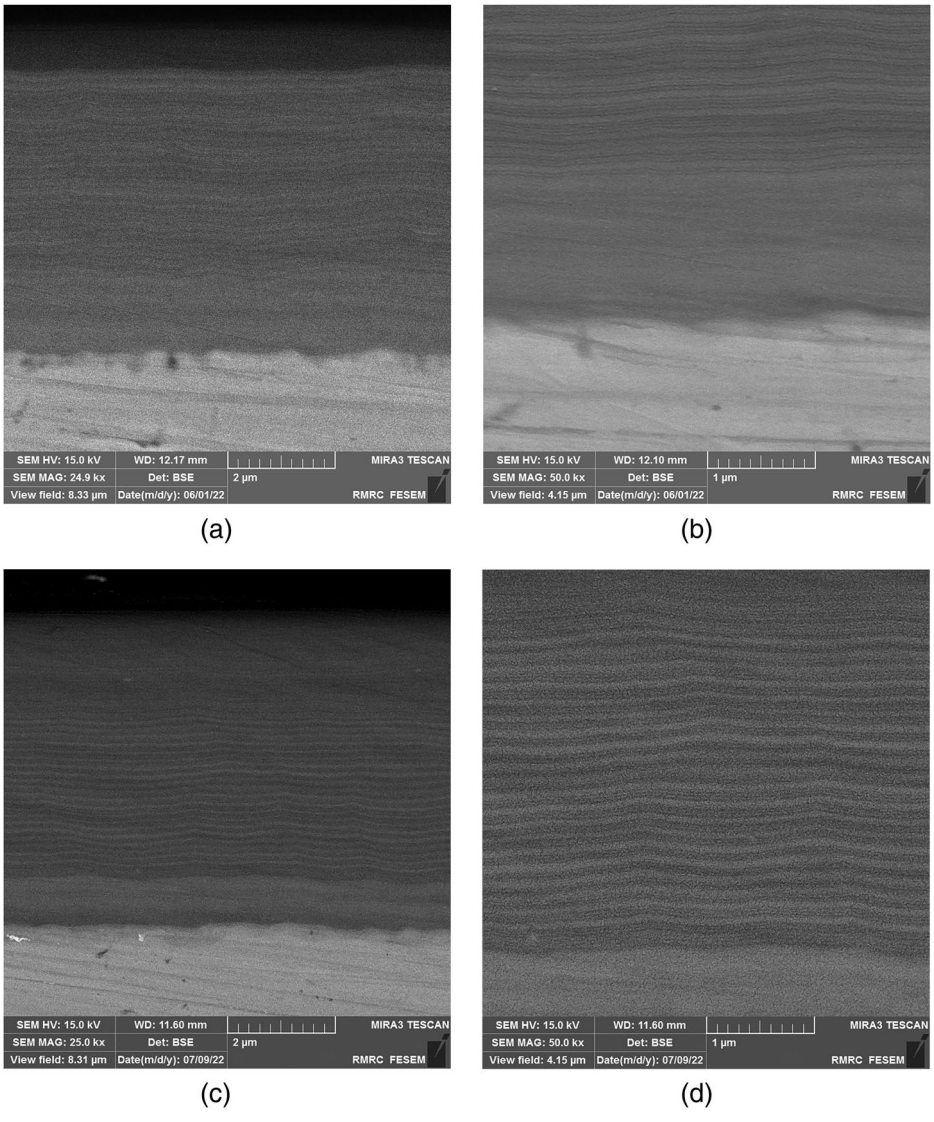

Figure 4. FESEM cross-section images of the coatings in two different magnifications: (a,b) TiN and (c,d) CrN.

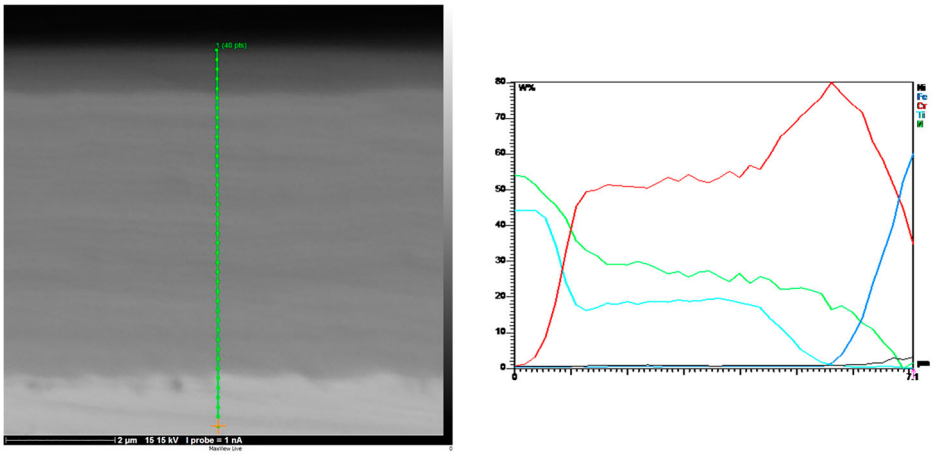

(a)

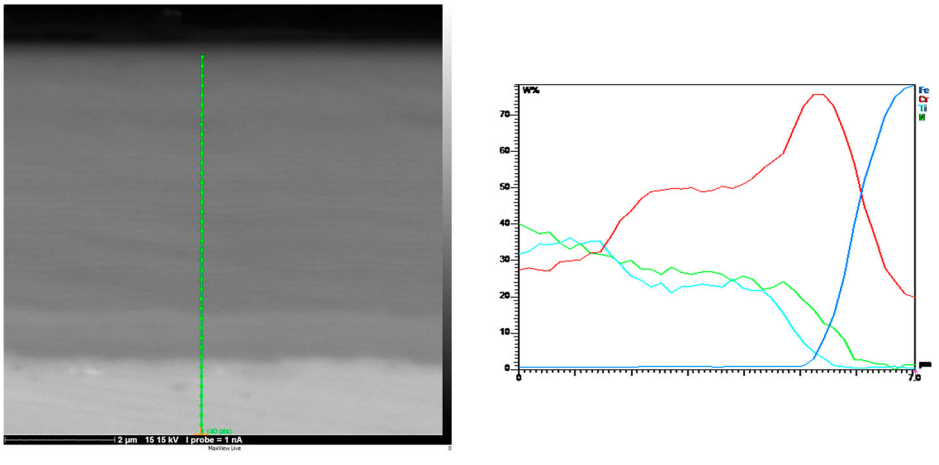

(b)

Figure 5. Linear elemental analysis and FESEM micrographs of (a) TiN coating and (b) CrN coating.

The FESEM images obtained from the cross-section of the coatings and the line scan analysis are presented in Figures 4 and 5. As can be seen, both coatings are composed of several layers. The total thickness of the TiN coating specimen is 6.1 µm and for the CrN coating specimen, it is 5.56 µm. As can be demonstrated, there is no disbonding between the substrate and the coating which implies an excellent adhesion of the coating layer to the substrate. It can also be seen that both coatings consist of three different sections. The first section is the upper layer of each coating. For the TiN coating, the upper layer is rich of Ti and for the CrN coating, the upper layer is enriched by Cr. The second section is the multi-layer section which is composed of sequential TiN and CrN nanolayers. The third section is the middle layer which contains

Table 3. Surface roughness parameters values of substrate, TiN S, TiN R, CrN S and CrN R coatings.

	Substrate	TiN S	TiN R	CrN S	CrN R
R_a (μm)	0.05 ± 0.02	0.09 ± 0.01	0.37 ± 0.02	0.13 ± 0.03	0.47 ± 0.04
R_z (μm)	0.45 ± 0.06	1.2 ± 0.3	4.86 ± 1.15	1.83 ± 0.5	3.89 ± 0.3
R_q (μm)	0.07 ± 0.03	0.14 ± 0.02	0.53 ± 0.06	0.23 ± 0.08	0.59 ± 0.04

Cr and CrN. Therefore, it is safe to say that the main difference between the two coatings is only in their upper layers.

The measured roughness parameters of the substrate and the coatings are reported in Table 3. In addition, the Rockwell adhesion test results for TiN and CrN coatings are shown in Figure 6. According to the VDI 3198 standard, the adhesion of both coatings is in the HF1 class, which is acceptable [10,31].

3.3. Mechanical properties

Figure 7 (a,b) shows the force-displacement diagram obtained from the nanoindentation test and AFM images after the indentation for the TiN coating, the CrN coating, and the substrate. As can be seen, the highest displacement (the highest indentation depth) is for the substrate and then the CrN coating and the lowest indentation depth is for the TiN coating. A low indentation depth indicates that the material is harder and as a result, it has more resistance against external force. Figure 7(c) presents the values of hardness (H), Young's modulus (E), H/E, and H^3/E^2 of the substrate and the coatings.

As can be seen, the highest hardness is related to the TiN coating and the lowest hardness is related to the substrate. Also, the highest Young's modulus, H/E ratio and H^3/E^2 ratio belong to the TiN coating. These parameters can efficiently predict the tribological behaviour of a coating [33].

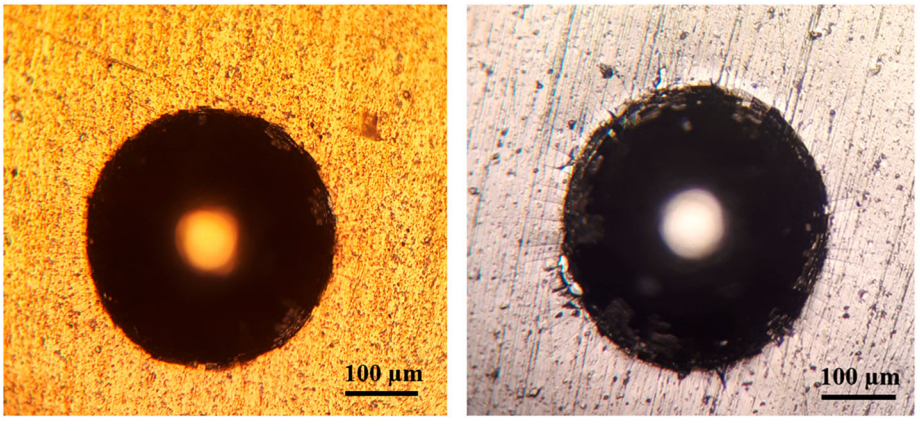

Figure 6. Optical microscopy images from Rockwell indentation effect (×100 and ×200): (a,b) TiN and (c,d) CrN coatings.

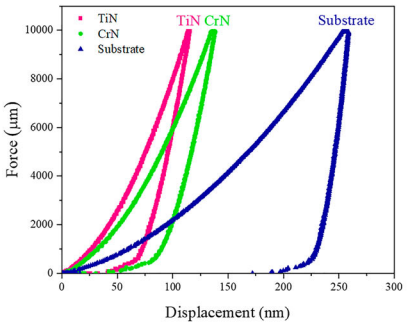

(a)

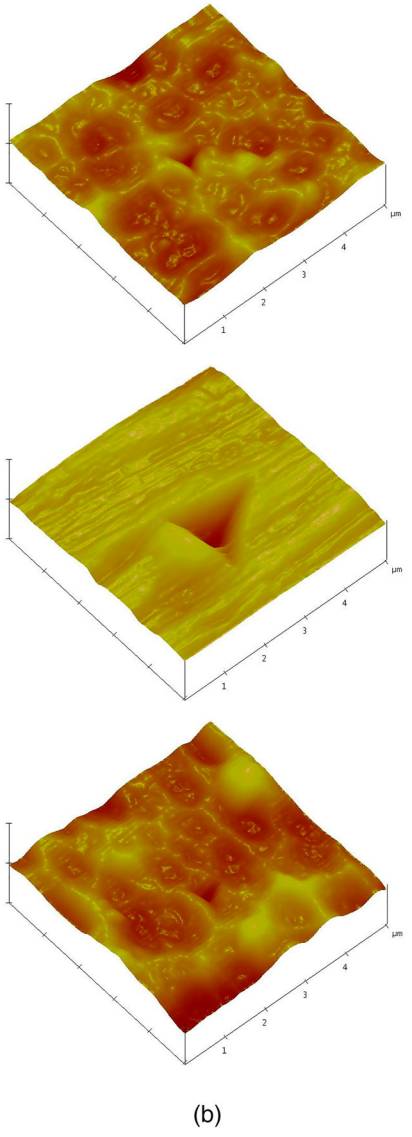

(b)

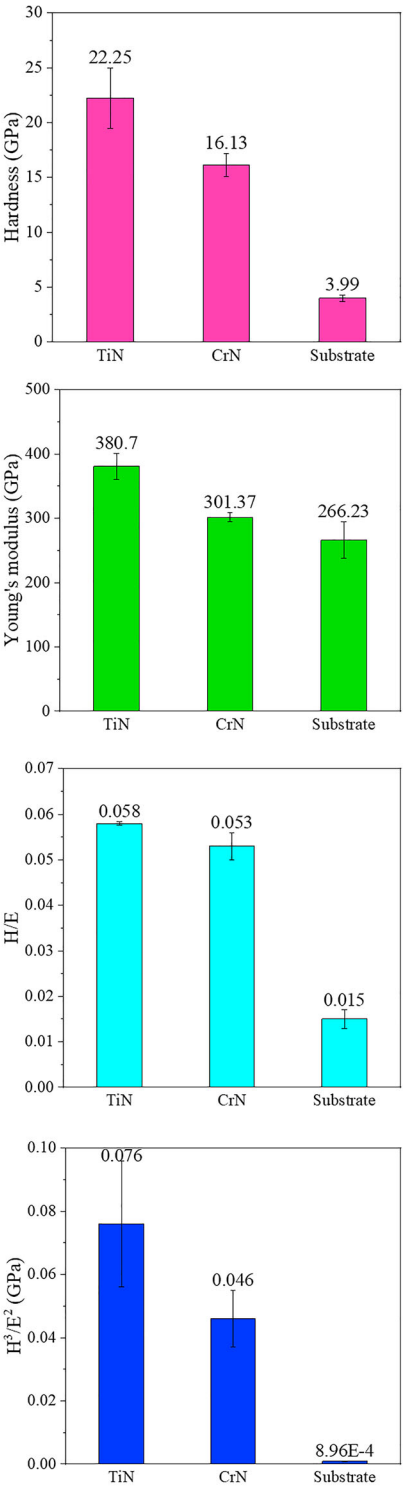

(c)

Figure 7. Nanoindentation results of TiN and CrN coatings and substrate: (a) Force-displacement plots, (b) AFM images from the indentation effect, (c) Mechanical properties.

3.4. Wear behaviour

The wear test was performed on the substrate, CrN, and TiN coatings by a ball-on-disk tester. SEM images of the wear surface of the samples are presented in Figure 8. As can be seen, the width of the wear grooves in Figure 8 is in the following order: TiN R, TiN S, CrN S, CrN R and finally, the substrate. In addition, it can be seen from the SEM images that the wear mechanism could be a mixture of adhesion and abrasion. The wear profile plots are also given in Figure 9(a). By comparing the width of the wear grooves, it is clear that the width of the wear groove in TiN coating is smaller than that of CrN. As can be seen, the width of the wear grooves in Figure 9 is consistent with the width measured by SEM images (Figure 8).

By calculating the side area of the wear grooves (Figure 9(a)) and using Equation 1, the wear rates (W) were calculated [34,35]. In this equation, V is the lost volume, which is equal to the product of the area under the plot and the wear track diameter, which was 13 mm. F_n is the applied force in newtons, and S is the sliding distance in metres. W is calculated in terms of 10^{-6} mm^3/N.m.

$$W = \frac{V}{F_n.S} \tag{1}$$

The friction constant and wear loss rate of the substrate and TiN S, TiN R, CrN S, and CrN R coatings are presented in Figure 9 (b, c). As can be seen, the calculated wear rates and the measured friction coefficients of the samples are consistent with each other and the largest wear rate and friction constant are for the substrate. The wear rate of TiN coating is lower than that of CrN coating, and this is consistent with the wear groove results. Therefore, TiN coating has higher wear resistance [19].

An important influencing factor in determining the wear rate of a material is its hardness. According to Figure 10(a), the hardness of the TiN coating is larger than the CrN coating and therefore it is expected to get a lower wear rate for TiN coating. In addition, the surface roughness of the TiN coating is lower than that of the CrN coating which may result in less interaction between the abrasive ball and the surface and therefore a decreased wear rate [36,37].

In addition to the mentioned reasons, other parameters affect the wear behaviour of coatings. These parameters are H/E and H^3/E^2, the ratios of hardness and Young's modulus, which are a measure of the material's resistance to permanent deformation. As can be seen in Figure 10(b), because the ratio of H/E and H^3/E^2 in TiN coating is higher than CrN, the wear rate in TiN is lower than CrN. When the ratios of H/E and H^3/E^2 are greater for a coating, the contact pressure is reduced and the applied load is distributed over a larger area. This makes the coating have a higher load-bearing capacity and when the wear ball slides over the surface, the coating can withstand the external load without exceeding its

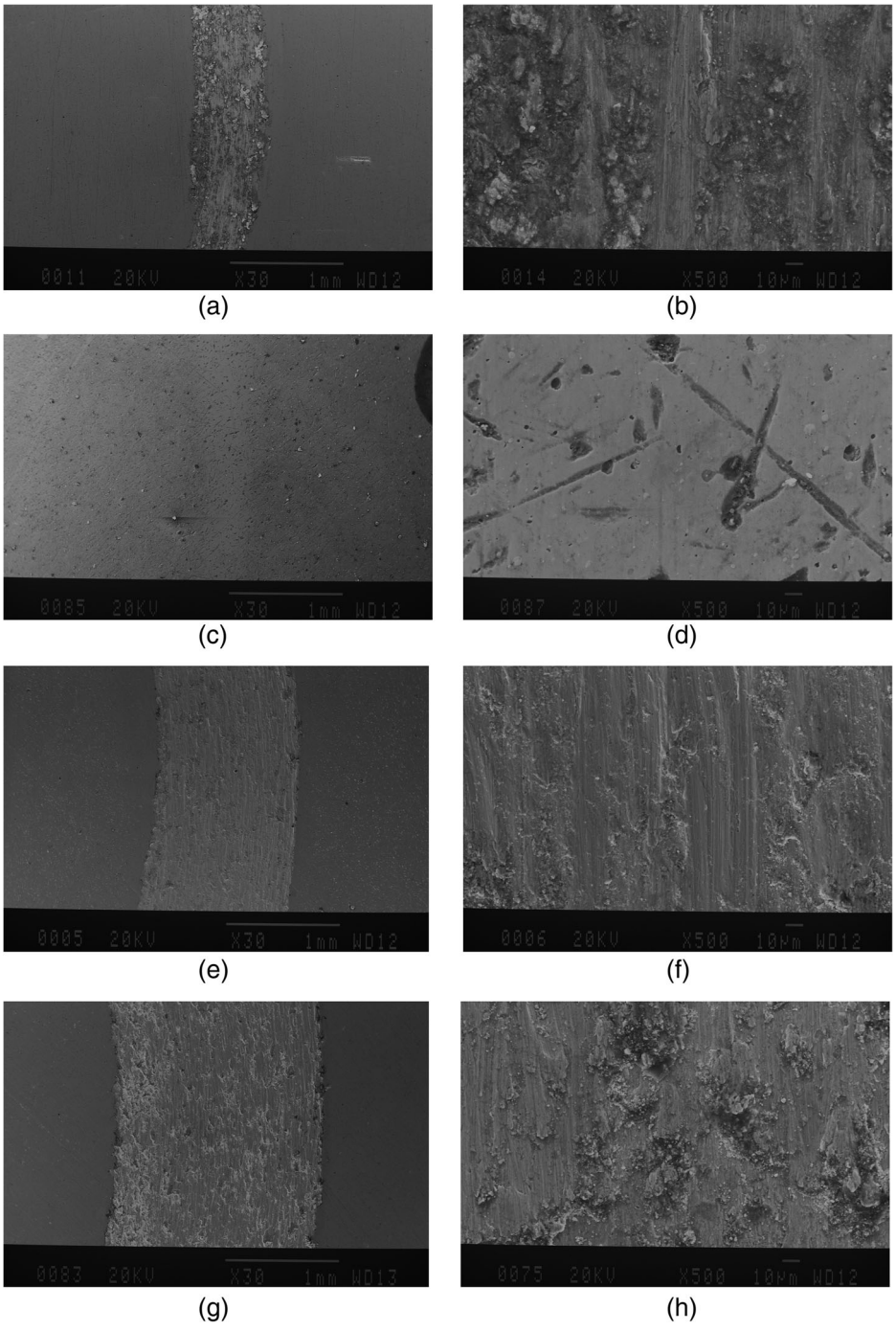

Figure 8. SEM images of the worn surfaces (×30, ×500): (a,b) TiN S, (c,d) TiN R, (e,f) CrN S, (g,h) CrN R.

elastic limit, and therefore its wear resistance increases [35,38]. Figure 10(b) shows the relationship between H/E and H^3/E^2 values with the wear rate values of the substrate and TiN and CrN coatings.

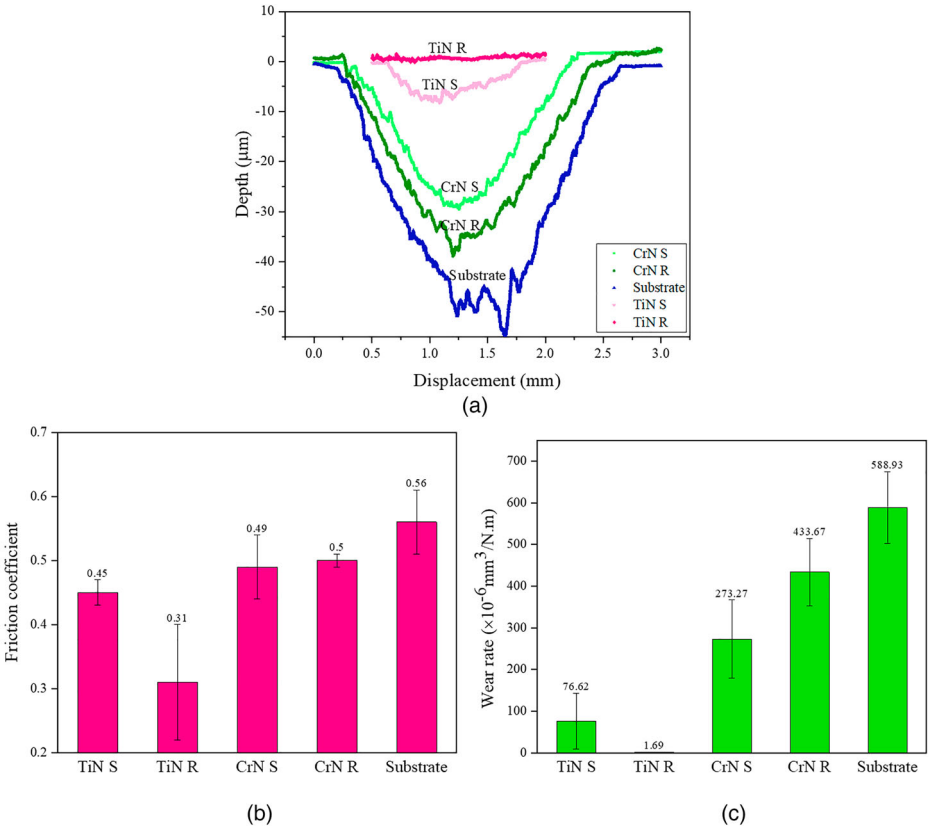

Figure 9. Results of wear test for substrate, TiN R, TiN S, CrN R, and CrN S coatings: (a) Wear profile, (b) Friction coefficient, and (c) wear rate.

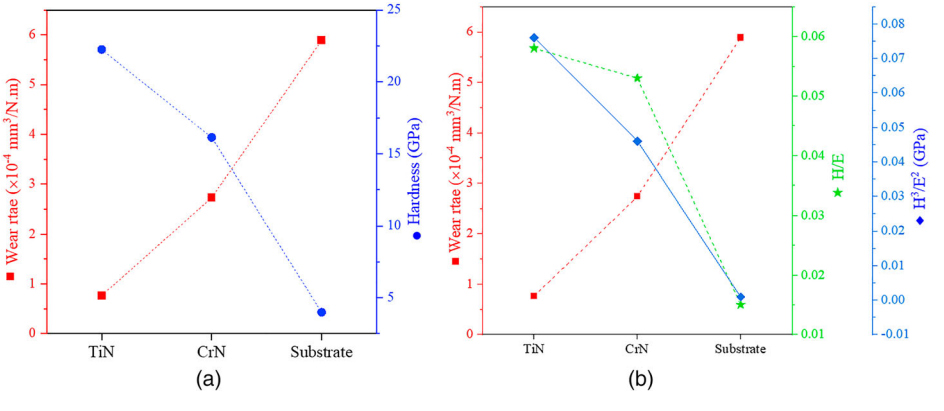

Figure 10. (a) Wear rate and hardness plots and (b) Wear rate and H/E and H^3/E^2 ratios for CrN and TiN coatings.

One interesting observation (Figure 9(c)) is that with the increase of surface roughness, the wear rate in TiN coating decreased and increased in CrN coating. As mentioned before, the surface of the coatings after the deposition

(before polishing) is covered with macroparticles: the CrN coating has a larger amount of fine macroparticles, while the coarsest macroparticles belong to the latter. During the wear process, coarse macroparticles act as a bumper and reduce the wear rate. On the other hand, fine macroparticles are also crushed during the wear process and produce abrasive particles, which cause severe wear.

On the other hand, in the CrN S coating, because the fine macroparticles had little adhesion to the surface, it was easy to separate them from the surface and they were removed by polishing the surface, and therefore the abrasive role was reduced. However, the coarse macroparticles had a stronger bond with the surface and they remained on the surface after polishing and played the positive role as bumper. Therefore, the wear rate of CrN S coating is lower than CrN R. In the TiN coating, the macroparticles act as a bumper and reduce the wear rate of the TiN R coating [39]. However, these macroparticles had a weak bond with the coating and therefore after polishing the surface, they were detached from the surface and therefore the surface lost the bumper. As a result, the wear rate of TiN S coating is higher than TiN R. Also, the surface roughness of the CrN S coating is 0.13 μm and is larger than the roughness of the TiN S coating, which is 0.092 μm, and this confirms the presence of more macroparticles over the CrN coating than the TiN coating after polishing the as-coated surfaces.

3.5. Wettability behaviour

The figures of wettability of the coatings right after the wetting (t = 0) are presented in Figure 11. It is observed that the contact angle of the CrN coating is larger than that of TiN. As can be seen, with the increase of surface roughness, the contact angle of TiN has decreased. This result is consistent with Wenzel's model, which states that if the surface is hydrophilic, increasing the roughness of the surface increases its hydrophilicity, and as a result, its wettability angle decreases [40]. The reason for this is that in the case where the surface is rougher, the contact area is larger and because the surface is hydrophilic, the water droplet tends to follow all the depressions and elevations of the surface and therefore the contact angle is reduced. In the case of CrN coating, the results are reversed and the contact angle increased with the increase of roughness. Regarding the hydrophobic surface, Wenzel or Cassie–Baxter models could express the wettability of the surface. In both models, as the surface roughness increases, the contact angle increases and the hydrophobic surface becomes more hydrophobic. By further investigating and comparing the wettability angle of the CrN S coating and the related diagrams for the effect of roughness on wettability [41], it is concluded that the CrN coating also follows the Wenzel model.

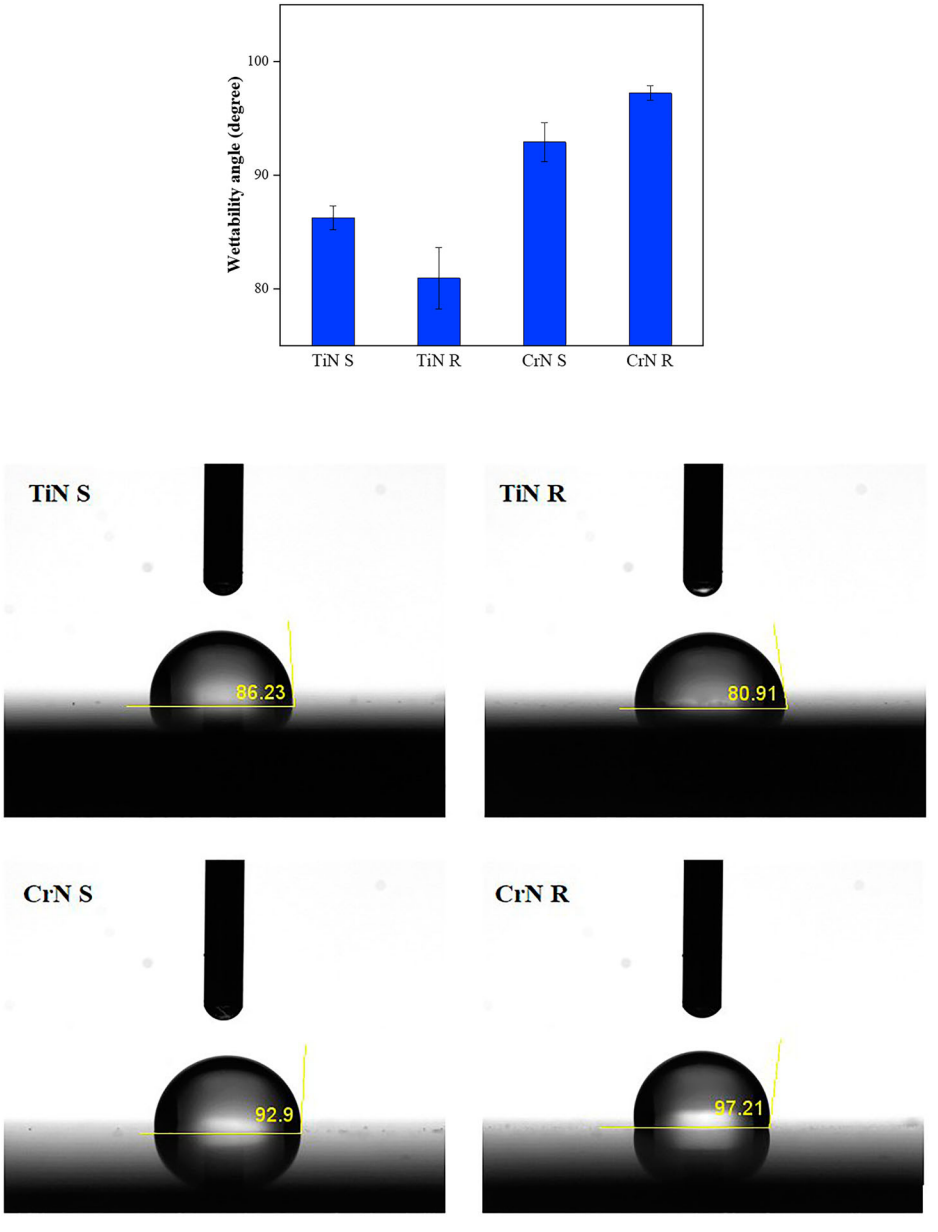

Figure 11. Wetting angles of TiN S, TiN R, CrN S, CrN R at t=0.

3.6. Corrosion behaviour

Figure 12 shows the potentiodynamic polarisation curve of TiN S, TiN R, CrN S, and CrN R coatings. Corrosion potential values and corrosion current density are shown in Table 4.

As can be seen, the lowest corrosion potential and current density were related to the CrN R coating and then belonged to the CrN S coating. This shows that the resistance of the CrN sample is higher than the TiN sample

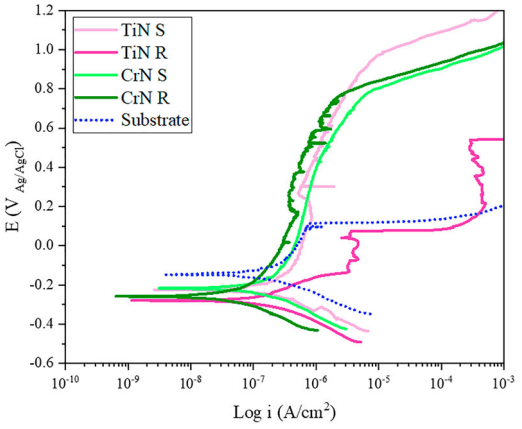

Figure 12. Potentiodynamic polarization curves for substrate and TiN S, TiN R, CrN S, and CrN R coatings tested in 3.5 wt.% NaCl solution.

and the substrate to corrosion. In addition, the passive area formed in CrN coatings is more than TiN and has improved its corrosion resistance. Also, the graphs of Nyquist spectroscopy and electrochemical impedance of TiN S, TiN R, CrN S, and CrN R coatings are shown in Figure 13(a-c).

The mechanism of electrochemical reactions could be simulated by an equivalent circuit model of the coatings (Figure 14(a)) and an equivalent circuit for the substrate (Figure 14(b)) [42]. In Figure 14(a), R_1 is the solution or electrolyte resistance, R_2 is the coating resistance, and R_3 is the resistance to charge transfer induced by the doubl-layer formation at the interface of the substrate/electrolyte. Also, CPE_1 and CPE_2 are the constant phase elements of the coating and the double-layer. In Figure 14(b), R_1 is the solution or electrolyte resistance, R_2 is the resistance to charge transfer induced by the double-layer formation at the interface of the substrate/electrolyte, and CPE_1 is the stationary phase element of the double-layer.

The results of simulating the corrosion behaviour of samples with equivalent circuits are summarised in Table 5. According to the Nyquist diagram, it can be seen that the largest diameter of the capacitor ring is related to the CrN R and then the CrN S coating. It can also be seen in Table 5 that the maximum capacitance resistance is related to the CrN R coating. Increasing the diameter of the capacitive ring and increasing the capacitive resistance means increasing the

Table 4. Corrosion test data for the substrate and TiN S, TiN R, CrN S and CrN R coatings.

Sample	E_{corr} (mV)	i_{corr} (A/cm^2)	β_a (mV/dec)	β_c (mV/dec)
Substrate	−147	1.12×10^{-7}	134	87
TiN S	−225	1.08×10^{-7}	252	12
TiN R	−28	1.26×10^{-7}	134	102
CrN S	−215	0.64×10^{-7}	125	82
CrN R	−257	0.38×10^{-7}	177	115

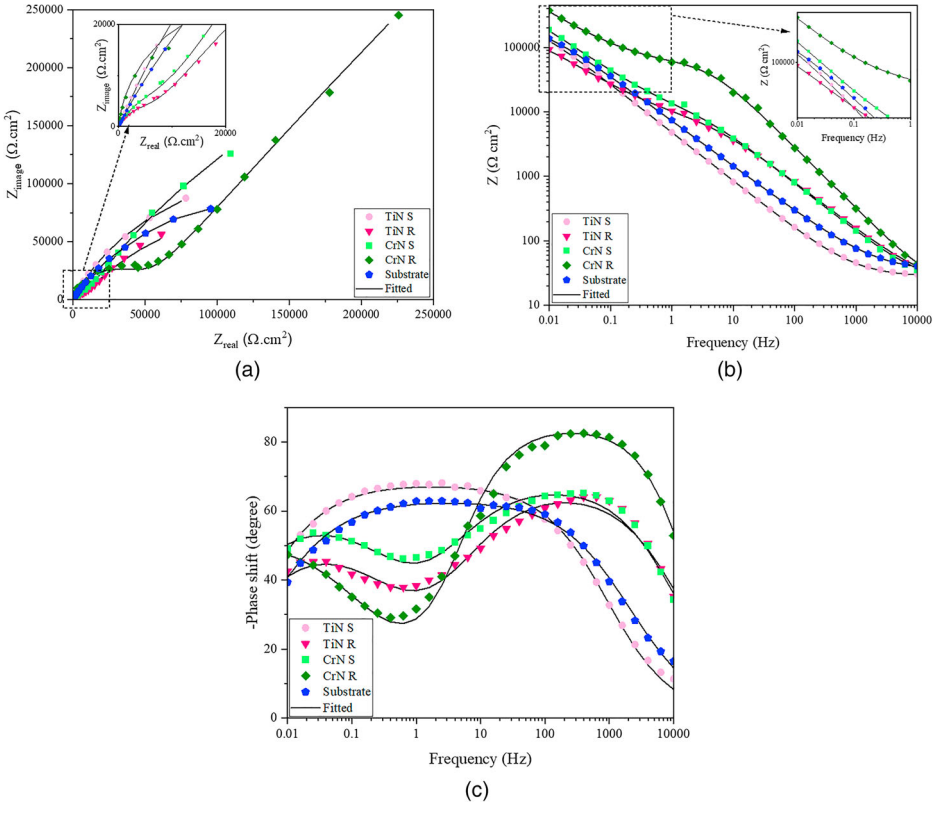

Figure 13. EIS plots for the samples immersed in 3.5 wt.% NaCl solution for 2 h: (a) Nyquist, (b) Bode/module, and (c) Bode/phase.

corrosion resistance of CrN coatings compared to the substrate and TiN coating. Therefore, according to the impedance and polarisation diagrams, the corrosion resistance of the samples increases as follows: TiN R, Substrate, TiN S, CrN S, and CrN R.

Many parameters influence the corrosion behaviour of a material, including surface roughness and morphology, the amount of surface defects, the number of surface wettability, and the architecture and chemical composition of the coatings. In CrN and TiN coatings, due to their nanolayer structure, the number of interfaces increases, and if a crack occurs, the crack path is

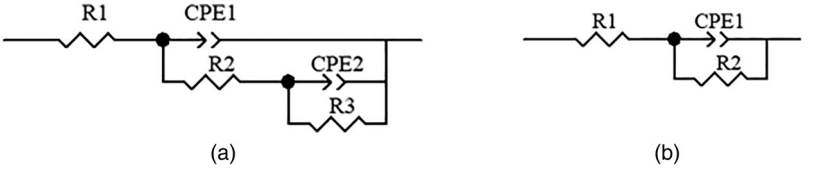

Figure 14. Equivalent electrical circuit to simulate corrosion behavior of (a) Coatings and (b) substrate.

Table 5. Electrochemical parameters data (in 3.5 wt.% of NaCl solution).

Sample	R_1 ($\Omega.cm^2$)	R_2 ($\times 10^5$) ($\Omega.cm^2$)	R_3 ($\times 10^5$) ($\Omega.cm^2$)	$R_2 + R3$ ($\times 10^5$) ($\Omega.cm^2$)
Substrate	48.59	4.6	....	4.6
TiN S	36	0.18	4.9	5.08
TiN R	31.27	0.15	4.3	4.45
CrN S	31.19	0.24	13.47	13.71
CrN R	33.93	0.82	127.54	128.36

blocked, and the corrosive media needs more time to reach the surface of the substrate and cause corrosion [22].

In other words, the deposition of alternating nanolayers of different materials prevents the formation of crystallites with continuous boundaries and therefore the possibility of creating holes in the coating is reduced. As a result of reducing the structural defects and blocking the defects of each layer by the next layer, the corrosion resistance of the coating increases [43].

Therefore, the nanolayer architecture of the coatings increases the corrosion resistance. One of the reasons for the difference in the corrosion behaviour of CrN coating compared to TiN coating is the formation of the passive layer by CrN coating, which improves corrosion resistance. Another difference is that the CrN coating has a dense structure and does not provide any direct pathway for the diffusion of the corrosive media into the substrate, but the TiN coating has a columnar structure, which causes the corrosive media to reach the surface of the substrate faster and reduces its corrosion resistance [22].

Also, when the TiN coating dissolves, nitrogen releases and reacts with H^+ ions in the electrolyte, and H^+ ions are neutralised and turn into NH_4^+, but in an electrolyte that is rich in Cl^-, TiN cannot prevent the complete penetration of Cl^- into the coating, and due to defects on the surface, corrosive ions penetrate the coating through these channels and create a galvanic effect at the interface of the coating and the substrate, which due to the difference in composition, increase the rate of corrosion [44].

Another influencing factor in the corrosion behaviour of coatings is the level of surface roughness and wettability. In the CrN R coating, it is observed that despite having the highest level of surface roughness, it is observed that it has the highest corrosion resistance and this is due to the effect of roughness on the wettability. In fact, the increase in roughness has increased the hydrophobicity of the CrN R coating surface, and the increase in hydrophobicity has also affected the corrosion behaviour and increased its corrosion resistance. On the other hand, in TiN coating, it can be seen that with the increase of surface roughness, the corrosion resistance has decreased and it has shown the weakest corrosion resistance. In the TiN coating, the increase in surface roughness has caused more hydrophilicity in the TiN R coating, and the increase in hydrophilicity has also caused a greater penetration of the corrosive solution and a decrease in the corrosion resistance.

4. Conclusions

In this research, two types of TiN/CrN multi-layer coatings were investigated: TiN upper layer and CrN upper layer. Each type of coating has two different surface conditions: smooth (polished) and rough. The following results were obtained:

- The results of the nanoindentation test showed that in the case where the upper layer is TiN, the hardness, Young's modulus, H/E, and H^3/E^2 were 5.57, 1.42, 3.86, and 85.39 times against substrate, respectively. For the coating with a CrN upper layer, these values were 4.04, 1.13, 3.53, and 51.68 times against substrate, respectively.
- The values of hardness and Young's modulus and the combined ratios between these two parameters affect the wear behaviour of coatings. Thus, the wear resistance of TiN coating is higher than that of CrN coating. In the rough condition, the wear rate in TiN coating is reduced by about 99% compared to CrN, while in the smooth state, it is reduced by about 72%.
- The increase in surface roughness in TiN coating has increased wear resistance, whereas in CrN coating it has decreased wear resistance. TiN and CrN have performed better in the rough and smooth states, respectively. This is ascribed to the presence of macroparticles on the surface. Polishing the surface in the TiN coating has reduced the positive role of macroparticles as a bumper, and the wear rate has increased in the smooth state, due to the higher friction. While in the CrN coating, polishing has increased the amount of macroparticles on the surface, and they have played the role of the bumper and reduced the wear rate, due to the lower friction. In the TiN coating, increasing the roughness has reduced the wear rate by 97%, and in the CrN coating, increasing the roughness has increased the wear rate by 58%.
- The increase in surface roughness in CrN coating has increased the hydrophobicity of the surface and the increase in roughness in TiN coating has increased its hydrophilicity. Changing the wettability behaviour of coatings has changed their corrosion resistance. CrN R coating has shown the highest corrosion resistance due to the formation of a passive layer and high hydrophobicity, whereas TiN R coating has shown the lowest corrosion resistance due to its high hydrophilicity.

Disclosure statement

No potential conflict of interest was reported by the author(s).

ORCID

Meisam Nouri http://orcid.org/0000-0003-1027-1042

References

[1] G.A. Rodríguez-BRavo, M. Vite-Torres, and J.G. Godínez Salcedo, *Analysis on the corrosion rate changes of Aisi 410 stainless steel submitted to abrasion-corrosion in simulated marine conditions*. Proc. Eng. Sci. 1(1) (2019), pp. 90–97. doi: 10.24874/pes01.01.012.

[2] R.T. Loto, *Study of the corrosion behaviour of S32101 duplex and 410 martensitic stainless steel for application in oil refinery distillation systems*. J. Mater. Res. Technol 6(3) (2017), pp. 203–212. doi: 10.1016/j.jmrt.2016.11.001.

[3] T.S. De Oliveira, E.S. Silva, S.F. Rodrigues, C.C.F. Nascimento, V.S. Leala, and G.S. Reis, *Softening mechanisms of the AISI 410 martensitic stainless steel under hot torsion simulation*. Mater. Res 20(2) (2017), pp. 395–406. doi: 10.1590/1980-5373-MR-2016-0795.

[4] A. Pramanik and A.K. Basak, *Stainless Steel Microstructure, Mechanical Properties and Methods of Application*, Nova Science Publishers, New York, 2015.

[5] Y. Dvirnyk, D. Pavlenko, and R. Przysowa, *Determination of serviceability limits of a turboshaft engine by the criterion of blade natural frequency and stall margin*. Aerospace 304 (2019), pp. 03004. doi: 10.1051/matecconf/201930403004.

[6] L.E. Geambazu, I. Voiculescu, C.A. Manea, and R.V. Bololoi, *Economic efficiency of high-entropy alloy corrosion-resistant coatings designed for geothermal turbine blades: a case study*. Appl. Sci. 12(14) (2022). doi: 10.3390/app12147196.

[7] P. Fördös and J. Čerňan, *Analysis of the impact of hard pvd coatings on the abrasion resistance of the compressor blades*. Adv Mil Technol. 15(1) (2020), pp. 85–95. doi: 10.3849/aimt.01333.

[8] N. Bharadishettar, K.U. Bhat, and D.B. Panemangalore, *Coating technologies for copper based antimicrobial active surfaces: a perspective review*. Metals 11(5) (2021). doi: 10.3390/met11050711.

[9] B. Fotovvati, N. Namdari, and A. Dehghanghadikolaei, *On coating techniques for surface protection: a review*. J. Manuf. Mater. Process 3(1) (2019). doi: 10.3390/jmmp3010028.

[10] Z.A. Fazel, H. Elmkhah, A. Fattah-Alhosseini, K. Babaei, and M. Meghdari, *Comparing electrochemical behavior of applied CrN/TiN nanoscale multilayer and TiN single-layer coatings deposited by CAE-PVD method*. J. Asian Ceram. Soc 8(2) (2020), pp. 510–518. doi: 10.1080/21870764.2020.1756065.

[11] G. Faghani, S.M. Rabiee, S. Nourouzi, and H. Elmkhah, *Self-cleaning properties of TiN/CrN nanoscale multi-layer deposited on surgical 420C stainless steel*. Journal of Nanostructures 9(4) (2019), pp. 702–711. doi: 10.22052/JNS.2019.04.012.

[12] K. Khlifi and A. Ben Cheikh Larbi, *Investigation of adhesion of PVD coatings using various approaches*. Surf. Eng 29(7) (2013), pp. 555–560. doi: 10.1179/1743294413Y.0000000150.

[13] F. Lin, Y. Xia, and X. Feng, *Conductive and tribological properties of TiN-Ag composite coatings under grease lubrication*. Friction 9(4) (2021), pp. 774–788. doi: 10.1007/s40544-020-0373-4.

[14] A. Agüero, M. Juez-Lorenzo, P.E. Hovsepian, A.P. Ehiasarian, Y.P. Purandare, and R. Muelas, *Long-term behaviour of Nb and Cr nitrides nanostructured coatings under steam at 650 °C. Mechanistic considerations*. J. Alloys Compd 739 (2018), pp. 549–558. doi: 10.1016/j.jallcom.2017.12.288.

[15] Y. Liu, S. Yu, Q. Shi, X. Ge, and W. Wang, *Multilayer coatings for tribology: a mini review*. Nanomaterials 12(9) (2022). doi: 10.3390/nano12091388.

[16] W. Ernst, J. Neidhardt, H. Willmann, B. Sartory, P.H. Mayrhofer, and C. Mitterer, *Thermal decomposition routes of CrN hard coatings synthesized by reactive arc evaporation and magnetron sputtering*. Thin Solid Films 517(2) (2008), pp. 568–574. doi: 10.1016/j.tsf.2008.06.086.

[17] A. Pogrebnjak, K. Smyrnova, and O. Bondar, *Nanocomposite multilayer binary nitride coatings based on transition and refractory metals: structure and properties*. Coatings 9(3) (2019). doi: 10.3390/coatings9030155.

[18] V.S. Pahade, P.S. Chavan, and V.P. Baisane, *A review paper on vapour deposition coating," Int*. J. Eng. Appl. Sci 3(6) (2016), pp. 75–78. [Online]. Available: www.ijeas.org.

[19] E. Lotfi-khojasteh, M. Sahebazamani, H. Elmkhah, M. Nouri, O. Imantalab, and A. Fattah-alhosseini, *A study of the electrochemical and tribological properties of TiN/CrN nano-layer coating deposited on carburized-H13 hot-work steel by Arc-PVD technique*. J. Asian Ceram. Soc 9(1) (2021), pp. 247–259. doi: 10.1080/21870764.2020.1863577.

[20] Q. Yang, L.R. Zhao, and P. Patnaik, *Erosion performance, corrosion characteristics and hydrophobicity of nanolayered and multilayered metal nitride coatings*. Surf. Coat. Technol. 375 (2019), pp. 763–772. doi: 10.1016/j.surfcoat.2019.07.074.

[21] L. Kolaklieva, S. Rabadzhiyska, R. Kakanakov, V. Chitanov, T. Cholakova, V. Rupetchov, and G. Mishev, *Evaluation of the mechanical and tribological properties of multilayer CrN/TiN films deposited at low temperatures*, in *Proceedings of the International Conference on Microelectronics, ICM*, L. Anguera S.C. Satapathy, V. Bhateja and K.V.N. Sunitha, eds., Springer, Sigapore, 2017, pp. 187–190. doi: 10.1109/MIEL.2017.8190099.

[22] H. Olia, R. Ebrahimi-Kahrizsangi, F. Ashrafizadeh, and I. Ebrahimzadeh, *Comparative study of corrosion and corrosion-wear behavior of TiN and CrN coatings on UNS S17400 stainless steel*. Corros. Rev 36(4) (2018), pp. 403–412. doi: 10.1515/corrrev-2017-0130.

[23] G. Faghani, S.M. Rabiee, S. Nourouzi, and H. Elmkhah, *Corrosion behavior of TiN/CrN nanoscale multi-layered coating in ringer's solution*. Int. J. Eng. Trans. B Appl 33(2) (2020), pp. 329–336. doi: 10.5829/IJE.2020.33.02B.18.

[24] M. Forouzanmehr, K. Reza Kashyzadeh, A. Borjali, A. Ivanov, M. Jafarnode, T.H. Gan, B. Wang, and M. Chizari, *Detection and analysis of corrosion and contact resistance faults of TiN and CrN coatings on 410 stainless steel as bipolar plates in PEM fuel cells*. Sensors 22(3) (2022). doi: 10.3390/s22030750.

[25] S.G. Croll, *Surface roughness profile and its effect on coating adhesion and corrosion protection: a review*. Prog. Org. Coatings 148 (2020), doi: 10.1016/j.porgcoat.2020.105847.

[26] A.S. Toloei, V. Stoilov, and D.O. Northwood, *The effect of different surface topographies on the corrosion behaviour of nickel*. WIT Trans. Eng. Sci. 77 (2013), pp. 193–204. doi: 10.2495/MC130171.

[27] M. Hanief and M.F. Wani, *Effect of surface roughness on wear rate during running-in of En31-steel: model and experimental validation*. Mater. Lett 176 (2016), pp. 91–93. doi: 10.1016/j.matlet.2016.04.087.

[28] N.S. Mansoor, A. Fattah-alhosseini, H. Elmkhah, and A. Shishehian, *Electrochemical behavior of TiN, CrN and TiN/CrN nanostructured coatings on the nickel-chromium alloy used in dental fixed prosthesis*. J. Asian Ceram. Soc 8(3) (2020), pp. 694–710. doi: 10.1080/21870764.2020.1776915.

[29] Z. Zhang, J. Chen, G. He, and G. Yang, *Fatigue and mechanical behavior of Ti-6Al-4V alloy with CrN and TiN coating deposited by magnetic filtered cathodic vacuum arc process*. Coatings 9(10) (2019), pp. 1–13. doi: 10.3390/COATINGS9100689.

[30] R. Hahn, M. Bartosik, R. Soler, C. Kirchlechner, G. Dehm, and P.H. Mayrhofer, *Superlattice effect for enhanced fracture toughness of hard coatings*. Scr. Mater 124 (2016), pp. 67–70. doi: 10.1016/j.scriptamat.2016.06.030.

[31] C.H. Hsu, C.K. Lin, K.H. Huang, and K.L. Ou, *Improvement on hardness and corrosion resistance of ferritic stainless steel via PVD-(Ti,Cr)N coatings*. Surf. Coatings Technol 231 (2013), pp. 380–384. doi: 10.1016/j.surfcoat.2012.05.095.

[32] P.E. Hovsepian, A.A. Sugumaran, Y. Purandare, and A.P. Ehiasarian, *Corrosion behaviour of post-deposition polished droplets- embedded arc evaporated and droplets-free HIPIMS / DCMS coatings*. Corros. -Houst. Tx (2017), pp. 685–693. doi: 10.5006/2064.

[33] B.D. Beake, V.M. Vishnyakov, and A.J. Harris, *Nano-scratch testing of (Ti,Fe)Nx thin films on silicon*. Surf. Coat. Technol. 309 (2017), pp. 671–679. doi: 10.1016/j.surfcoat.2016.11.024.

[34] A.M. Kenneth Holmberg, *Coatings Tribology Properties, Mechanisms, Techniques and Applications in Surface*, Elsevier, Oxford, 2009.

[35] Y. Feng, J. Cheng, D. Liu, and X. Liang, *Effects of Cr and Nb additions on sliding wear behaviors of the FePSiB coatings*. Coatings 8(12) (2018). doi: 10.3390/COATINGS8120463.

[36] G. Faghani, S.M. Rabiee, S. Nourouzi, and H. Elmkhah, *Nanoscale multi-layer thin film fabricated by Cathodic Arc Evaporation (CAE) method*. J. Superhard Mater 42(2) (2020), pp. 78–89. doi: 10.3103/S1063457620020057.

[37] X. Huang, T. Junguo, Z. Tengfei, M. Jinjun, G. Zecui, Z. Xing, and W. Qimin, *Deposition and anti-wear/corrosion properties of nano-multilayer TiN/CrN films on titanium alloy*. Cailiao Daobao/Materials Reports 35(4) (2021), pp. 04139–04143. doi: 10.11896/cldb.19070256.

[38] J. Guo, H. Wang, F. Meng, X. Liu, and F. Huang, *Tuning the H/E* ratio and E* of AlN coatings by copper addition*. Surf. Coat. Technol. 228 (2013), pp. 68–75. doi: 10.1016/j.surfcoat.2013.04.008.

[39] W.Y. Lee, Y.J. Jang, T. Tokoroyama, M. Murashima, and N. Umehara, *Effect of defects on wear behavior in ta-C coating prepared by filtered cathodic vacuum arc deposition*. Diamond Relat. Mater. 105 (2020). doi: 10.1016/j.diamond.2020.107789.

[40] J. Wang, Y. Wu, Y. Cao, G. Li, and Y. Liao, *Influence of surface roughness on contact angle hysteresis and spreading work*. Colloid Polym. Sci. 298(8) (2020), pp. 1107–1112. doi: 10.1007/s00396-020-04680-x.

[41] L. Cao, *Superhydrophobic surface design fabrication and application*, Ph.D. Thesis, University of Pittsburgh, 2010.

[42] N.S. Mansoor, A. Fattah-Alhosseini, H. Elmkhah, and A. Shishehian, *Comparison of the mechanical properties and electrochemical behavior of TiN and CrN single-layer and CrN/TiN multi-layer coatings deposited by PVD method on a dental alloy*. Mater. Res. Express 6(12) (2019). doi: 10.1088/2053-1591/ab640d.

[43] M. Noori, M. Atapour, F. Ashrafizadeh, H. Elmkhah, G.G. di Confiengo, S. Ferraris, S. Perero, M. Cardu, and S. Spriano, *Nanostructured multilayer CAE-PVD coatings based on transition metal nitrides on Ti6Al4V alloy for biomedical applications*. Ceram. Int. 49(14) (2023), Techna Group S.r.l.

[44] J. Lou, Z. Gao, J. Zhang, H. He, and X. Wang, *Comparative investigation on corrosion resistance of stainless steels coated with titanium nitride, nitrogen titanium carbide and titanium-diamond-like carbon films*. Coatings 11(12) (2021). doi: 10.3390/coatings11121543.

Philosophical Magazine

ISSN: 1478-6435 (Print) 1478-6443 (Online) Journal homepage: www.tandfonline.com/journals/tphm20

Comparing hysteresis properties of graphene honeycomb and pentagraphene nanostructures via Monte Carlo simulations

R. El Fdil, Z. Fadil, Chaitany Jayprakash Raorane, Khaled H. Mahmoud, Abdulrahman A. Alsayyari, Seong-Cheol Kim, E. Salmani & H. Ez-Zahraouy

To cite this article: R. El Fdil, Z. Fadil, Chaitany Jayprakash Raorane, Khaled H. Mahmoud, Abdulrahman A. Alsayyari, Seong-Cheol Kim, E. Salmani & H. Ez-Zahraouy (2026) Comparing hysteresis properties of graphene honeycomb and pentagraphene nanostructures via Monte Carlo simulations, Philosophical Magazine, 106:4, 380-394, DOI: 10.1080/14786435.2025.2564415

To link to this article: https://doi.org/10.1080/14786435.2025.2564415

Published online: 01 Oct 2025.

PHILOSOPHICAL MAGAZINE
2026, VOL. 106, NO. 4, 380–394
https://doi.org/10.1080/14786435.2025.2564415

Comparing hysteresis properties of graphene honeycomb and pentagraphene nanostructures via Monte Carlo simulations

R. El Fdil[a], Z. Fadil[a], Chaitany Jayprakash Raorane[b], Khaled H. Mahmoud[c], Abdulrahman A. Alsayyari[d], Seong-Cheol Kim[b], E. Salmani[a] and H. Ez-Zahraouy[a]

[a]Laboratoire de Matière Condensée et Sciences Interdisciplinaires (LaMCScI), Faculty of Sciences, URL-CNRST, Mohammed V University in Rabat, Rabat, Morocco; [b]School of Chemical Engineering, Yeungnam University, Gyeongsan, Republic of Korea; [c]Department of Physics, College of Khurma University College, Taif University, Taif, Saudi Arabia; [d]Department of Radiologic Technology, College of Applied Medical Sciences, Qassim University, Buraydah, Saudi Arabia

ABSTRACT

We conducted a numerical study of hysteresis effects in graphene and pentagraphene by Monte Carlo simulations, based on the Blume-Emery-Griffiths model. The analysis focused on the coercive () and saturation () fields under the influence of exchange couplings (,), temperature (), and crystal field (). The results revealed that the honeycomb structure of graphene exhibited higher and due to its more ordered lattice, improving spin alignment. These results highlight the crucial role of the lattice structure in magnetic behaviour and offer insights into the tunability of these nanostructures for applications in spintronics and magnetic storage.

ARTICLE HISTORY
Received 9 June 2025
Accepted 8 September 2025

KEYWORDS
Graphene honeycomb; pentagraphene; nanostructure; magnetic hysteresis cycles; Monte Carlo simulations; Blume-Emery-Griffiths model

1. Introduction

Two-dimensional (2D) materials are of central importance for the progress of nanotechnology due to their unique mechanical, electronic and magnetic properties [1–5]. Their reduced dimensionality and surface-dominated behaviour offer promising opportunities for applications in flexible electronics, energy harvesting, catalysis and sensing [5–10]. Graphene is characterised by a single sheet of atomic carbon, forming a hexagonal lattice has revolutionised materials science with its exceptional electrical conductivity, high mechanical strength and thermal stability [11, 12]. In parallel, pentagraphene, a theoretically predicted carbon allotrope composed entirely of pentagons, has attracted growing interest due to its negative Poisson's ratio, structural stability and tunable electronic and magnetic properties [13, 14]. While much attention has been paid to the transport and mechanical properties of these materials, understanding their magnetic behaviour is critical to harnessing their potential in spintronic devices and magnetic

CONTACT Z. Fadil fadilzakaria604@gmail.com Laboratoire de Matière Condensée et Sciences Interdisciplinaires (LaMCScI), Faculty of Sciences, URL-CNRST, Mohammed V University in Rabat, P.O. Box 1014, Rabat, Morocco; Chaitany Jayprakash Raorane chaitanyaraorane22@ynu.ac.kr School of Chemical Engineering, Yeungnam University, Gyeongsan 38541, Republic of Korea; Seong-Cheol Kim sckim07@ynu.ac.kr School of Chemical Engineering, Yeungnam University, Gyeongsan 38541, Republic of Korea

data storage technologies [15–17]. In such systems, the ability to control and manipulate spin degrees of freedom opens the way to high-speed, energy-efficient memory and logic components [18]. Central to this functionality is the phenomenon of magnetic hysteresis, characterised by the material's coercive field (HC) and saturation field (HS), which determine magnetic storage and switching behaviour [19, 20]. To explore these properties at the atomic level, Monte Carlo simulations provide a robust computational approach for modelling spin interactions under different thermal and magnetic field conditions [21, 22]. In conjunction with the Blume-Emery-Griffiths (BEG) model, which takes into account bilinear and biquadratic exchange interactions and the anisotropy of individual ions, these simulations enable accurate and flexible description of magnetic ordering in complex nanostructures [23–25]. This framework is widely used in the study of low-dimensional magnetic systems. Previous research has used Monte Carlo methods in the BEG model to analyze hysteresis behaviour, phase transitions, and critical phenomena in different geometries. For example, critical behaviour and hysteresis have been studied in hexagonal core–shell nanowires [26], and magnetisation plateaus have been observed in fullerene-like systems [27], and the combined Monte Carlo and mean-field approach has revealed rich magnetic behaviour in hexagonal Ising nanowires with core–shell structures [28]. Mixed-spin models have been investigated in honeycomb lattices [29] and under rarefaction effects [30], emphasising the role of lattice topology and disorder. Further studies have extended these methods to exotic geometries, including bilayer Kekulene [31], Blume–Capel nanowires [32] and antiperovskite Mn_3AlN compounds [33]. Further work has investigated the effects of long-range RKKY interactions in naphthalene-like nanostructures [34] and the thermal and magnetic behaviour in rubrene-like [35] and coronene-like monolayer nanostructures [36]. These studies highlight the power of Monte Carlo methods and the BEG model in capturing the intricate interplay between spin interactions, temperature and geometry and pave the way for the design of nanoscale materials in spintronics and magnetic storage applications. Moreover, the trend toward downsizing electronic components has sparked interest in 2D materials with tailored magnetism. Although graphene exhibits outstanding characteristics, its non-magnetic nature limits spintronic applications [11, 12, 15–17], which has prompted researchers to investigate pentagraphene with tunable magnetic behaviour [13, 14]. A well-defined hysteresis loop with coercive (H_C) and saturation (H_S) fields is essential for these applications [19, 20]. We use Monte Carlo simulations within the framework of the Blume-Emery-Griffiths model [23–25, 37] to examine the hysteresis properties of graphene and pentagraphene nanostructures, with a focus on the impact of exchange couplings (J, K), anisotropy (D), and temperature (T) on their magnetic response for nanoscale design.

The paper follows a systematic structure: Sect. 2 outlines the theoretical model and computational approach, Sect. 3 presents the numerical results obtained through Monte Carlo simulations, and Sect. 4 concludes with the study's key findings.

2. Model and method

To analyze the magnetic hysteresis of Graphene honeycomb ($N_T = 54$ atoms) and Pentagraphene ($N_T = 49$ atoms), this study employs Monte Carlo simulations using the Blume-Emery-Griffiths model [23–25, 37]. Carbon atoms were replaced with spin-1 analogs, and

the first 10^4 of 10^5 steps per spin were discarded for thermal stabilisation (Figure 1). The spin-1 model is commonly used to study graphene-based systems, including carbon atoms [38–40], which allows the study of complex magnetic phenomena without the need for detailed ab initio calculations. The use of integer spins, such as 1 in the Ising framework, is particularly suitable for the analysis of phase transitions and critical behaviour. Although the spin-1 model does not reflect the actual spin of graphene carbon atoms, it provides an effective approach to capture the essential features of their magnetic behaviour. Moreover, simulations on 49- and 54-atom nanostructures, confirmed by doubling the system size, show consistent magnetic behaviour, indicating negligible finite size effects. The chosen size reflects our interest in small nanostructures, where the coercive field is relevant, while larger systems will be considered in future work.

Hamiltonian governing the Graphene honeycomb and pentagraphene nanostructures:

$$H = -J \sum_{\langle i,j \rangle} S_i S_j - K \sum_{\langle i,j \rangle} (S_i S_j)^2 - H \sum_i S_i - D \sum_i (S_i)^2, \tag{1}$$

The interactions between neighbouring spins S_i and S_j in each nanostructure are determined by linear (J) and biquadratic (K) coupling terms, where $\langle i, j \rangle$ represents summation over nearest neighbours. The system is also influenced by both the intrinsic crystal field (D) and an applied external magnetic field (H).

Site energy in Graphene honeycomb (Eq. 2) and pentagraphene (Eq. 3) nanostructures:

$$E = \frac{1}{N_{T\ (Graphene\ honeycomb)}} \mathcal{H}, \tag{2}$$

$$E = \frac{1}{N_{T\ (pentagraphene)}} \mathcal{H}, \tag{3}$$

Magnetisation equations for Graphene honeycomb (Eq. 4) and pentagraphene (Eq. 5)

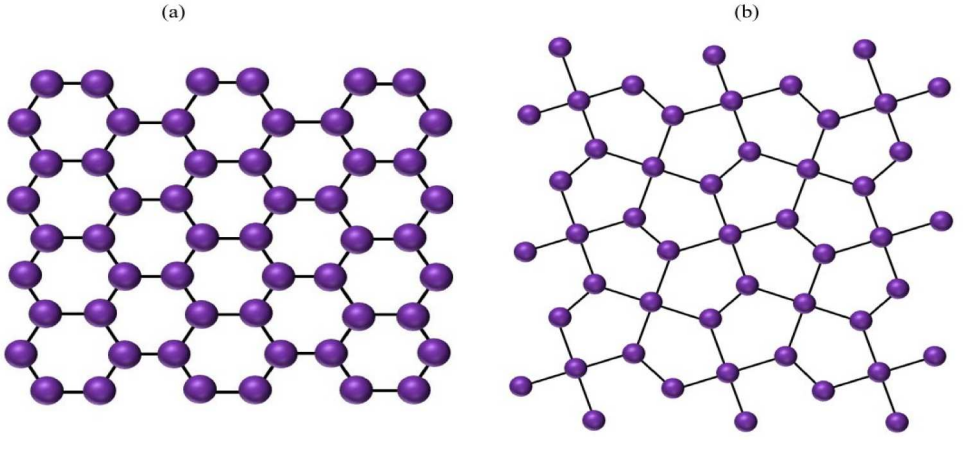

Figure 1. Graphene honeycomb (a) and pentagraphene (b) nanostructures are displayed, with all atoms carrying a spin value of 1.

nanostructures:

$$M = \frac{1}{N_{T\ (Graphene\ honeycomb)}} \sum_i S_i \tag{4}$$

$$M = \frac{1}{N_{T\ (pentagraphene)}} \sum_i S_i \tag{5}$$

3. Numerical findings via monte carlo

A Monte Carlo-based analysis of the magnetic hysteresis in Graphene honeycomb and pentagraphene nanostructures is conducted, emphasising coercive (H_C) and saturation (H_S) fields and the roles of exchange couplings (J, K), temperature (T), and crystal field (D).

Figure 2 presents a comparison of the hysteresis cycles of graphene honeycomb nanostructures and pentagraphene, calculated with $J = 0.1$, $K = 0.1$, $D = -0.1$ and $T = 0.1$. The results show that graphene honeycomb nanostructures possess significantly higher coercive (H_C) and saturation (H_S) fields than pentagraphene. Graphene honeycomb nanostructures, with their ordered lattice, promote spin alignment, leading to stronger magnetic responses and high coercive and saturation fields. In contrast, pentagraphene nanostructures have a more complex lattice, resulting in a weaker spin arrangement and lower coercive and saturation fields.

Figure 3 compares the hysteresis loops of graphene honeycomb (a) and pentagraphene (b) nanostructures, calculated with $K = 0.1$, $D = -0.1$ and $T = 0.1$. With increasing linear exchange coupling J, the magnetic hysteresis loop of graphene honeycomb and pentagraphene nanostructures widens, increasing both the coercive field (H_C) and saturation field (H_S), more significantly for graphene honeycomb. Increasing J strengthens spin

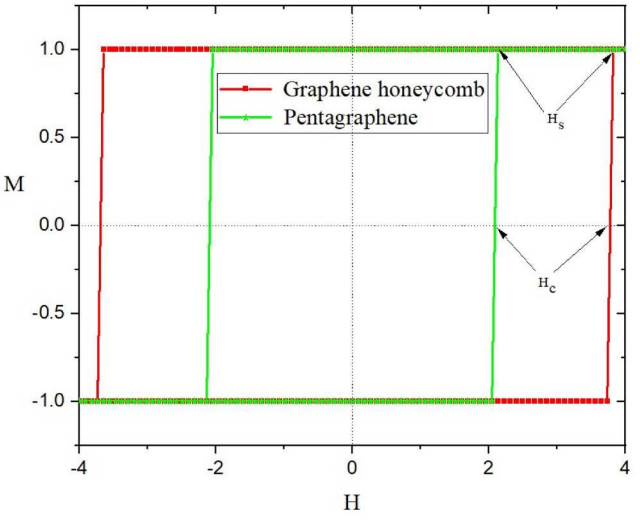

Figure 2. Hysteresis loops for Graphene honeycomb and pentagraphene nanostructures, computed with $J = 1$, $K = 0.1$, $D = -0.1$ and $T = 0.1$.

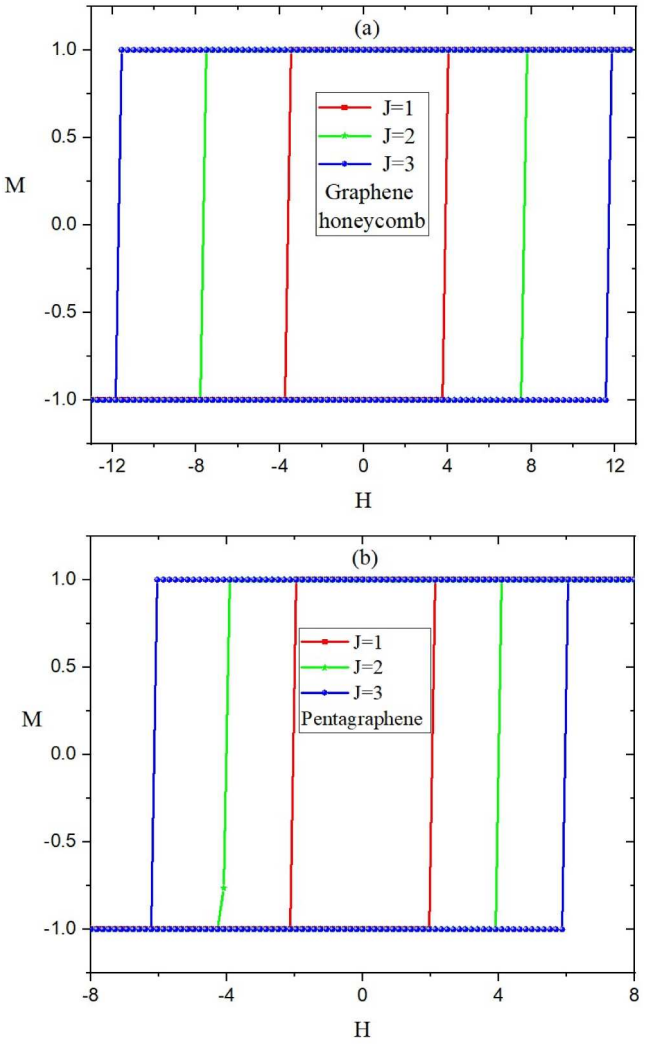

Figure 3. Hysteresis loops for Graphene honeycomb (a) and pentagraphene (b), with $K = 0.1$, $D = -0.1$ and $T = 0.1$.

interactions, widens the magnetic hysteresis loop, and increases both coercive and saturation fields. Graphene honeycomb nanostructures exhibit a larger variation due to their more stable and ordered structure.

Figure 4 compares the hysteresis loops corresponding to the graphene honeycomb (a) and pentagraphene (b) nanostructures, calculated using $J = 0.1$, $D = -0.1$, and $T = 0.1$. As the biquadratic exchange coupling K increases, the magnetic hysteresis loop in the graphene honeycomb and pentagraphene nanostructures expands, leading to higher coercive (H_C) and saturation (H_S) fields, with a more pronounced effect in the graphene honeycomb. Increasing K strengthens the spin interactions, widening the hysteresis loop and enhancing the coercivity and saturation fields. The graphene honeycomb nanostructure exhibits a better response due to its more stable and ordered structure.

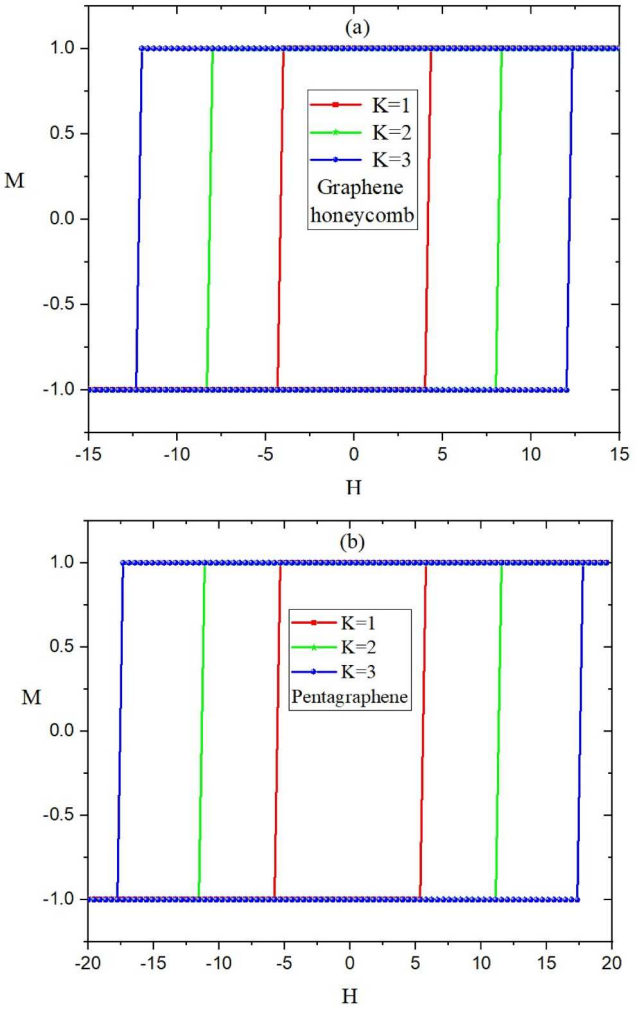

Figure 4. Hysteresis loops for Graphene honeycomb (a) and pentagraphene (b), with $J = 0.1$, $D = -0.1$ and $T = 0.1$.

Additionally, parameter K has a stronger impact on the magnetic hysteresis loop compared to parameter J. Parameter K has a stronger impact on the magnetic hysteresis loop than J due to its influence on nonlinear spin interactions, which widens the loop and increases the coercive and saturation fields.

Figure 5 compares the hysteresis loops corresponding to Graphene honeycomb (a) and pentagraphene (b) nanostructures, computed using $J = 0.1$, $D = -0.1$ and $K = 0.1$. As T increases, the hysteresis loop area decreases in both nanostructures, leading to a reduction in H_C and an increase in H_S, except at $T = 0.1$, where strong exchange interactions and anisotropy maintain a high H_C, deviating from the typical trend.

The hysteresis loops of both nanostructures disappear at $T = 4.0$. This indicates that the system has already reached or exceeded the transition temperature, i.e. the temperature at which it loses its ferromagnetic state and enters the paramagnetic phase. The

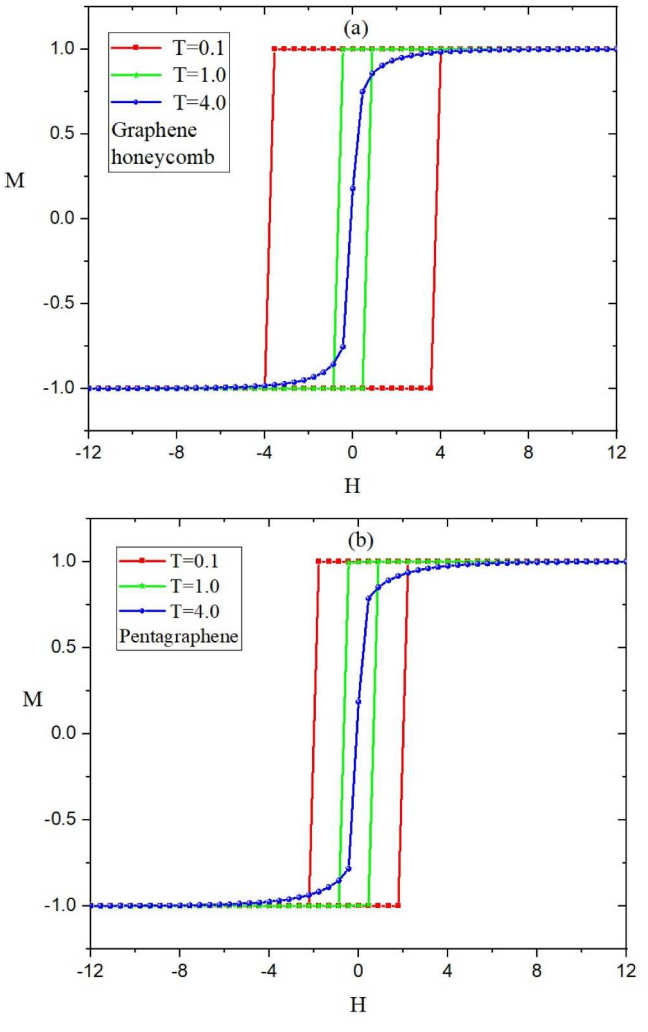

Figure 5. Hysteresis loops for Graphene honeycomb (a) and pentagraphene (b), with $J = 0.1$, $K = 0.1$ and $D = -0.1$.

narrower hysteresis loops at $T = 1.0$ suggest that this transition likely began well before $T = 4.0$. Thermal fluctuations become sufficient to disrupt spin alignment well before the complete disappearance of the loop, which explains the gradual decrease in coercive force (H_C) with increasing temperature. We will correct the sentence to better reflect this physical reality. The description will be reworded to indicate that the transition to the paramagnetic phase begins at lower temperatures and ends at $T \geq 4.0$.

Figure 6 compares the hysteresis loops corresponding to Graphene honeycomb (a) and pentagraphene (b) nanostructures, computed using $J = 0.1$, $K = 0.1$ and $T = 0.1$. As the crystal field D decreases, the magnetic hysteresis loop expands in both nanostructures, resulting in higher coercive and saturation fields (H_C and H). This effect of D is consistent in both H_C and H_S fields for both nanostructures. As D decreases, the magnetic hysteresis loop widens, increasing the coercive and saturation fields (H_C and H_S)

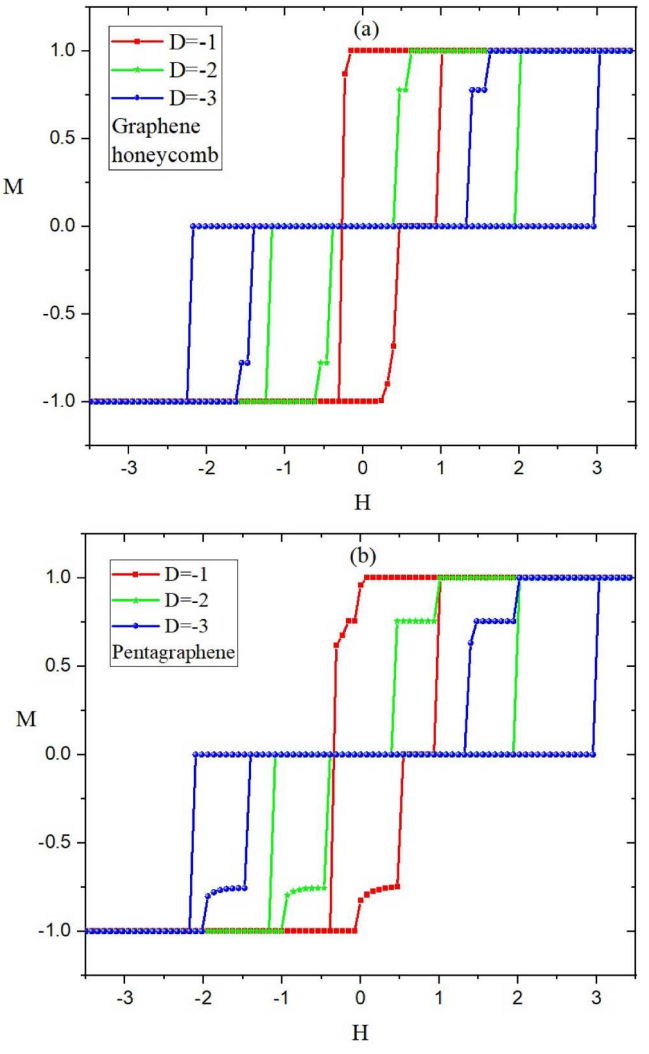

Figure 6. Hysteresis loops for Graphene honeycomb (a) and pentagraphene (b), with $J = 0.1$, $K = 0.1$ and $T = 0.1$.

similarly in both nanostructures. Moreover, that decreasing of D widens the hysteresis loops and significantly increases H_C and H, reflecting a strong dependence of the magnetic anisotropy on D. A high D favours the alignment of spins in a single direction and leads to narrow loops. In contrast, for low values of D, especially in the honeycomb nanostructure, the presence of multiple loops reflects the coexistence of distinct metastable states. These required the crossing of different magnetic fields, generating multiple loops. This behaviour highlights the complexity of magnetisation dynamics and confirms the determining role of the crystal field in modulating magnetic transitions at the nanoscale.

Figure 7 displays the coercive field (H_C) for Graphene honeycomb and pentagraphene nanostructures, computed using $K = 0.1$, $D = -0.1$ and $T = 0.1$ with varying J (a); $J = 0.1$,

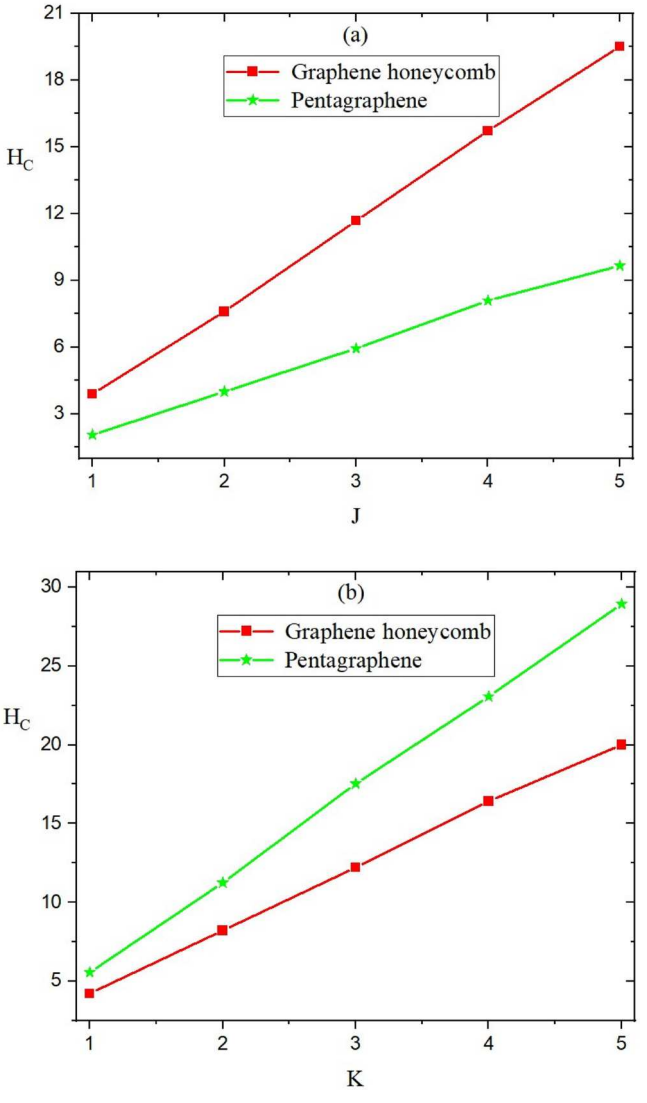

Figure 7. H_C for Graphene honeycomb and pentagraphene nanostructures, computed using $K = 0.1$, $D = -0.1$ and $T = 0.1$ with varying J (a); $J = 0.1$, $D = -0.1$ and $T = 0.1$ with varying K (b); $J = 0.1$, $K = 0.1$ and $D = -0.1$ with varying T (c); $J = 0.1$, $K = 0.1$ and $T = 0.1$ with varying D (d).

$D = -0.1$ and $T = 0.1$ with varying K (b); $J = 0.1$, $K = 0.1$ and $D = -0.1$ with varying T (c); $J = 0.1$, $K = 0.1$ and $T = 0.1$ with varying D (d). As the exchange couplings (J, K) increase and the crystal field (D) decreases, the coercive field (H_C) increases in both nanostructures almost linearly, with a stronger effect in the graphene honeycomb than in the pentagraphene. The effect of D is consistent in H_C field for both nanostructures. Conversely, H_C decreases with temperature (T) until reaching zero, marking the transition to the superparamagnetic phase. This transition occurs at $T \geq 2$ for graphene honeycomb and $T \geq 3$ for pentagraphene, indicating a higher thermal stability in pentagraphene due to differences in exchange interactions, anisotropy, or lattice effects.

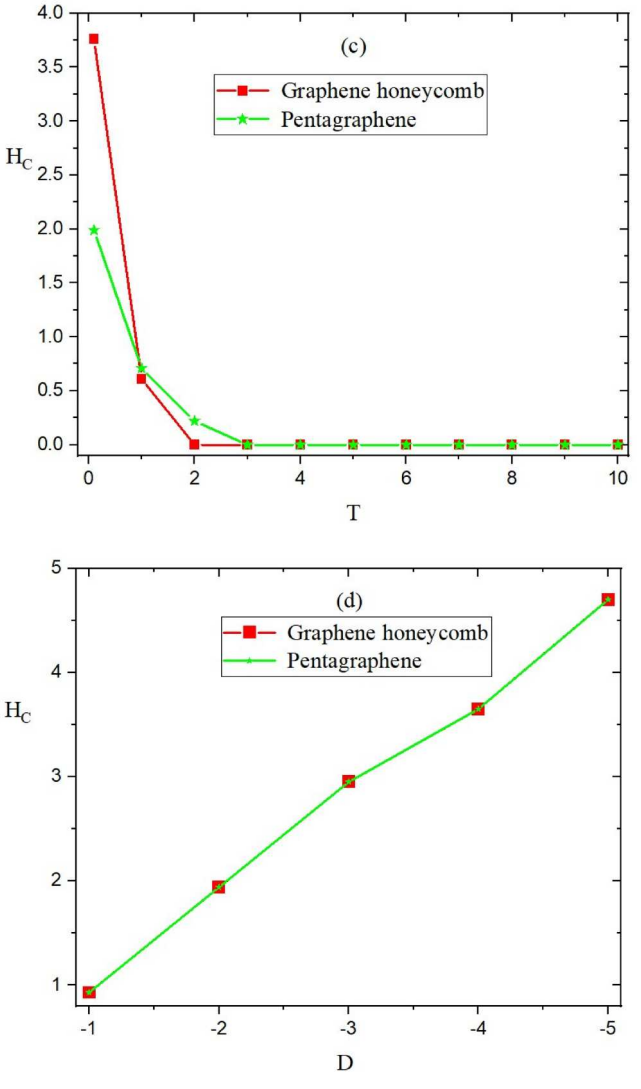

Figure 7 *Continued*

In summary, the coercive field is strongly influenced by the exchange couplings (J and K), the crystal field (D) and the temperature (T). Increasing J promotes parallel spin alignment and raises the energy barrier required for magnetisation reversal, which increases H_C. The biquadratic coupling (K), by strengthening nonlinear interactions, widens the loop even more and has a more pronounced impact on H_C than J. Regarding D, lower values lead to higher H_C, because the low anisotropy allows several metastable states to coexist, requiring different external fields to overcome them. Finally, increasing T reduces H_C: thermal fluctuations facilitate spin reorientation, and beyond the transition temperature, hysteresis disappears completely.

Figure 8 displays the saturation field (H_S) for Graphene honeycomb and pentagraphene nanostructures, computed using $K = 0.1$, $D = -0.1$ and $T = 0.1$ with varying J (a); $J = 0.1$, $D = -0.1$ and $T = 0.1$ with varying K (b); $J = 0.1$, $K = 0.1$ and $D = -0.1$ with

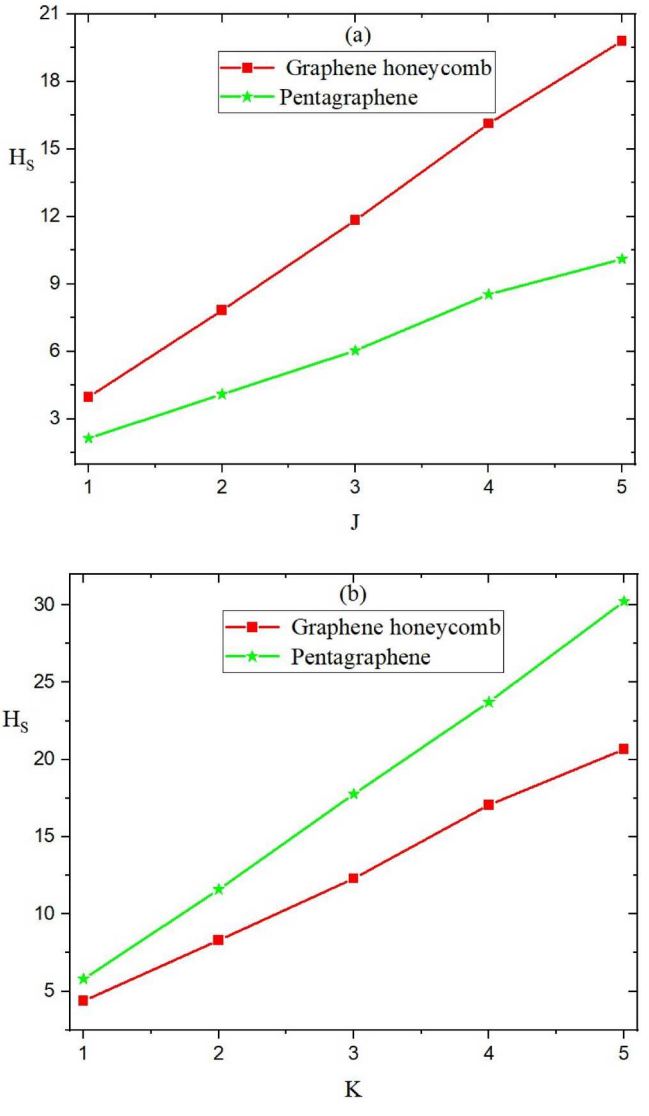

Figure 8. H_S for Graphene honeycomb and pentagraphene nanostructures, computed using $K = 0.1$, $D = -0.1$ and $T = 0.1$ with varying J (a); $J = 0.1$, $D = -0.1$ and $T = 0.1$ with varying K (b); $J = 0.1$, $K = 0.1$ and $D = -0.1$ with varying T (c); $J = 0.1$, $K = 0.1$ and $T = 0.1$ with varying D (d).

varying T (c); $J = 0.1$, $K = 0.1$ and $T = 0.1$ with varying D (d). As the exchange couplings (J, K), temperature (T) increase and the crystal field (D) decreases, the saturation field (H) rises in both nanostructures almost linearly, with a stronger effect in graphene honeycomb than in pentagraphene. In particular, as T increases, H_S generally increases, except at $T = 0.1$, where strong exchange interactions and anisotropy maintain a low H_S, deviating from the typical trend. Additionally, the effect of D on H_S is consistent for both nanostructures. In summary, the saturation field depends on J, K and D. Higher values of J and especially K increase the stability of the magnetic order and necessarily require a higher external field to reach saturation, which increases H_S. The influence

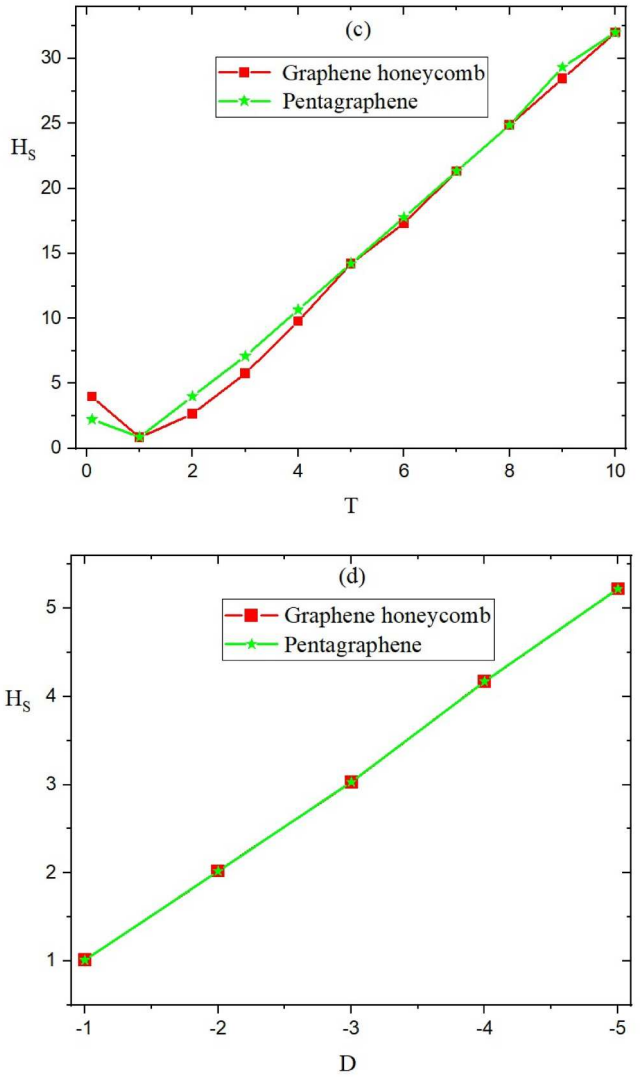

Figure 8 *Continued*

of D is inverse: a strong anisotropy (high D) orients the spins in a preferential direction and reduces H_S, while a decrease in D widens the loop and increases H_S. As for temperature, its increase tends to reduce H_S due to the increasing role of thermal fluctuations that limit the complete alignment of the spins. These results confirm that H_S, like H_C, is modulated by the competition between exchange interactions, anisotropy and thermal agitation.

4. Conclusions

This study compared the hysteresis properties of graphene honeycomb and pentagraphene nanostructures using Monte Carlo simulations, based on the Blume-Emery-Griffiths model, focusing on the coercive (H_C) and saturation (H_S) fields. The results showed that

the graphene honeycomb exhibited higher H_C and H_S due to its more ordered lattice structure, which promoted stronger spin alignment. Both the exchange couplings (J, K) and the crystal field (D) enhanced the hysteresis loop, with K having a stronger impact than J. The temperature dependence revealed a typical decrease in H_C, leading to a transition to the superparamagnetic phase at $T \geq 2$ for graphene honeycomb and $T \geq 3$ for pentagraphene, indicating greater thermal stability in the latter. Interestingly, H_S generally increased with temperature, except at $T = 0.1$, where strong exchange interactions and anisotropy maintained a lower H_S. These results highlighted the crucial role of the lattice structure in magnetic behaviour and provided insights into the tunability of these nanostructures for potential applications in spintronics and magnetic storage technologies.

Acknowledgements

The authors extend their appreciation to Taif University, Saudi Arabia, for supporting this work through project number (TU-DSPP-2024 −51).

Disclosure statement

No potential conflict of interest was reported by the author(s).

Funding

This research was funded by Taif University, Saudi Arabia, Project No**.** (TU-DSPP-2024-51). Also, this research was supported by the National Research Foundation of Korea (NRF) grant funded by the Korea government (MSIT) (RS-2025-22222973) and with the support of the '2024 System Semiconductor Technology Development Support Project' of Chungbuk Technopark.

Data availability statement

All data that support the findings of this study are included within the article.

References

[1] A. Armano and S. Agnello, Two-dimensional carbon: A review of synthesis methods, and electronic, optical, and vibrational properties of single-layer graphene. C **5** (2019), pp. 67.
[2] G.R. Bhimanapati, Z. Lin, V. Meunier, Y. Jung, J. Cha, S. Das, D. Xiao, Y. Son, M.S. Strano, V.R. Cooper, and L. Liang, *Recent advances in two-dimensional materials beyond graphene*. ACS Nano **9** (2015), pp. 11509–11539.
[3] T. Das and J.H. Ahn, *Development of electronic devices based on two-dimensional materials*. FlatChem **3** (2017), pp. 43–63.
[4] E.C. Ahn, *2D materials for spintronic devices*. npj 2D Mater Appl **4** (2020), pp. 17.
[5] F.R. Fan, R. Wang, H. Zhang, and W. Wu, *Emerging beyond-graphene elemental 2D materials for energy and catalysis applications*. Chem. Soc. Rev **50** (2021), pp. 10983–11031.
[6] G. Fiori, F. Bonaccorso, G. Iannaccone, T. Palacios, D. Neumaier, A. Seabaugh, S.K. Banerjee, and L. Colombo, *Electronics based on two-dimensional materials*. Nature Nanotech **9** (2014), pp. 768–779.
[7] N. Ashraf, M. Isa khan, A. Majid, M. Rafique, and M.B. Tahir, *A review of the interfacial properties of 2-D materials for energy storage and sensor applications*. Chin. J. Phys. **66** (2020), pp. 246–257.

[8] M.K. Aslam, T.S. AlGarni, M.S. Javed, S.S.A. Shah, S. Hussain, and M. Xu, *2D MXene materials for sodium Ion batteries: A review on energy storage*. Journal of Energy Storage **37** (2021), pp. 102478.
[9] V. Babar, S. Sharma, and U. Schwingenschlögl, *New paradigm for gas sensing by two-dimensional materials*. J. Phys. Chem. C **123** (2019), pp. 13104–13109.
[10] A. Bolotsky, D. Butler, C. Dong, K. Gerace, N.R. Glavin, C. Muratore, J.A. Robinson, and A. Ebrahimi, *Two-dimensional materials in biosensing and healthcare: from In vitro diagnostics to optogenetics and beyond*. ACS Nano **13** (2019), pp. 9781–9810.
[11] M.J. Allen, V.C. Tung, and R.B. Kaner, *Honeycomb carbon: A review of graphene*. Chem. Rev **110** (2010), pp. 132–145.
[12] A.K. Geim and K.S. Novoselov, The rise of graphene. Nanoscience and Technology **6** (2009), pp. 183–191.
[13] M. Balvasi, A. Avazpour, J. Jalilian, and M.Z. Bidsardare, *Tuning the electronic and transport properties of three configurations of penta-graphene nanoribbons*. Acta Phys Pol A **144** (2023), pp. 214–225.
[14] M.A. Nazir, A. Hassan, Y. Shen, and Q. Wang, *Research progress on penta-graphene and its related materials: properties and applications*. Nano Today. **44** (2022), pp. 101501.
[15] R.L. Comstock, *Review modern magnetic materials in data storage*. J Mater Sci: Mater Electron. **13** (2002), pp. 509–523.
[16] D.A. Thompson and J.S. Best, *The future of magnetic data storage techology*. IBM J Res Dev. **44** (2000), pp. 311–322.
[17] S.P. Gubin, Y.I. Spichkin, G.Y. Yurkov, and A.M. Tishin, Nanomaterial for high-density magnetic data storage. Russian Journal of Inorganic Chemistry C/C of Zhurnal Neorganicheskoi Khimii **47** (2002), pp. S32–S67.
[18] D. Joksas, A. AlMutairi, O. Lee, M. Cubukcu, A. Lombardo, H. Kurebayashi, A.J. Kenyon, and A. Mehonic, *Memristive, spintronic, and 2D-materials-based devices to improve and complement computing hardware*. Adv Intell Syst **4** (2022), pp. 2200068.
[19] B.K. Chakrabarti and M. Acharyya, *Dynamic transitions and hysteresis*. Rev Mod Phys **71** (1999), pp. 847–859.
[20] F. Fiorillo, C. Appino, and M. Pasquale, Hysteresis in magnetic materials, in *The science of hysteresis*, G. Bertotti, I.D. Mayergoyz, eds., Elsevier, Amsterdam, 2006. pp. 1–190. doi:10.1016/B978-012480874-4/50019-1.
[21] N. Metropolis and S. Ulam, *The monte carlo method*. J. Am. Stat. Assoc. **44** (1949), pp. 335–341.
[22] S. Cho, *Metropolis–hastings algorithm for ising model*, in *Monte Carlo Simulations Using Microsoft EXCEL®*, Cho S., ed., Springer International Publishing, Cham, 2023. pp. 93–121.
[23] Y.L. Wang, F. Lee, and J.D. Kimel, *Phase diagrams of the spin-1 Ising Blume-Emery-Griffiths model: Monte Carlo simulations*. Phys. Rev. B **36** (1987), pp. 8945–8947.
[24] A.N. Berker and M. Wortis, *Blume-Emery-Griffiths-Potts model in two dimensions: phase diagram and critical properties from a position-space renormalization group*. Phys. Rev. B **14** (1976), pp. 4946–4963.
[25] W. Hoston and A.N. Berker, *Multicritical phase diagrams of the blume-emery-griffiths model with repulsive biquadratic coupling*. Phys. Rev. Lett **67** (1991), pp. 1027–1030.
[26] G.B.A. Goguin, T.D. Oke, R.A.A. Yessoufou, and E. Albayrak, *Critical and hysteresis behaviors for a hexagonal core-shell structure nanowire in the blume–emery–griffiths model*. Physica A **624** (2023), pp. 128927.
[27] R. El Fdil, H. Sabbah, A.A. Alsayyari, Z. Fadil, C.J. Raorane, S.C. Kim, S. Saadaoui, E. Salmani, and H. and Ez-Zahraouy, *Monte carlo investigation of hysteresis cycles and magnetization plateau in C60 fullerene-like system using the blume–emery–griffiths model*. Int. J. Theor. Phys. **64** (2025), pp. 109.
[28] G.B. Aziza Goguin, R.A.A. Yessoufou, T.D. Oke, and E. Albayrak, *Monte Carlo and mean-field studies on the magnetic properties of a hexagonal ising nanowire with core-shell structure in the Blume–Emery–Griffiths model*. J. Magn. Magn. Mater. **598** (2024), pp. 172071.

[29] S.S. Ahmed, L. Bahmad, A. El Yousfi, A. Benyoussef, A. El Kenz, and A.G. El Hachimi, *Mixed spin-1 and spin-3/2 Blume-Emery-Griffiths model with external field on a honeycomb lattice*. Superlattices Microstruct. **123** (2018), pp. 1–11.
[30] H.P. Dong and S.L. Yan, *Magnetic properties of the bond and crystal field dilution Blume–Emery–Griffiths model in the presence of magnetic field*. Solid State Commun. **139** (2006), pp. 406–411.
[31] A. Jabar and R. Masrour, *Magnetic properties of magnetic Bilayer Kekulene structure: A Monte Carlo study*. Phys. B **539** (2018), pp. 21–28.
[32] H. Magoussi, A. Zaim, and M. Kerouad, *Monte carlo simulation of the magnetic properties of a spin-1 blume–capel nanowire*. Solid State Commun. **200** (2014), pp. 32–41.
[33] H. Kerrai, A. Zaim, and M. Kerouad, *Magnetic energy product and hysteresis behavior of anti-perovskite Mn3AlN: Monte Carlo simulation*. Phys. Scr. **99** (2024), pp. 065986.
[34] Z. Fadil, A. Mhirech, B. Kabouchi, L. Bahmad, and W. Ousi Benomar, *Magnetic properties of naphthalene-like nano-structure with RKKY interactions: Monte Carlo simulations*. Chin. J. Phys. **64** (2020), pp. 295–304.
[35] N. Saber, Z. Fadil, A. Mhirech, B. Kabouchi, and L. Bahmad, *Magnetic properties and thermal behavior of the monolayer rubrene-like nano-island: Monte Carlo simulations*. Solid State Commun. **362** (2023), pp. 115084.
[36] Z. Fadil, N. Saber, H. Eraki, A. Mhirech, B. Kabouchi, and L. Bahmad, *Magnetic properties and compensation temperature of a mixed monolayer coronene-like nanostructure: Monte Carlo study*. SPIN **12** (2022), pp. 2250020.
[37] W. Selke and J. Yeomans, *Interface properties of the two-dimensional blume-emery-griffiths model*. J. Phys. A: Math. Gen. **16** (1983), pp. 2789.
[38] R. Masrour, A. Jabar, A. Benyoussef, and M. Hamedoun, *Monte carlo simulation of magnetic properties of a mixed spin-1 and spin-3/2 ferrimagnetic ising system*. Chem. Phys. Lett. **631** (2015), pp. 92–96.
[39] Z.Y. Liu, W. Wang, and B.C. Li, *Monte Carlo study of the magnetic and magnetocaloric properties of an edge-decorated graphene-like nanoparticle*. J. Mater. Sci. **59** (2024), pp. 13908–13930.
[40] M. Yang, W. Wang, B.C. Li, H.J. Wu, S.Q. Yang, and J. Yang, *Magnetic properties of an ising ladder-like graphene nanoribbon by using monte carlo method*. Physica A **539** (2020), pp. 122932.

Philosophical Magazine

ISSN: 1478-6435 (Print) 1478-6443 (Online) Journal homepage: www.tandfonline.com/journals/tphm20

Understanding the effect of grain boundary solute segregation on the creep behaviour of thermally stable nanocrystalline materials: a theoretical approach

I. Wani, N. Rai, K. L. Murty & S. Gollapudi

To cite this article: I. Wani, N. Rai, K. L. Murty & S. Gollapudi (2024) Understanding the effect of grain boundary solute segregation on the creep behaviour of thermally stable nanocrystalline materials: a theoretical approach, Philosophical Magazine, 104:24, 1191-1206, DOI: 10.1080/14786435.2024.2383252

To link to this article: https://doi.org/10.1080/14786435.2024.2383252

PHILOSOPHICAL MAGAZINE
2024, VOL. 104, NO. 24, 1191–1206
https://doi.org/10.1080/14786435.2024.2383252

Taylor & Francis
Taylor & Francis Group

Understanding the effect of grain boundary solute segregation on the creep behaviour of thermally stable nanocrystalline materials: a theoretical approach

I. Wani [a], N. Rai [a,b], K. L. Murty[c] and S. Gollapudi[a]

[a]School of Minerals, Metallurgical and Materials Engineering, Indian Institute of Technology Bhubaneswar, Bhubaneswar, India; [b]Department of Mechanical and Industrial Engineering, University of Illinois, Chicago, IL, USA; [c]Department of Nuclear Engineering, North Carolina State University, Raleigh, NC, USA

ABSTRACT

In this work, we provide a theoretical framework to evaluate the beneficial effect of solute segregation on the creep behaviour of nanocrystalline materials. We choose copper as the model system and employ the Murdoch and Schuh model to identify Cu–3Zr as a binary system with high thermal stability in its nanocrystalline state. The effect of the segregation of Zr on the grain boundary diffusivity was evaluated using the Hondros and Henderson model. The effect of solute segregation on threshold stress for vacancy emission and absorption at the grain boundaries was evaluated using the Mohamed model. Using these in conjunction with the Bird Mukherjee Dorn equation for creep allowed us to compare the diffusional creep behaviour of nc copper and nc Cu–3Zr. The nc Cu–3Zr system with a grain size of 49 nm demonstrated a higher creep resistance compared to nc Cu bearing a similar grain size. However, the creep resistance of both systems was found to be significantly inferior when compared to the conventional coarse-grained Cu bearing a grain size of 1 µm.

ARTICLE HISTORY
Received 10 May 2023
Accepted 12 July 2024

KEYWORDS
Nanocrystalline; creep; thermal stability; Cu–Zr; solute segregation

1. Introduction

For a long time nanocrystalline materials, despite their high hardness and wear resistance, had not garnered widespread commercial applications. This was because of their poor thermal stability [1–3]. Recent works by Murdoch and Schuh [4] and Darling et al. [5,6] have demonstrated the efficacy of thermodynamics guided design of stable nanostructured materials. A key premise herein is the segregation of the chosen solute at the grain boundaries of the solvent or the parent element [7,8]. This in turn is expected to reduce the overall free energy of the system leading to a high degree of thermal stability in the nanocrystalline state [9].

CONTACT S. Gollapudi srikantg@iitbbs.ac.in School of Minerals, Metallurgical and Materials Engineering, Indian Institute of Technology Bhubaneswar, Argul, Jatni, Bhubaneswar, Odisha 752050, India
Supplemental data for this article can be accessed online at https://doi.org/10.1080/14786435.2024.2383252.

Creep behaviour of thermally stable nanocrystalline materials is a relatively unexplored area [10], both experimentally and theoretically. The solute segregated at the grain boundary, by way of its effect on vacancy emission and absorption at the grain boundary, is expected to influence the creep behaviour of the material. A related point is the effect the solute atom has on the grain boundary diffusivity, the diffusivity being a key contributor to the kinetics of creep deformation [11].

In this work, we address these aspects by developing a theoretical framework to understand the effect of solute segregation on creep behaviour of nanocrystalline materials. This framework relies on the nanostructure stability criterion proposed by Murdoch and Schuh [4], employs model for grain boundary diffusivity under segregated state proposed by Hondros and Henderson [11] and utilises the constitutive equation for creep deformation proposed by Bird–Mukherjee–Dorn [12].

2. Approach

The approach taken is as follows: (i) first we identify a thermally stable nanocrystalline system using the Murdoch–Schuh equations. (ii) We then evaluate the effect of solute addition on grain boundary and lattice diffusivity. (iii) Finally, we employ creep constitutive equations for evaluating the creep behaviour of nanocrystalline materials and compare the same against the creep behaviour of its conventional counterpart.

Murdoch and Schuh [4] proposed the following equation to evaluate the free energy of a binary nanocrystalline system

$$\Delta G_{mix} = (1 - f_{gb})\Delta G_c + f_{gb}\Delta G_{gb} + zvf_{gb}(X_{gb} - X_c)\left[(2X_{gb} - 1)\omega_{gb} - \frac{1}{zt}(\Omega_A \gamma_A - \Omega_B \gamma_B)\right] \quad (1)$$

where z is the coordination number of solvent, v is the transitional bond fractions, Ω_A and Ω_B are the atomic volumes of A and B respectively, γ_A and γ_B are the respective grain boundary energies of the solute and solvent, f_{gb} is the grain boundary fraction, t is the grain boundary thickness, ω_c and ω_{gb} are the crystal and grain boundary interaction factors respectively, and X_{gb} and X_c are the solute concentration at the grain boundary and inside the crystal respectively. For a given solute concentration X, the solute will partition between the grain boundary and crystal in such a way that the overall free energy of the system is minimised. The relation between X, X_{gb} and X_c is given by

$$X = X_{\mathrm{gb}}.f_{\mathrm{gb}} + X_{\mathrm{c}}.(1 - f_{\mathrm{gb}}) \quad (2)$$

The grain boundary fraction, f_{gb}, is dependent on grain size (d) and this makes ΔG_{mix} in Equation (1), dependent on grain size. To determine the grain size, d,

and grain boundary solute concentration X_{gb} at which ΔG_{mix} will attain its minimum value, we vary the value of d from 1 to 100 nm and the value of X_{gb} is varied from 0.01 to 0.99 with a step size of 0.01. The values of f_{gb}, ΔG_c, ΔG_{gb}, X_c, ω_c , ω_{gb} in Equation (1) are determined from the procedure suggested in [4,13]. Following this, ΔG_{mix} is plotted against X_{gb} & d in a three-dimensional plot and minima in the free energy profile indicates a thermally stable nanocrystalline system [4]. Herein, we would like to mention that although other factors such as grain size distribution [14] and crystallographic texture [15] are known to influence the thermal stability of the nanocrystalline materials, we are ignoring the effects of the same in this particular study.

In our work, we choose copper as the model system and used the above-mentioned approach to identify zirconium as the solute atom capable of stabilising the nanostructure of copper. Figure 1(a) provides the (ΔG_{mix}) of a Cu–3Zr system which reveals the free energy profile has a minimum corresponding

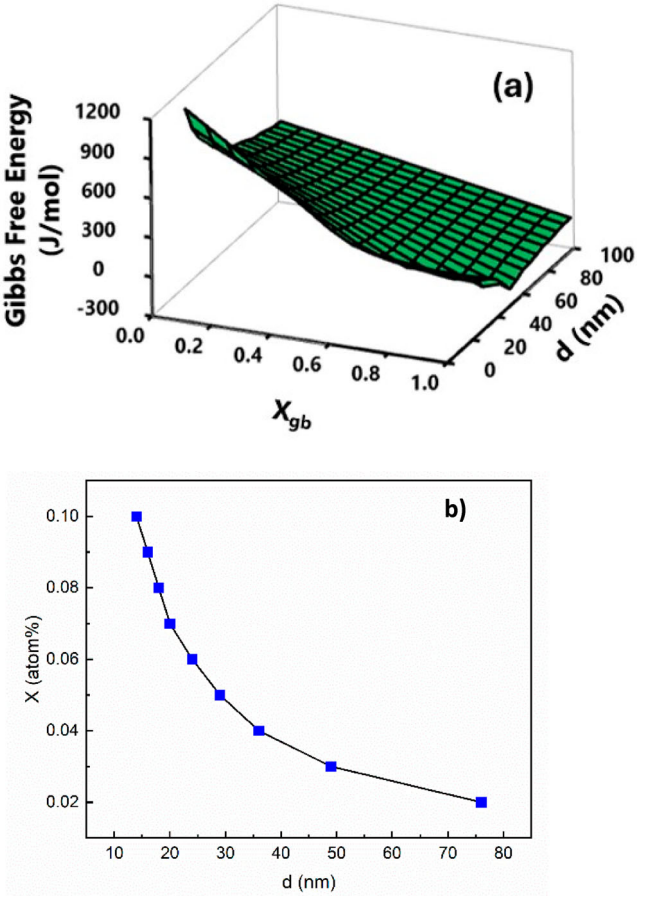

Figure 1. (a) The variation of Gibbs free energy of the alloy (ΔG_{mix}) as a function of Xgb and grain size d for the Cu–3Zr system. (b) The amount of solute X required for achieving a stable grain size in the Cu–Zr system.

to d value of 49 nm for a X_{gb} of 0.96 indicating the possibility of high thermal stability. The values of the different parameters used for developing Figure 1(a) are shown in Tables 1 and 2. This approach was employed to evaluate the free energy profile for other compositions of Cu–Zr too. Figure 1(b) reveals the effect of the solute concentration on the stable grain size which can be achieved in the Cu–Zr system and predicts that when the solute concentration is increased, the stable grain size that can be achieved in the Cu–Zr system is smaller. Hence finer grain sizes can be expected to be stabilised at higher solute concentrations.

It is important to mention herein that the Cu–3Zr system, predicted by Murdoch and Schuh, has been reported to be thermally stable by Khalajhedayati and Rupert [16]. Despite annealing for long durations at temperatures as high as 850°C, Khalajhedayati and Rupert [16] found that the material retained its initial nanostructure. Hence it can be concluded that the thermodynamic calculation for Cu–Zr system reported in this work captured its stability tendencies correctly.

We next focus on evaluating the effect of the Zr addition on the grain boundary diffusivity and lattice diffusivity of Cu. For this we employ the equations proposed by Hondros and Henderson [11] that described the effect of the solute segregation on the grain boundary diffusivity,

$$D^{*}_{gb} = D_{gb}\left(1 + \left(b_L - \frac{2}{m}\frac{a^2_{sv}}{a^2_{su}}\beta_b\right)X_c\right) \tag{3}$$

where D^{*}_{gb} is the diffusivity of the grain boundary in the presence of the solute element, D_{gb} is the grain boundary diffusivity of the parent element, a_{sv} is the atomic size of the parent element, a_{su} is the atomic size of the solute element, m relates to the number of effective atom layers in the grain boundary and β_b is the enrichment factor given by X_{gb}/X_c. The diffusivity of the lattice or

Table 1. Parameters for copper and zirconium used for constructing Figure 1(a) using Equation (1).

Parameter	Copper (Cu)	Zirconium (Zr)
Atomic Volume (Ω)	7.1×10^{-6} m^3/mol	1.40×10^{-5} m^3/mol
Grain Boundary Energy (γ)	0.6 J/m^2	0.65 J/m^2
Atomic Size (a)	1.28 Å	1.60 Å

Table 2. Parameters employed for constructing Figure 1(a) using Equation (1).

Parameter	Value
Grain Boundary Interaction Parameter (ω_{gb})	−3450 J
Bulk Interaction Parameter (ω_c)	167 J
Transitional bond fraction (v)	0.5
Grain Boundary Thickness (t)	0.5 nm
Burgers Vector Magnitude of Copper (b)	2.56 Å

crystal in the presence of the solute is given by

$$D_L^* = D_L(1 + b_L X_c) \tag{4}$$

where D_L^* is the bulk/lattice diffusivity of the alloy and D_L is the bulk/lattice diffusivity of the parent element, b_L is a constant taken as 100 for binary alloys and X_c is the concentration of the solute element within the lattice. This equation is applicable to normal solute diffusion for the dilute case. With Equations (3) and (4) in place, the effect of 3 at.% Zr addition on the grain boundary and lattice diffusivity of Cu was determined. The values of the different parameters used for these calculations are shown in Tables 3 and 4.

Following this, we direct our efforts to understand the effect of Zr addition on the creep deformation of nanocrystalline Cu. We made the following assumptions to evaluate the creep deformation rates. (1) Diffusion creep mechanisms such as Coble and Nabarro–Herring are the rate controlling mechanisms of creep deformation. In support of this assumption, we provide a review of literature on creep of nanocrystalline materials. Table 5 provides a summary of the experimental investigations and computer simulations studies on nanocrystalline materials. From Table 5, it is evident that several studies have reported Coble creep as the rate controlling mechanism of creep deformation in nanocrystalline materials. A few studies have also reported Nabarro–Herring creep as a possible mechanism of creep in these materials. A couple of studies have reported Interface controlled Coble creep as rate controlling mechanism in these materials. Interface controlled creep is believed to arise when the grain boundaries are no longer perfect sources and sinks of vacancies. Such a situation may arise when impurity atoms segregate at the grain boundaries.

Table 3. Value of parameters used for evaluating the effect of Zr segregation on diffusivity.

Parameter	Value
Grain Boundary Diffusion Coefficient (D_{0gb})	1×10^{-5} m^2/s
Lattice Diffusion Coefficient (D_{0L})	2×10^{-5} m^2/s
Grain Boundary Activation Energy (Q_{gb})	104 kJ/mol
Lattice Activation Energy (Q_L)	197 kJ/mol
M	2
Enrichment Factor (β_b) (for 49 nm grain size)	1.57×10^3

Table 4. Values of X_{gb} and X_c for different grain sizes.

Solute Concentration(X)	Grain Boundary Solute Concentration ($\boldsymbol{X_{gb}}$)	Grain Size (nm)	Lattice Solute Concentration ($\boldsymbol{X_c}$)
0.03	0.96	49	0.612×10^{-3}
0.05	0.95	29	0.667×10^{-3}
0.07	0.95	20	0.701×10^{-3}

Table 5. Summary of experimental investigations and molecular dynamics simulations studies on creep of nanocrystalline materials.

Study type	Material	Initial grain size (nm)	n (stress exponent)	Q (kJ/mol)	Q_{gb}	Q_L	Mechanism (creep)	Reference
Exp.	Ni–P	28	1.2	69	✓	X	Coble	[17]
Exp.	Ni	6,20,40	1.1, 2, 5.5	—	—	—	Coble, GBS, DC	[18]
Exp.	Fe–B–Si	27	1.2	144	✓	X	Coble	[19]
Exp.	Y-SZP	40	1.4	660	X	✓	NH	[20]
Exp.	Cu	30	—	69	✓	X	ICCC	[21]
Exp.	Ni	30	1,6.5	—	—	—	Coble, DC	[22]
Exp.	Cu	26	1,4.12	—	—	—	Coble, DC	[23]
Exp.	ZrO_2-Y	65–350	3	—	—	—	ICCC	[24]
Exp.	Cu	35	—	—	—	—	Coble	[25]
Exp.	CoCrFeMnNi	33	1	84	✓	X	Coble	[26]
MD	UO_2	12	—	372	✓	X	Coble	[27]
MD	Cu	8–16	1.08, 2.01	—	—	—	Coble, GBS	[28]
MD	Ni	2.8–5.6	1–3	—	—	—	Coble, NH, GBS, DC	[29]
MD	W	2.38–2.86, 3.57–4.76	3.43–4.22, 2.24–3.36	—	—	—	Coble, NH, GBS, DC	[30]
MD	TiAl	3.8–6.6	—	—	—	—	Coble, NH, DC	[31]
MD	FeCrAl	3.7–17.8	1.16–7.15	—	—	—	Coble, GBS, DC	[32]

GBS: Grain boundary sliding; **DC:** Dislocation creep; **NH:** Nabarro–Herring creep; **ICCC:** Interface controlled Coble creep.

Table 5 thus validates our assumption regarding diffusion creep as the dominant mechanism of creep in nanocrystalline materials; diffusion creep in nanocrystalline materials was first invoked by Chokshi et al. [33] to rationalise the inverse Hall–Petch phenomenon. The other assumptions made in our work are as follows. (2) All the grain boundaries decorating the nanostructure are low angle grain boundaries. By assuming all grain boundaries to be low angle grain boundaries, we can understand the effect of solute segregation on the threshold stress for vacancy emission/dislocation climb within the grain boundaries. (3) For the purpose of our creep calculations, nanocrystalline copper is assumed to be thermally stable. This assumption was made to allow comparison of the creep deformation rates of the stable systems, i.e. nc Cu–3Zr with that of the nc Cu system for a given grain size. (4) The applied stress does not cause any stress-assisted grain growth [34–38]. It has been reported in certain nanocrystalline systems that creep deformation could cause a change in the starting grain size of the material. However, for the purpose of our analysis, we have assumed that applied stress does not cause any changes in grain size of the material during creep deformation. With these assumptions in place, we evaluate the creep deformation rates of nc Cu, nc Cu–3Zr, both bearing a grain size of 49 nm and microcrystalline copper bearing a grain size of 1 μm.

The constitutive equation for creep deformation is given by the Bird–Mukherjee–Dorn [12] equation which is as follows:

$$\dot{\varepsilon} = \frac{AD_0Gb}{kT}\left(\frac{b}{d}\right)^p\left(\frac{\sigma}{G}\right)^n e^{-\frac{Q}{RT}} \tag{5}$$

where $\dot{\varepsilon}$ is the strain rate of creep deformation, A is a constant corresponding to the specific mechanism of creep, D_0 is the diffusion coefficient, G is the shear modulus of the material at the test temperature, T is temperature, k is Boltzmann's constant (1.38×10^{-23}) J/K, b is the Burgers vector, d is the grain size, σ is the applied stress, p is the grain size exponent, n is the stress exponent, R is the universal gas constant and Q is the activation energy for the particular rate controlling mechanism.

From Table 5, it is clear that Coble creep is generally the rate controlling mechanism in these materials. However, for the purpose of our calculations we have considered both Coble and N–H creep as possible rate controlling mechanisms considering that both have a strong grain size dependence; Coble has a p value of 3 and N–H creep has a p value of 2. Also, for Coble creep grain boundary diffusivity ($Q = Q_{gb}$) is applicable and for N–H creep lattice diffusivity ($Q = Q_L$) is applicable and $n = 1$ for both mechanisms. Here Q_{gb} is the grain boundary diffusion activation energy and Q_L is the lattice diffusion activation energy.

Considering the fact that Coble and NH creep are parallel mechanisms, the total creep rate of deformation of the nanocrystalline material can then be

described by

$$\dot{\varepsilon}_{\mathrm{T}} = \dot{\varepsilon}_{\mathrm{Coble}} + \dot{\varepsilon}_{\mathrm{NH}} \tag{6}$$

which expands to

$$\dot{\varepsilon}_{Coble} + \dot{\varepsilon}_{NH} = \frac{150 D_{gb} G b}{kT}\left(\frac{b}{d}\right)^{3}\left(\frac{\sigma}{G}\right)^{1} + \frac{12 A D_{L} G b}{kT}\left(\frac{b}{d}\right)^{2}\left(\frac{\sigma}{G}\right)^{1} \tag{7}$$

Generally during the evaluation of diffusion creep, the grain boundaries are assumed to be perfect sources and sinks for vacancies. This assumption is valid for pure systems such as elemental nc Cu. However, with solute atoms segregated at the grain boundaries, this assumption may not be valid anymore and hence a threshold stress term will have to be introduced in Equation (7). The threshold stress σ_0 basically indicates that for applied stresses lower than σ_0, creep deformation will not ensue. Hence Equation (7) can be modified to account for creep in nc Cu–3Zr alloy.

$$\dot{\varepsilon}_{Coble} + \dot{\varepsilon}_{NH} = \frac{150 D^{*}_{gb} G b}{kT}\left(\frac{b}{d}\right)^{3}\left(\frac{\sigma - \sigma_0}{G}\right)^{1} + \frac{12 A D^{*}_{L} G b}{kT}\left(\frac{b}{d}\right)^{2}\left(\frac{\sigma - \sigma_0}{G}\right)^{1} \tag{8}$$

All the terms, except for σ_0, mentioned in Equations (7) and (8) are known quantities. The values of these quantities are mentioned in the supplementary section. However, σ_0 has to be evaluated and the same can be determined from the equations proposed by Mohamed [39]

$$\frac{\sigma_o}{G} = B\, exp\left(\frac{|W|}{kT}\right) \tag{9}$$

where B is a constant and W is the binding energy. The threshold stress term was developed by Mohamed [39] for the segregation of solute atoms at low angle grain boundaries wherein B is found to be

$$B = \frac{c_o W}{b b_b^2 G} \tag{10}$$

Here c_0 is the solute concentration corresponding to $W = 0$ and b_b is the Burgers vector of dislocations within the grain boundary taken as 1.56b [40]. The binding energy W can be obtained from the chemical, elastic and electrical interactions between the solute and the solvent atoms as noted in the work of Fiore and Bauer [41]

$$W = U_{\mathrm{elastic}} + U_{\mathrm{chemical}} + U_{\mathrm{electrical}} \tag{11}$$

where

$$U_{edge}^{elastic} = \left(\frac{4}{3}\right) \mathrm{G} \epsilon \mathrm{b} r_0^3 \frac{(1+\vartheta)}{(1-\vartheta)} \frac{\sin\theta}{\mathrm{r}} \tag{12}$$

However, when a screw dislocation occurs, the elastic interaction is about l/5 of that of an edge dislocation.

$$U^{electrical} = 0.0175(\mathrm{Z}-1)\mathrm{b}\frac{\sin\theta}{\mathrm{r}} \tag{13}$$

$$U^{chemical} = 1.6 \times 10^{-21} J \tag{14}$$

Here, r_0 is the radius of solvent, ϵ misfit parameter, r is the radial distance from the centre of the dislocation core to the solute atom, ϑ is the Poisson's ratio, θ is the angle (measured clockwise) between the slip plane of the dislocation and the radial vector, Z is the valency of solute in solvent. The values of these are as follows: $r_0 = 1.28$ Å, $\epsilon = 0.25$, $r = 2.7$ Å, $\theta = 90°$, $\mathrm{Z} = 4$.

3. Results and discussion

Using Equations (9) and (10), the variations of the binding energy W and normalised threshold stress σ_0/G are plotted against temperature T in Figures 2(a) and (b) respectively. We note that the binding energy, W, as well as the normalised threshold stress σ_0/G decrease in magnitude with increasing temperature. This is indicative of the weakening of the bond between the solute and the solvent atom at higher temperatures as expected. With the knowledge of the normalised threshold stress at different temperatures, it is now possible to evaluate the creep deformation rates of the Cu–3Zr alloy for different applied stresses and temperatures. The calculated creep rate of the nc Cu–3Zr is then plotted against nc Cu and mc Cu in Figure 3(a) for a temperature of 823 K. For the purpose of these calculations, the Burgers vector of Cu was taken as 2.56 A, the Coble creep constant A_C was taken as 150 and NH creep constant A_{NH} was taken as 10 [12].

Figure 3(a) compares the creep rates obtained for nc Cu, nc Cu–3Zr and mc Cu. Please note that for Figure 3, the creep rates were calculated by using the diffusion coefficients (D_{ob} and D_{oL}) and activation energy (Q_{gb} and Q_L) values belonging to conventional microcrystalline copper. This is because of the dearth of complete experimental data on these parameters for nc Cu. It is evident from Figure 3(a) that the nc Cu–3Zr is more creep resistant compared to the nc Cu. The higher creep resistance of the Cu–3Zr alloy can be attributed to the role of Zr in reducing the grain boundary diffusivity and also to the role of the threshold stress. However, despite the beneficial role of Zr, the nc Cu–3Zr is significantly less creep resistant when compared to the mc Cu. This implies that the smaller diffusion paths in the nanograin structure of Cu–3Zr have a greater bearing on the creep rates than the barriers to diffusion creep created by the presence of the Zr atoms at the grain boundaries. Figure 3(b) is the Arrhenius plot (a semi-log plot of creep rates against the inverse of temperature) indicating that the activation energies for creep in nc Cu and nc Cu–3Zr are 96 and 101 kJ/mol respectively.

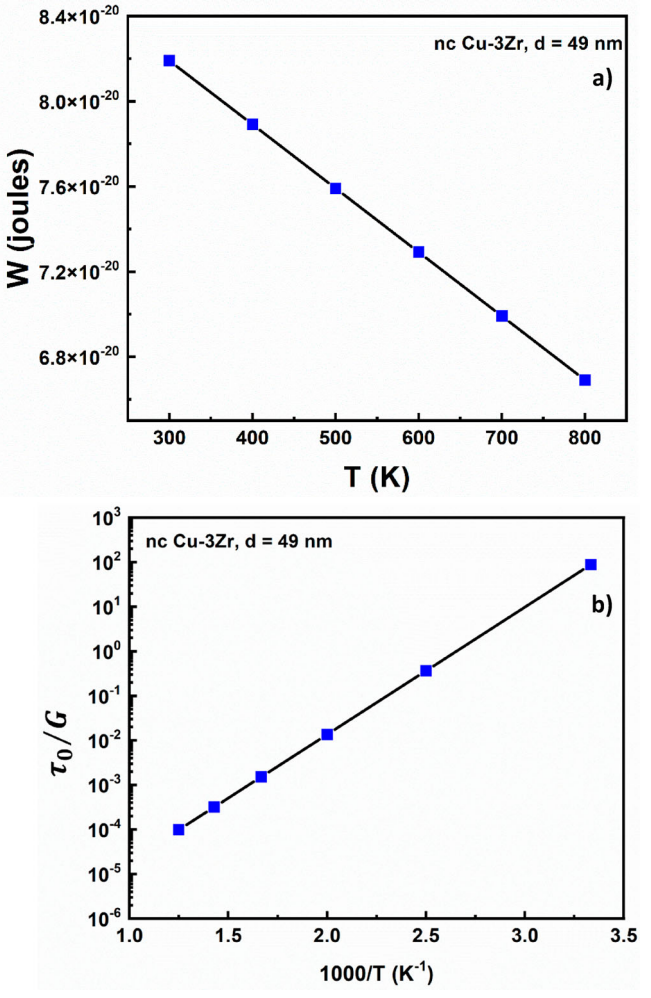

Figure 2. (a) The variation of the binding energy *W* versus temperature for the Cu–3Zr system. (b) The variation of the normalised threshold stress as a function of the inverse of temperature.

The higher, albeit small, activation energy for creep in nc Cu–3Zr alloy vis-à-vis nc Cu is suggestive of higher resistance to creep deformation in the alloy which is in accordance with the results shown in Figure 3(a). The *Q* values obtained for nc Cu are close to that of grain boundary diffusion activation energy in pure Cu [42]. This implies that the deformation in nc Cu is dominated by Coble creep which is known to proceed by grain boundary diffusion. This also implies that NH creep does not have a significant role in nc materials. Secondly the higher *Q* value exhibited by nc Cu–3Zr indicates that Zr is providing obstacles to diffusion of vacancies. However, it is to be noted that the *Q* value of nc Cu–3Zr is only marginally higher than that for nc Cu. This implies that the amount of Zr segregated at the grain boundary is not sufficient to introduce a higher resistance to creep deformation. While

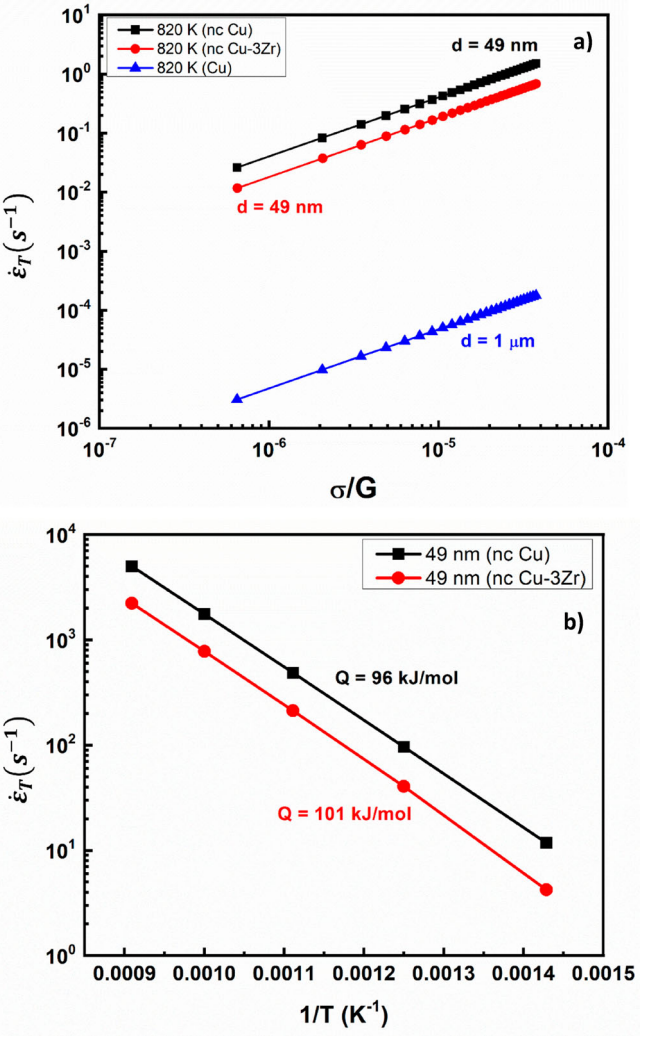

Figure 3. (a) Variation of the creep strain rate of nc Cu, nc Cu–3Zr and mc Cu as a function of normalised stress (σ/G) (b) Arrhenius plot for the determination of activation energy of creep in nc Cu and nc Cu–3Zr.

the predictions of the model regarding the relative creep resistance of nc Cu and nc Cu–3Zr alloy are on expected lines, a validation of the model predictions by comparison with experimental results is of interest. For a validation of our model, we have evaluated the creep deformation rates of nc Cu obtained from the model and compared them against experimental creep rates for nc Cu reported in literature. A similar exercise could not be conducted for nc Cu–3Zr because of the lack of experimental investigations into creep of this material. Figure 4 is a plot of the total creep strain rate against normalised stress for nanocrystalline copper. In the plot, we have shown the strain rate of creep in nc Cu obtained from literature and compared it against strain rates calculated using our model. The model calculations were

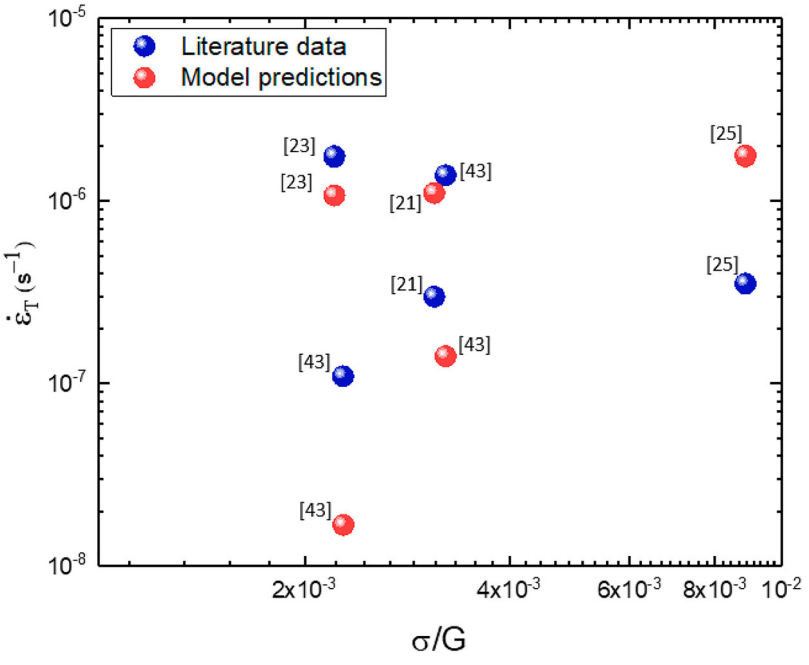

Figure 4. Comparison of creep rates of nc Cu obtained from model against literature data. In this figure, the creep rates obtained from the model employed D_{0b} and Q_{gb} values belonging to nc Cu. The reference number is shown besides the data points in square brackets.

made with D_{ob} and Q_{gb} values belonging to nc Cu, taken from [21] but with D_{oL} and Q_L belonging to conventional polycrystalline copper (taken from [42]). Figure 4 reveals that the calculated strain rates of nc Cu are in better agreement with experimental strain rates observed in nc Cu when the D_{ob} and Q_{gb} values belonging to nc Cu were employed in the model. Please note that D_{oL} and Q_L belonging to conventional polycrystalline copper was used in the model calculations as values of this parameter for nc Cu have not been reported.

Finally, before concluding, we wanted to check if the addition of higher amounts of Zr can enhance the creep resistance of nc Cu. To check the impact of higher solute additions on creep, we evaluated the creep strain rates in nc Cu–5Zr and nc Cu–7Zr bearing grain sizes of 29 and 20 nm respectively. Figure 5 compares the creep strain rates of nc Cu, nc Cu–3Zr, nc Cu–5Zr and nc Cu–7Zr. It is evident from Figure 4 that the creep rates in nc Cu–5Zr and nc Cu–7Zr are higher than that of both nc Cu and nc Cu–3Zr. The addition of higher quantities of Zr is not accompanied by an increase in creep resistance of Cu due apparently to the reduction in equilibrium grain size brought about by higher concentrations of Zr. As mentioned earlier, the grain size and consequently the diffusion path length has a stronger bearing on creep deformation than the reduction in diffusivity brought about by solute segregation.

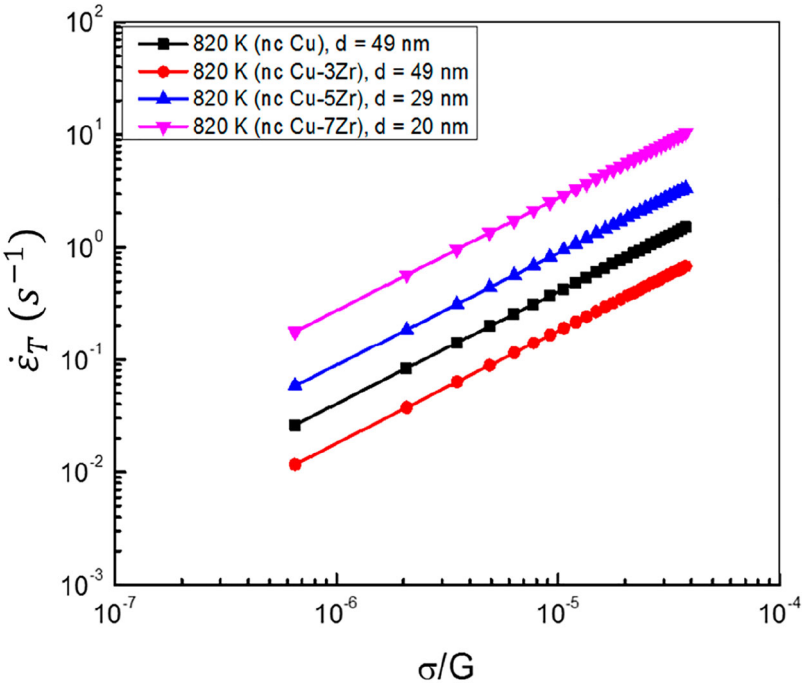

Figure 5. The creep deformation rate of various Cu–Zr alloys as a function of the normalised stress (σ/G).

Before we conclude, we would like to point out that enhancement in creep resistance in alloys vis-à-vis the pure element can be achieved in nc materials if the solute chosen for grain size stabilisation demonstrates a higher bonding with the grain boundary solvent atoms. Furthermore, the solute atom must have a larger atomic size compared to the solvent atom, but the difference in atomic size must encourage grain boundary segregation instead of phase separation. Hence thermodynamic calculations guided by Murdoch and Schuh [4] approach can be employed in conjunction with Hondros and Henderson [11] equation to identify solute atoms capable of enhancing grain size stability and creep resistance at the same time.

4. Conclusion

In this work, we adopted a theoretical approach to investigate the effect of solute segregation on the creep deformation of nanocrystalline copper. Guided by Murdoch and Schuh's thermodynamics model, Zr was found to be a solute capable of stabilising the Cu nanostructure. The segregation of Zr at the grain boundary is found to reduce the grain boundary diffusivity of Cu which leads to higher creep resistance; albeit this is marginal which can be attributed to the lower concentration of Zr additions. Higher Zr concentration does not confer higher creep resistance because the equilibrium grain size is inversely proportional to the solute content.

Disclosure statement

No potential conflict of interest was reported by the author(s).

Data availability statement

The raw/processed data required to reproduce these findings cannot be shared at this time due to technical or time limitations.

ORCID

I. Wani http://orcid.org/0000-0002-3888-2534
N. Rai http://orcid.org/0000-0002-2759-2697

References

[1] B.S. Murty, M.K. Datta, and S.K. Pabi, *Structure and thermal stability of nanocrystalline materials*. Sadhana 28 (2003), pp. 23–45.
[2] C.C. Koch, R.O. Scattergood, K.A. Darling, and J.E. Sermones, *Stabilization of nanocrystalline grain sizes by solute additions*. J. Mater. Sci. 43 (2008), pp. 7264–7272.
[3] N. Rai, B.K. Samantaray, K.V. Rajulapati, R. Ravi, S.R. Bakshi, N.T.B.N. Koundinya, R.S. Kottada, and S. Gollapudi, *Theoretical and experimental studies on thermal stability of nanocrystalline Mg–Mo alloy*. Materialia 14 (2020), pp. 100933.
[4] H.A. Murdoch and C.A. Schuh, *Stability of binary nanocrystalline alloys against grain growth and phase separation*. Acta Mater. 61 (2013), pp. 2121–2132.
[5] K.A. Darling, B.K. VanLeeuwen, J.E. Semones, C.C. Koch, R.O. Scattergood, L.J. Kecskes, and S.N. Mathaudhu, *Stabilized nanocrystalline iron-based alloys: guiding efforts in alloy selection*. Mater. Sci. Eng. A 528 (2011), pp. 4365–4371.
[6] K.A. Darling, B.K. VanLeeuwen, J.E. Semones, C.C. Koch, and R.O. Scattergood, *Thermal stability of nanocrystalline Fe–Zr alloys*. Mater. Sci. Eng. A 527 (2010), pp. 3572–3580.
[7] F. Liu and R. Kirchheim, *Grain boundary saturation and grain growth*. Scr. Mater. 51 (2004), pp. 521–525.
[8] J. Weissmuller, *Alloy effects in nanostructures*. Nanostruct. Mater. 3 (1993), pp. 261–272.
[9] T. Chookajorn, H.A. Murdoch, and C.A. Schuh, *Design of stable nanocrystalline alloys*. Science 337 (2012), pp. 951–954.
[10] K.A. Darling, M. Rajagopalan, M. Komarasamy, M.A. Bhatia, B.C. Hornbuckle, R.S. Mishra, and K.N. Solanki, *Extreme creep resistance in a microstructurally stable nanocrystalline alloy*. Nature 537 (2016), pp. 378–381.
[11] E.D. Hondros and P.J. Henderson, *Role of grain boundary segregation in diffusional creep*. Metall. Trans. 14A (1983), pp. 521–530.
[12] J.E. Bird, A.K. Mukherjee, and J.E. Dorn, *Correlations between high temperature creep behavior and structure*, in *Quantitative Relation Between Properties and Microstructure*, D.G. Brandon and A. Rosen, eds., Israel Universities Press, Haifa, 1969, pp. 1–186.
[13] H.A. Murdoch, Design of a stable nanocrystalline alloy, PhD Thesis, 2013, Massachusetts Institute of Technology.

[14] S. Gollapudi and A.K. Soni, *Understanding the effect of grain size distribution effects on stability of nanocrystalline materials: An analytical approach*. Materialia 9 (2020), pp. 100579.
[15] S. Gollapudi, N. Rai, R. Kushwaha, and R.K. Sabat, *Crystallographic texture influences on the thermal stability of nanocrystalline materials*. J. Mater. Sci. 56 (2021), pp. 11154–11163.
[16] A. Khalajhedayati and T. Rupert, *High-Temperature stability and grain boundary complexion formation in a nanocrystalline Cu–Zr alloy*. JOM 67 (2015), pp. 2788–2801.
[17] J. Deng, D.L. Wang, Q.P. Kong, and J.P. Shui, *Stress dependence of creep in nanocrystalline Ni–P alloy*. Scrip. Metall. Mater. 32 (1995), pp. 349–352.
[18] N. Wang, Z. Wang, K.T. Aust, and U. Erb, *Room temperature creep behavior of nanocrystalline nickel produced by an electrodeposition technique*. Mater. Sci. Eng. A 237 (1997), pp. 150–158.
[19] Q.P. Kong, B. Cai, and M.L. Xiao, *High temperature creep of two nanocrystalline alloys*. Mater. Sci. Eng., A 234 (1997), pp. 91–93.
[20] F. G-Mora, A. D-Rodrıguez, M. J-Melendo, R. Chaim, and M. Hefetz, *Creep of nanocrystalline Y-SZP ceramics*. Nanostruct. Mater. 11 (1999), pp. 531–537.
[21] B. Cai, Q.P. Kong, L. Lu, and K. Lu, *Low temperature creep of nanocrystalline pure copper*. Mater. Sci. Eng., A 286 (2000), pp. 188–192.
[22] W.M. Yin, S.H. Whang, R. Mirshams, and C.H. Xiao, *An investigation for fracture toughness and creep behavior in carbon doped nanocrystalline nickel*. Mater. Sci. Eng. A 301 (2001), pp. 18–22.
[23] Z. Jiang, X. Liu, G. Li, Q. Jiang, and J. Lian, *Strain rate sensitivity of a nanocrystalline copper synthesized by electric brush plating*. Appl. Phys. Lett 88 (2006), pp. 143115.
[24] S. Ghosh and A.H. Chokshi, *Creep in nanocrystalline zirconia*. Scr. Mater. 86 (2014), pp. 13–16.
[25] N. Ghazi and J.W. Kysar, *Experimental investigation of plastic strain recovery and creep in nanocrystalline copper thin films*. Exp. Mech. 56 (2016), pp. 1351–1362.
[26] D.-H. Lee, M.-Y. Seok, Y. Zhao, I.-C. Choi, J. He, Z. Lu, J.-Y. Suh, U. Ramamurty, M. Kawasaki, T.G. Langdon, and J.-i. Jang, *Spherical nanoindentation creep behavior of nanocrystalline and coarse grained CoCrFeMnNi high entropy alloys*. Acta Mater. 109 (2016), pp. 314–322.
[27] T.G. Desai, P.C. Millett, and D. Wolf, *Molecular dynamics study of diffusional creep in nanocrystalline UO2*. Acta Mater. 56 (2008), pp. 4489–4497.
[28] Y.J. Wang, A. Ishii, and S. Ogata, *Grain size dependence of creep in nanocrystalline copper by molecular dynamics*. Mater. Trans. 53 (2012), pp. 156–160.
[29] K. Nie, W.-P. Wu, X.-L. Zhang, and S.-M. Yang, *Molecular dynamics study on the grain size, temperature, and stress dependence of creep behavior in nanocrystalline nickel*. J Mater Sci 52 (2017), pp. 2180–2191.
[30] S. Saha and M. Motalab, *Nature of creep deformation in nanocrystalline tungsten*. Comput. Mater. Sci. 149 (2018), pp. 360–372.
[31] F. Zhao, J. Zhang, C. He, Y. Zhang, X. Gao, and L. Xie, *Molecular dynamics simulation on creep behavior of nanocrystalline TiAl alloy*. Nanomaterials 10 (2020), pp. 1693–1699.
[32] H. Yao, T. Ye, W. Yu, P. Wang, J. Wu, Y. Wu, and P. Chen, *Atomic scale investigation of creep behavior and deformation mechanism in nanocrystalline FeCrAl alloys*. Mater. Des. 206 (2021), pp. 109766.
[33] A.H. Chokshi, A. Rosen, J. Karch, and H. Gleiter, *On the validity of the Hall–Petch relationship in nanocrystalline materials*. Scripta Metall. Mater. 23 (1989), pp. 1679–1684.

[34] K. Zhang and J.R. Weertman, *The influence of time, temperature and grain size on indentation creep in high purity nanocrystalline and ultrafine grain copper*. Appl. Phys. Lett. 85 (2004), pp. 5197–5199.
[35] R.S. Kottada and A.H. Chokshi, *Low temperature compressive creep in electrodeposited nanocrystalline nickel*. Scr. Mater. 53 (2005), pp. 887–892.
[36] S. Gollapudi, K.V. Rajulapati, I. Charit, C.C. Koch, R.O. Scattergood, and K.L. Murty, *Creep in nanocrystalline materials: role of stress assisted grain growth*. Mater. Sci. Eng., A 527 (2010), pp. 5773–5781.
[37] D.S. Gianola, S.V. Petegem, M. Legros, S. Brandstetter, H. Van Swygenhoven, and K.J. Hemker, *Stress assisted discontinuous grain growth and its effect on the deformation behavior of nanocrystalline aluminium thin films*. Acta Mater. 54 (2006), pp. 2253–2263.
[38] M. Chauhan and F.A. Mohamed, *Interpretation of the creep behavior of nanocrystalline Ni in terms of dislocation accommodated boundary sliding*. Metall. Mater. Trans. A 37 (2006), pp. 3555–3567.
[39] F.A. Mohamed, *Interpretation of superelastic flow in terms of threshold stress*. J. Mater. Sci. 18 (1983), pp. 582–592.
[40] M.F. Ashby, *Boundary defects and atomistic aspects of boundary sliding and diffusional creep*. Surf. Sci. 31 (1972), pp. 498–542.
[41] N.F. Fiore and C.L. Bauer, *Solute atom dislocation binding energy in dilute Cu–Ge alloys*. Acta Metall. 12 (1964), pp. 1329–1336.
[42] H.J. Frost and M.F. Ashby, *Deformation Mechanism Maps: The Plasticity and Creep of Metals and Ceramics*, Pergamon Press, Oxford, UK, 1982.

Philosophical Magazine

ISSN: 1478-6435 (Print) 1478-6443 (Online) Journal homepage: www.tandfonline.com/journals/tphm20

Blocking temperature variations in graphene nanostructures with distinct edge geometries: a Monte Carlo simulation study

Z. Fadil, Chaitany Jayprakash Raorane, Hussein Sabbah, A. Samih, E. Salmani, Khaled H. Mahmoud, Abdulrahman A. Alsayyari & Seong-Cheol Kim

To cite this article: Z. Fadil, Chaitany Jayprakash Raorane, Hussein Sabbah, A. Samih, E. Salmani, Khaled H. Mahmoud, Abdulrahman A. Alsayyari & Seong-Cheol Kim (2026) Blocking temperature variations in graphene nanostructures with distinct edge geometries: a Monte Carlo simulation study, Philosophical Magazine, 106:5, 451-466, DOI: 10.1080/14786435.2025.2573174

To link to this article: https://doi.org/10.1080/14786435.2025.2573174

PHILOSOPHICAL MAGAZINE
2026, VOL. 106, NO. 5, 451–466
https://doi.org/10.1080/14786435.2025.2573174

Taylor & Francis
Taylor & Francis Group

Blocking temperature variations in graphene nanostructures with distinct edge geometries: a Monte Carlo simulation study

Z. Fadil[a]*, Chaitany Jayprakash Raorane[b]*, Hussein Sabbah[c], A. Samih[a], E. Salmani[a], Khaled H. Mahmoud[d], Abdulrahman A. Alsayyari[e] and Seong-Cheol Kim[b]

[a]Laboratoire de Matière Condensée et Sciences Interdisciplinaires (LaMCScI), URL-CNRST, Faculty of Sciences, Mohammed V University in Rabat, Rabat, Morocco; [b]School of Chemical Engineering, Yeungnam University, Gyeongsan, Republic of Korea; [c]College of Engineering and Technology, American University of the Middle East, Egaila, Kuwait; [d]Department of Physics, College of Khurma University College, Taif University, Taif, Saudi Arabia; [e]Department of Radiologic Technology, College of Applied Medical Sciences, Qassim University, Buraydah, Saudi Arabia

ABSTRACT

We employed Monte Carlo simulations based on the Blume-Emery-Griffiths model to investigate the magnetic behaviour and blocking temperature (T_B) of graphene nanostructures featuring different edge geometries. Our results demonstrate that T_B increases with stronger bilinear (J) and especially biquadratic (K) exchange interactions, as well as with an applied external magnetic field, while it decreases as the crystal field strength rises. The pronounced influence of K highlights its dominant role in shaping the magnetic dynamics of the system. Among the studied geometries, the armchair nanostructure shows the greatest sensitivity to parameter variations and achieves the highest T_B. These findings underscore the combined importance of exchange interactions and edge geometry in tuning graphene's magnetic properties, offering promising prospects for spintronic devices and data storage technologies.

ARTICLE HISTORY
Received 29 August 2025
Accepted 6 October 2025

KEYWORDS
Monte-Carlo; phase transitions; magnetic effects; magnetic phase transition

1. Introduction

Carbon is among the most abundant and chemically versatile elements in the universe. Its ability to form multiple allotropes, which are distinct structural forms arising from various configurations of carbon atoms, results in a wide range of compounds exhibiting diverse physical and chemical properties. Within this category, carbon-based nanomaterials (CNMs) include numerous nanostructures such as graphene [1,2], carbon nanotubes (CNTs) [3], fullerenes C_{60} [4], graphite [5], and carbon dots [6]. The isolation of graphene, a two-dimensional (2D) material [7,8], in 2004 marked a groundbreaking advancement in the field. Graphene [1,2] is a prototypical 2D nanostructure composed of carbon atoms

CONTACT Z. Fadil fadilzakaria604@gmail.com Laboratoire de Matière Condensée et Sciences Interdisciplinaires (LaMCScI), URL-CNRST, Faculty of Sciences, Mohammed V University in Rabat, P.O. Box 1014, Rabat, Morocco; Seong-Cheol Kim sckim07@ynu.ac.kr School of Chemical Engineering, Yeungnam University, Gyeongsan 38541, Republic of Korea
*Authors contributed equally.

arranged in a hexagonal honeycomb lattice. Its remarkable electrical conductivity, characterised by exceptionally high electron mobility [9], has attracted significant attention for potential applications in optoelectronics [10] and sensing [11] technologies. Beyond its electronic advantages, graphene also exhibits outstanding mechanical strength and stability [12,13], making it a promising candidate for structural reinforcement in aerospace composites [14] and the automotive industry [15]. The multifunctionality of graphene is further demonstrated through applications in energy storage [16] and biomedical fields [17].

This paper focuses on the magnetic behaviour and blocking temperature (T_B) associated with different graphene edge configurations, specifically zigzag, armchair, and reconstructed zigzag (reczag) edges. The blocking temperature T_B indicates the transition from ferromagnetic or ferrimagnetic states to the superparamagnetic state [18,19]. When graphene honeycomb lattices are cut along various orientations, the resulting edge morphology typically appears as either zigzag or armchair [20]. It has been established that armchair edges are more stable compared to zigzag edges [20–22]. However, density functional theory (DFT) predicts that zigzag edges can reconstruct into a more stable form known as reczag edges [20–22], characterised by alternating five- and seven-membered carbon rings. Both theoretical and experimental studies have confirmed that reczag edges are more stable than armchair and conventional zigzag edges [20,22].

DFT calculations have been instrumental in revealing the diverse electronic and magnetic properties associated with these edge structures. For example, functionalisation of zigzag graphene nanoribbons (ZGNRs) with carboxyl and hydroxyl groups induces spin splitting and reduces band gaps, significantly altering their electronic behaviour [23]. Further DFT analyses show that ZGNRs exhibit metallic characteristics, whereas armchair graphene nanoribbons (AGNRs) behave as semiconductors [24]. Additionally, theoretical studies on armchair (7,7) carbon nanotubes (CNTs) suggest metallic behaviour and confirm the covalent nature of carbon–carbon bonds in this configuration [25].

Monte Carlo methods complement these findings by exploring magnetic behaviour at graphene edges. These simulations demonstrate that the magnetic phase diagram of armchair edges is sensitive to exchange interactions, external magnetic fields, and crystal field effects [26]. Zigzag graphene nanoribbons display complex magnetisation plateau behaviour under longitudinal magnetic fields at low temperatures [27].

In this study, we aim to investigate the magnetic properties and blocking temperature (T_B) of graphene nanostructures with different edge geometries using Monte Carlo simulations [28–30] based on the Metropolis algorithm [31] and the Blume-Emery-Griffiths (BEG) model [32]. The BEG model extends the Ising framework to study complex magnetic and phase transition phenomena, particularly in systems with three possible spin states : S_i equal to –1, 0, or +1. It incorporates bilinear (J) and biquadratic (K) exchange interactions, single-ion anisotropy (D), and external magnetic field (H), enabling simulations of ferromagnetic, paramagnetic, and quadrupolar phases [33,34]. Widely used in Monte Carlo simulations, the BEG model captures temperature-dependent phase behaviour, hysteresis, and magnetic ordering, especially in low-dimensional or edge-sensitive materials. It effectively describes the interplay between spin alignment, vacancies, and anisotropic effects, providing a robust framework for investigating critical phenomena and magnetic topologies in nanoscale systems [35–38].

Moreover, pioneering studies on the Blume-Emery-Griffiths (BEG) model provide a fundamental framework for understanding the struggle between biquadratic and bilinear

interactions in the formation of complex phase diagrams. Dynamic phase transitions have been studied using various methods, including effective field theory, route probability method, and mean field theory with Glauber dynamics. These methods have revealed various behaviours, such as tricritical points, mixed phases, and hysteresis events [39–43.] The spin-2 Ising model with biquadratic coupling [44], spin-1 Blume–Capel films with variable crystal fields [45–48], dilute magnetic semiconductors [49], the effects of quantum anisotropy and RKKY interactions [50–52], and Monte Carlo studies of biquadratic exchange anisotropy and BEG thin films [53–55] are some examples of related models that have already investigated phase transitions and diagrams. With Monte Carlo studies of magnetisation plateaus, dielectric characteristics, and compensation behaviours in graphyne, coronene, naphthalene, hexacene, rubrene, core–shell nanotubes, and borophene layers with RKKY interactions, this research has recently been extended to carbon-based and related nanostructures [56–65]

The novelty of this work lies in examining how edge structures such as zigzag, armchair, and reczag influence T_B and other magnetic characteristics, advancing the understanding of edge geometry's role in tuning graphene's magnetic behaviour. The motivation is to enhance knowledge of graphene-based materials for potential applications in spintronics, data storage, and sensors, where precise control of magnetic properties is crucial.

This paper is organised as follows: Section 2 details the methods, Section 3 presents the results, and Section 4 concludes the study.

2. Model and method

To assess and compare the magnetic characteristics, especially the blocking temperature (T_B), of graphene nanostructures (zigzag, armchair, reczag) each containing 36 atoms ($N_T = 36$), we conducted Monte Carlo simulations using the Metropolis algorithm within the Blume-Emery-Griffiths model [32]. Carbon atoms were replaced with spin-1 analogs, and for thermal stabilisation, the first 2.10^5 steps per spin of the total 2.10^6 were excluded (Figure 1). The ergodicity of the system has been verified by checking the convergence of energy and magnetisation, ensuring that the time averages reliably reflect the ensemble averages. To isolate the impact of edge geometry (zigzag, armchair, and reczag) on magnetic characteristics, including the blocking temperature (T_B), and to capture finite size effects, the system size is purposely limited to $N_T = 36$ atoms. To determine the relative stability hierarchy of edge configurations, this study focuses on tiny systems rather than extrapolating absolute T_B values to bulk nanomaterials. The results support the idea that thermal stability is dominated by local topology, particularly the armchair edge, which guides the creation of optimal nanodevices.

Magnetic properties of the graphene nanostructures are described by the following Hamiltonian:

$$H = -J \sum_{\langle i,j \rangle} S_i S_j - K \sum_{\langle i,j \rangle} (S_i S_j)^2 - H \sum_i S_i - D \sum_i (S_i)^2, \tag{1}$$

In all three nanostructures, magnetic interactions are governed by bilinear (J) and biquadratic (K) exchange couplings, summed over nearest-neighbor pairs $\langle i, j \rangle$.

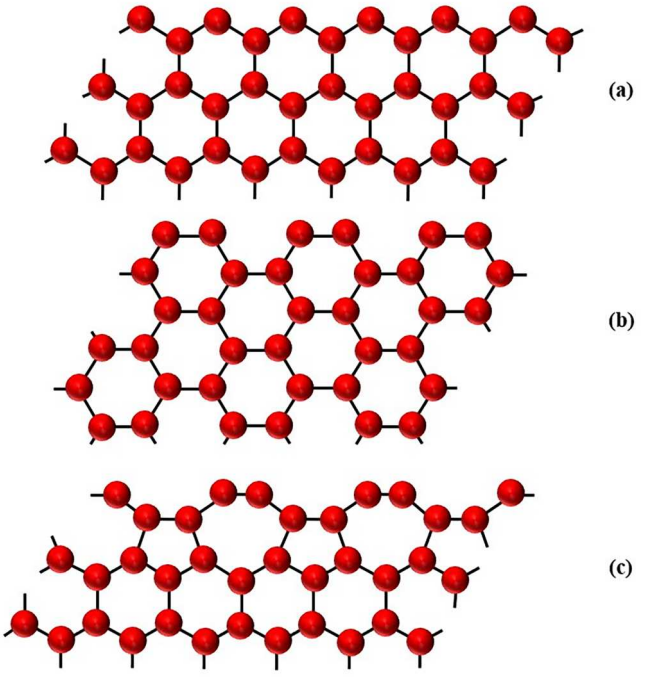

Figure 1. Graphene nanostructures with zigzag (a), armchair (b), and reczag (c) edges are composed of atoms, each assigned a spin value of 1.

Additionally, the system experiences the influence of a crystal field (D) and an external magnetic field (H).

- Bilinear exchange interaction $-J \sum_{\langle i,j \rangle} S_i S_j$: This term models the nearest-neighbor interaction between spins Si and Sj, with the sign of J determining whether the coupling is ferromagnetic ($J > 0$) or antiferromagnetic ($J < 0$).
- Biquadratic interaction $- K \sum_{\langle i,j \rangle} (S_i S_j)^2$: This higher-order interaction captures more complex spin correlations and contributes to phenomena such as magnetic frustration or first-order transitions.
- Zeeman term $-H \sum_i S_i$: Represents the interaction between the spin system and an external magnetic field H, which can align or oppose the spin orientations depending on the field direction.
- Single-ion anisotropy term $-D \sum_i (S_i)^2$: This is the defining feature of the Blume-Capel model. It introduces a crystal field effect that controls the population of spin states. For instance, a large positive D favours the non-magnetic $S = 0$ state in spin-1 systems, while negative D promotes magnetic states ($S = \pm 1$).

The expressions for site energy (Equation 2), magnetisation (Equation 3), and susceptibility (Equation 4) in graphene nanostructures are presented below:

$$E = \frac{1}{N_{\mathrm{T}}}\mathcal{H}\,, \tag{2}$$

$$M = \frac{1}{N_{\mathrm{T}}}\sum_i S_i \tag{3}$$

$$\chi = \beta\left(\left\langle M^2\right\rangle - < M >^2\right) \tag{4}$$

Using $\beta = 1/\ k_B T$ and setting $k_B = 1$ simplifies the energy expression to $E = T$. The exchange constant J is varied to examine its effect on magnetic responses. For comparison and coherence, all parameters are normalised and reported in dimensionless units.

Our simulations use dimensionless units normalised by the exchange interaction J and k_B to express energy. A typical $J \approx 5$ meV corresponds to $T = 1$ unit ≈ 58 K, suggesting that the simulated range $T \approx 1$–7 extends from 58 to 406 K for comparison with real graphene-based magnetic nanomaterials. Parameters $J, K, D = 1$–3 thus represent 5–15 meV, while $H = 1$ corresponds to magnetic fields of several tens of Teslas. Although approximate, this scaling places our results on T_B in experimentally relevant regimes for spintronic applications.

3. Simulated results using Monte Carlo methods

This section utilises Monte Carlo simulations to investigate the magnetic behaviour of graphene nanostructures, focusing on three edge configurations: zigzag, armchair, and reczag. Particular attention is given to the blocking temperature (T_B) and its dependence on the bilinear (J) and biquadratic (K) exchange couplings, the external magnetic field (H), and the crystal field (D). Moreover, the transition to the superparamagnetic state is characterised by the blocking temperature (T_B), specific to finite magnetic nanosystems. It represents the thermal stability of the system and corresponds to the maximum of the magnetic susceptibility (χ vs. T). The magnetisation remains 'blocked' below T_B, while thermal fluctuations cause a rapid reversal of the net magnetic moment above it. The most relevant measure in this case is T_B, as it accurately reflects the thermal stability and information retention of the studied graphene nanostructures, unlike the critical temperature (T_C), which characterises a phase change in infinite systems.

Figure 2 presents the temperature dependence of magnetisation (a) and magnetic susceptibility (b) for the three configurations, using fixed parameters: $J = 1$, $K = 1$, $D = -1$, and $H = 1$. As temperature increases, magnetisation decreases, indicating a transition from the ferromagnetic to the superparamagnetic phase. The results highlight a distinct behaviour in the armchair nanostructure compared to the zigzag and reczag configurations, which exhibit similar trends. The blocking temperature, identified by the peak in the susceptibility curve, serves as a key indicator of this phase transition. Despite having the same number of atoms and spins, the armchair configuration exhibits a higher T_B, attributed to its unique edge geometry.

Figure 3 presents the magnetisation (M) and susceptibility (χ) of graphene nanostructures with zigzag (a, b), armchair (c, d), and reczag (e, f) edge geometries for varying values of the bilinear exchange coupling J, while keeping $K = 1$, $D = -1$, and $H = 1$

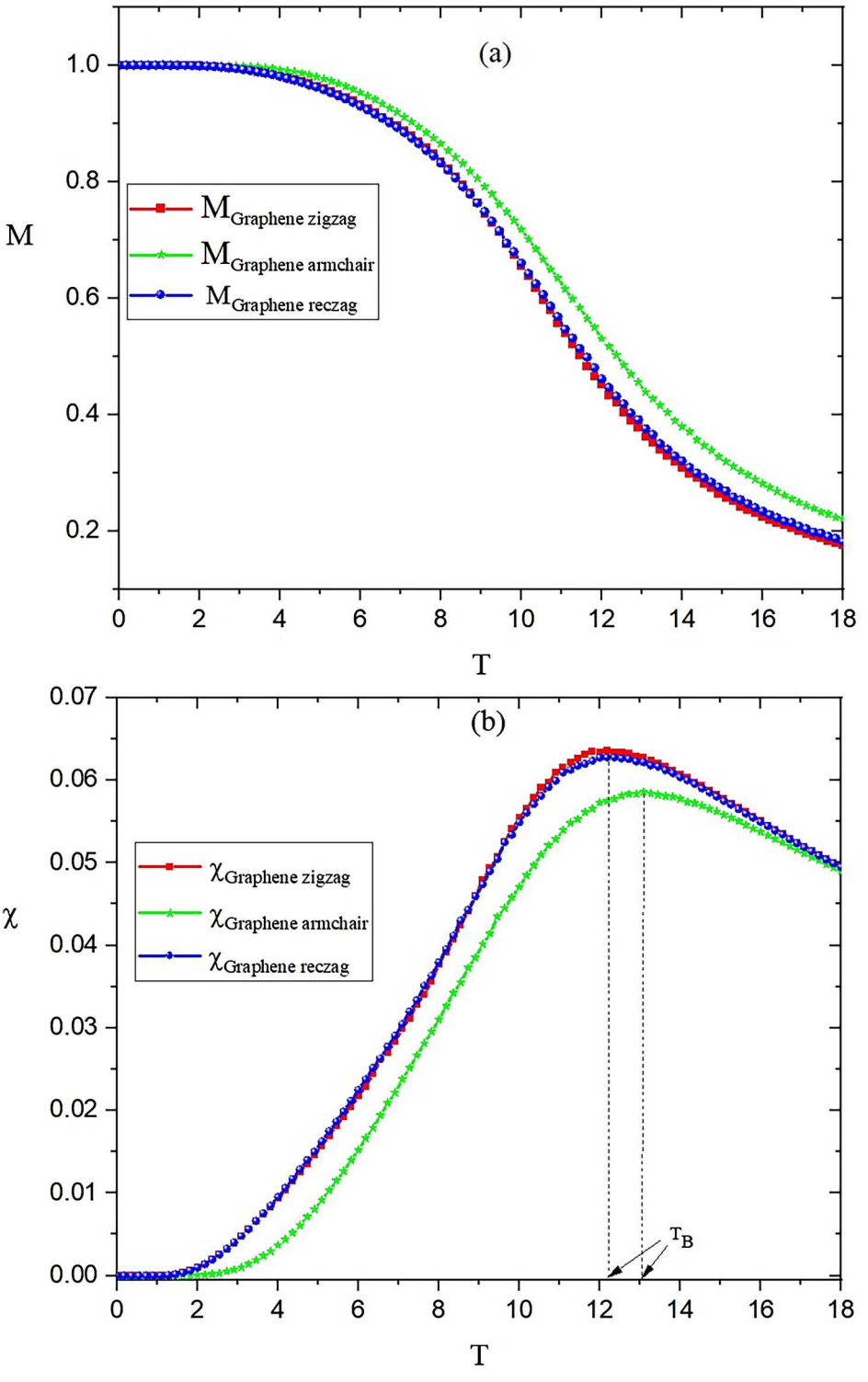

Figure 2. Magnetisation (M) in (a) and susceptibility (χ) in (b) vs. temperature for graphene zigzag, armchair, and reczag nanostructures, with $J = 1$, $K = 1$, $D = -1$, and $H = 1$.

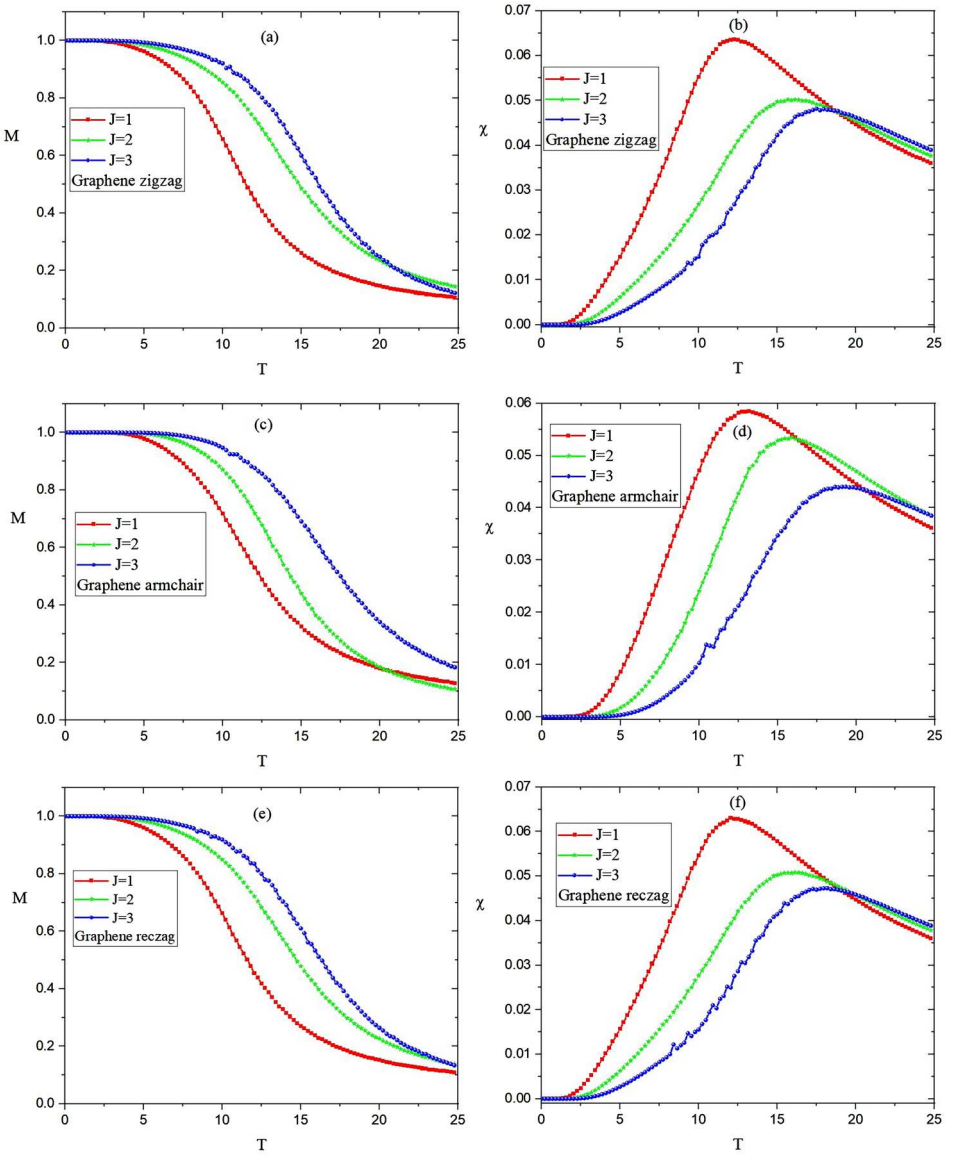

Figure 3. Magnetisation and susceptibility of graphene zigzag (a, b), armchair (c, d), and reczag (e, f) nanostructures are presented for varying J, while keeping $K = 1$, $D = -1$, and $H = 1$ fixed.

constant. For all three configurations, increasing J from 1 to 3 enhances the system's magnetic stability. A stronger bilinear exchange coupling reinforces spin interactions, thereby requiring more thermal energy to disrupt the magnetic order. This results in a delayed transition to the superparamagnetic phase, as evidenced by the shift of susceptibility peaks toward higher temperatures.

Figure 4 illustrates the temperature-dependent magnetisation and susceptibility for graphene nanostructures with zigzag (a, b), armchair (c, d), and reczag (e, f) edge configurations under varying values of the biquadratic exchange coupling K, while

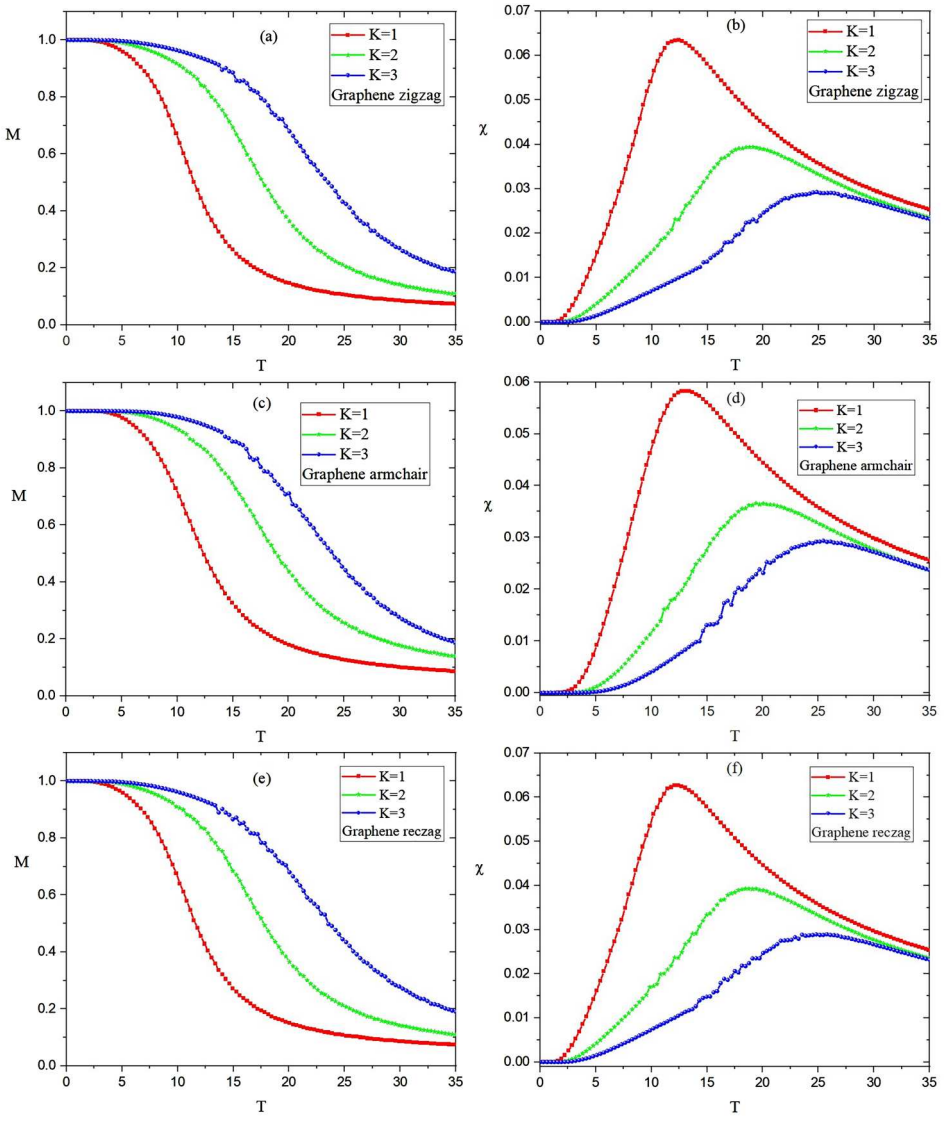

Figure 4. Magnetisation and susceptibility of graphene zigzag (a, b), armchair (c, d), and reczag (e, f) nanostructures are presented for varying K, while keeping $J = 1$, $D = -1$, and $H = 1$ fixed.

keeping $J = 1$, $D = -1$, and $H = 1$ constant. An increase in K results in a noticeable rise in the blocking temperature (T_B) across all geometries. This behaviour is attributed to enhanced spin–spin interactions, which require greater thermal energy to disrupt the magnetically ordered state. Consequently, magnetisation persists at higher temperatures, and the transition to the superparamagnetic regime is delayed, as indicated by the shift of susceptibility peaks toward higher temperatures. The shift in susceptibility peak position with increasing K is attributed to the increased spin-spin interactions introduced by the nonlinear term. As K increases, the energy barrier for spin reorientation becomes higher, requiring more thermal energy for the system to change from an ordered to a disordered

magnetic state. This leads to an increase in T_B, which is reflected in the rightward shift of the susceptibility peak. Notably, the effect of K on T_B is more pronounced than that of J, underscoring the dominant role of non-linear spin interactions in shaping the magnetic dynamics of the system.

Figure 5 presents the magnetisation and susceptibility curves for graphene nanostructures with zigzag (a, b), armchair (c, d), and reczag (e, f) edge geometries under varying external magnetic field strengths H, while keeping $J = 1$, $D = -1$, and $K = 1$ constant. As H increases, the blocking temperature (T_B) rises across all configurations. This behaviour is attributed to enhanced spin alignment promoted by the external magnetic field, which

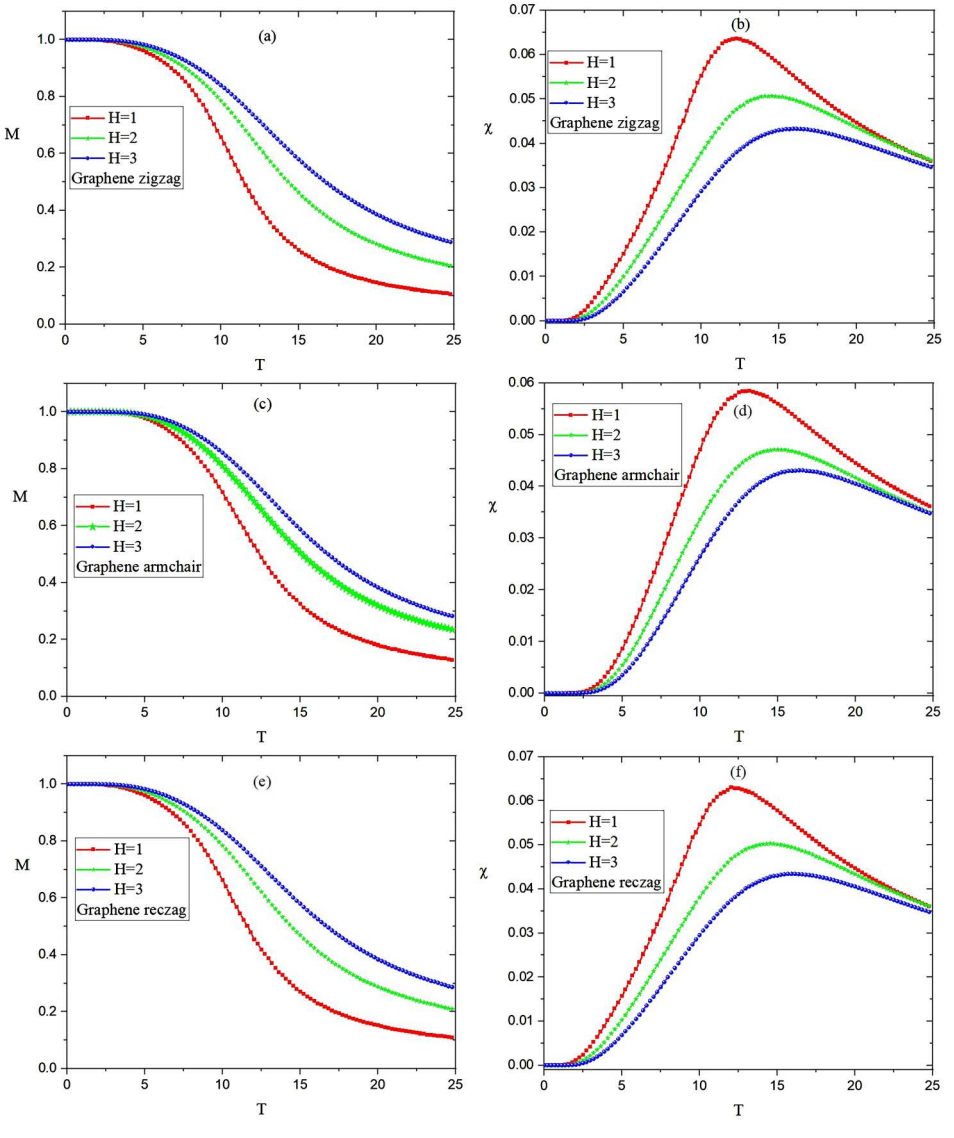

Figure 5. Magnetisation and susceptibility of graphene zigzag (a, b), armchair (c, d), and reczag (e, f) nanostructures are presented for varying H, while keeping $J = 1$, $D = -1$, and $K = 1$ fixed.

strengthens magnetic order and resists thermal fluctuations. As a result, greater thermal energy is required to disrupt the magnetisation, delaying the onset of the superparamagnetic phase. This is evidenced by the shift of susceptibility peaks toward higher temperatures.

Figure 6 displays the magnetisation and susceptibility curves for graphene nanostructures with zigzag (a, b), armchair (c, d), and reczag (e, f) edge geometries under varying crystal field values (D), while keeping $J = 1$, $H = 1$, and $K = 1$ constant. As D decreases, the blocking temperature (T_B) declines across all configurations, indicating a reduction in magnetic stability. At $D = -7$, the magnetisation drops to zero, suggesting the occurrence

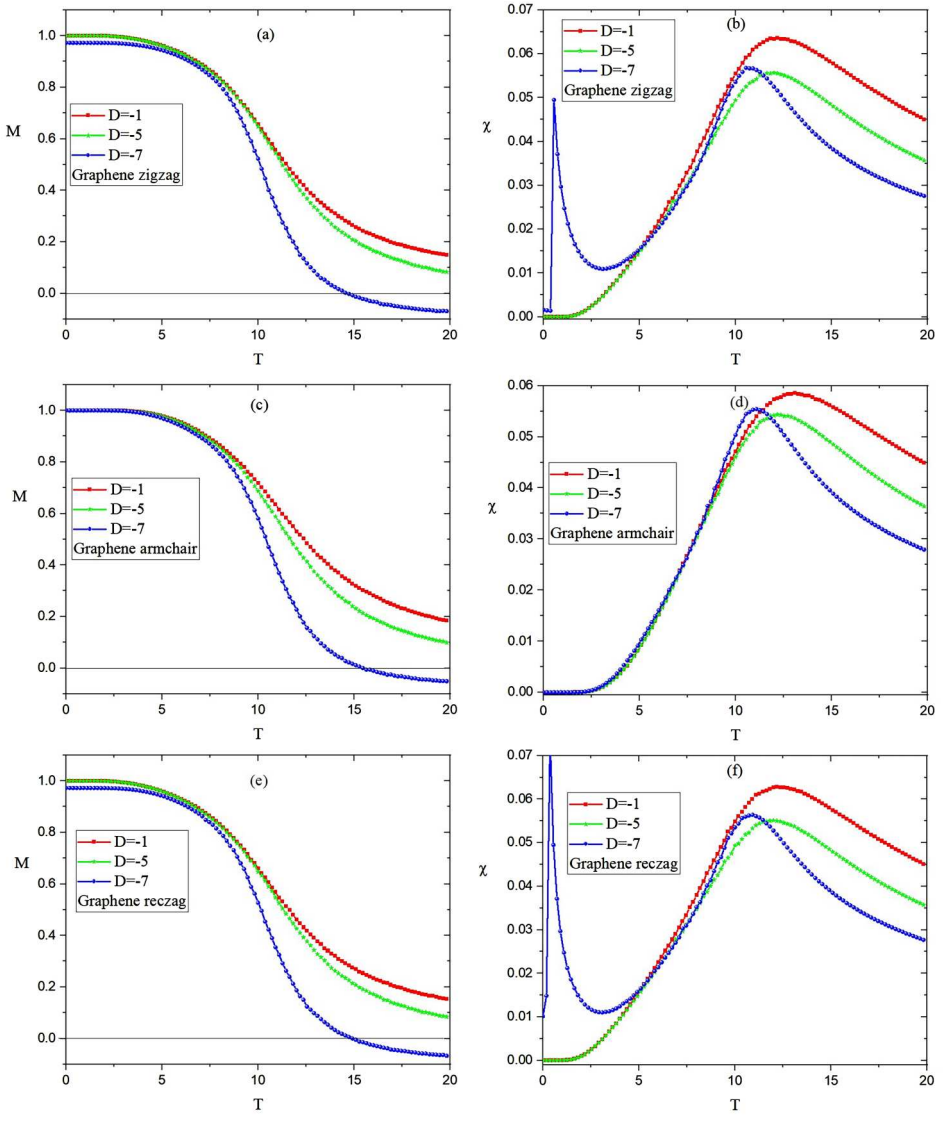

Figure 6. Magnetisation and susceptibility of graphene zigzag (a, b), armchair (c, d), and reczag (e, f) nanostructures are presented for varying D, while keeping $J = 1$, H = 1, and $K = 1$ fixed.

of a compensation temperature, where opposing sublattice magnetisations cancel each other. The first susceptibility peaks observed in panels (b) and (f) arise from the fact that the system does not begin in a fully ordered magnetic state. This partial ordering at low temperatures leads to an initial magnetic response to thermal excitations, reflected in the early susceptibility peak. The second peaks in panels (b) and (f), as well as the peak in (d), correspond to the blocking temperature and signify the transition from the ferromagnetic to the superparamagnetic phase.

In Figure 7, the blocking temperature (T_B) of graphene nanostructures with zigzag, armchair, and reczag edge geometries is plotted as a function of (a) bilinear exchange coupling (J), (b) biquadratic exchange coupling (K), (c) external magnetic field (H), and (d) crystal field (D), with the remaining parameters held constant. For all three configurations, T_B exhibits an approximately linear increase with increasing J, K, and H. This trend reflects the enhanced spin–spin interactions and the stabilisation of magnetic order, which require higher thermal energy to disrupt and drive the transition to the superparamagnetic phase. In contrast, increasing the magnitude of the crystal field reduces T_B, as it promotes spin localisation and weakens thermal stability. Among the nanostructures examined, the armchair configuration demonstrates the highest sensitivity to variations in physical parameters, while the zigzag and reczag structures show

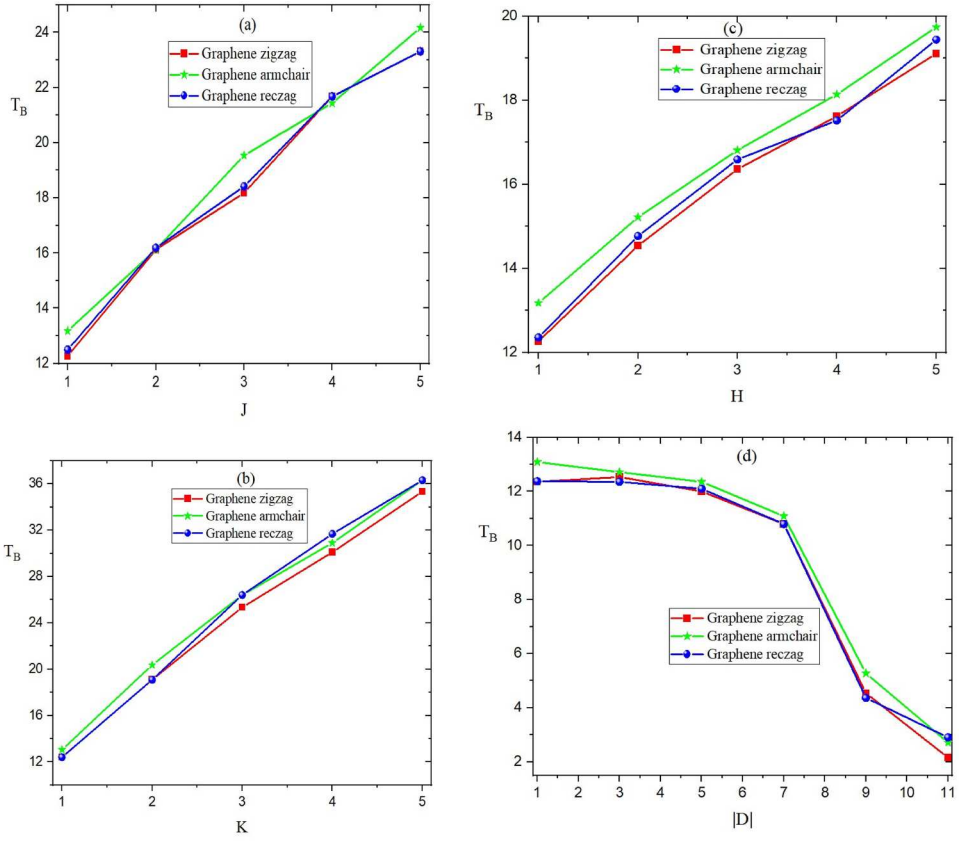

Figure 7. Blocking temperature (T_B) of graphene zigzag, armchair, and reczag nanostructures is plotted, varying with (a) J, (b) K, (c) H, and (d) D, keeping other parameters fixed.

similar but less pronounced responses. Moreover, to describe the variation in blocking temperature as a function of key physical parameters, second-order polynomial fits $y = \text{Intercept} + B_1 x + B_2 x^2$ were applied. For the exchange coupling J, fits to zigzag, armchair, and reczag graphene nanostructures yielded high accuracy ($R^2 \approx 0.99$) with reduced Chi-square values below 0.62, confirming a strong nonlinear dependence of T_B on J. Regarding the biquadratic exchange K, all fits showed excellent agreement ($R^2 > 0.998$), with one case reaching a perfect match ($R^2 = 1$, reduced Chi-square ≈ 0), underlining the dominant role of K. Similarly, for the magnetic field H, the nonlinear decrease of T_B was confirmed with R^2 values ranging from 0.989 to 0.998 and reduced Chi-square values remaining below 0.58. Finally, fitting T_B as a function of crystal field $|D|$ resulted in R^2 values between 0.93 and 0.96 and reduced Chi-square values under 6.5, confirming the weakening of magnetic stability as $|D|$ increases. This distinction highlights the significant role of geometrical configuration in regulating magnetic behaviour and thermal stability.

4. Conclusions

In this work, we employed Monte Carlo simulations within the Blume-Emery-Griffiths framework to investigate the magnetic behaviour and blocking temperature (T_B) of graphene nanostructures with zigzag, armchair, and reczag edge configurations. The results clearly demonstrate that $T_B$increases with stronger bilinear (J) and biquadratic (K) couplings, as well as with higher magnetic field strengths (H), due to enhanced spin coupling and thermal stability. In contrast, increasing the magnitude of the crystal field ($|D|$) leads to a decrease in T_B, reflecting suppressed magnetic order. Notably, a compensation point appears at large negative D, where opposing spin contributions cancel out the total magnetisation. Among the structures studied, the armchair geometry exhibited the highest T_B and the most pronounced response to interaction parameters, emphasising the critical role of edge geometry. These findings justify the relevance of controlling edge shape and physical parameters to tailor the magnetic properties of graphene-based nanosystems. The tunable magnetic response and blocking temperatures make these nanostructures promising candidates for spintronic applications, magnetic sensors, and high-density data storage devices.

Acknowledgements

The authors extend their appreciation to Taif University, Saudi Arabia, for supporting this work through project number (TU-DSPP-2024 -51).

Disclosure statement

No potential conflict of interest was reported by the author(s).

Funding

This research was funded by Taif University, Saudi Arabia, Project No. (TU-DSPP-2024-51). Also, this research was supported by the National Research Foundation of Korea (NRF) grant funded by the Korea government (MSIT) (RS-2025-22222973).

Data availability statement

All data that support the findings of this study are included within the article.

References

[1] K.S. Novoselov, A.K. Geim, S.V. Morozov, D.E. Jiang, Y. Zhang, S.V. Dubonos and A.A. Firsov, *Electric field effect in atomically thin carbon films*. Science 306(5696) (2004), pp. 666–669.

[2] A.K. Geim, *Graphene: status and prospects*. Science 324(5934) (2009), pp. 1530–1534.

[3] P.J. Harris, *Carbon nanotube composites*. Int. Mater. Rev. 49(1) (2004), pp. 31–43.

[4] R.S. Ruoff, D.S. Tse, R. Malhotra and D.C. Lorents, *Solubility of fullerene (C60) in a variety of solvents*. J. Phys. Chem. 97(13) (1993), pp. 3379–3383.

[5] D.D.L. Chung, *Review graphite*. J. Mater. Sci. 37 (2002), pp. 1475–1489.

[6] M. Tuerhong, X.U. Yang and Y.I.N. Xue-Bo, *Review on carbon dots and their applications*. Chin. J. Anal. Chem. 45(1) (2017), pp. 139–150.

[7] B. Luo, G. Liu and L. Wang, *Recent advances in 2D materials for photocatalysis*. Nanoscale 8(13) (2016), pp. 6904–6920.

[8] R. Mas-Balleste, C. Gomez-Navarro, J. Gomez-Herrero and F. Zamora, *2D materials: to graphene and beyond*. Nanoscale 3(1) (2011), pp. 20–30.

[9] K.I. Bolotin, K.J. Sikes, Z. Jiang, M. Klima, G. Fudenberg, J. Hone and H.L. Stormer, *Ultrahigh electron mobility in suspended graphene*. Solid State Commun. 146(9-10) (2008), pp. 351–355.

[10] J. Wu, H. Lin, D.J. Moss, K.P. Loh and B. Jia, *Graphene oxide for photonics, electronics and optoelectronics*. Nat. Rev. Chem. 7(3) (2023), pp. 162–183.

[11] J. Liu, S. Bao and X. Wang, *Applications of graphene-based materials in sensors: a review*. Micromachines 13(2) (2022), pp. 184.

[12] A.E. Galashev and O.R. Rakhmanova, *Mechanical and thermal stability of graphene and graphene-based materials*. Phys. Uspekhi 57(10) (2014), pp. 970–989.

[13] C.H. Tay and M. Norkhairunnisa, *Mechanical strength of graphene reinforced geopolymer nanocomposites: a review*. Front. Mater. 8 (2021), pp. 661013.

[14] S.M.A. Aftab, R.B. Shaikh, B. Saifullah, M.Z. Hussein and K.A. Ahmed. Aerospace applications of graphene nanomaterials. In AIP conference proceedings (Vol. 2083, No. 1). AIP Publishing, 2019, March.

[15] A. Elmarakbi and W. Azoti. State of the art on graphene lightweighting nanocomposites for automotive applications. Experimental Characterization, Predictive Mechanical and Thermal Modeling of Nanostructures and their Polymer Composites, 1-23, 2018.

[16] A.G. Olabi, M.A. Abdelkareem, T. Wilberforce and E.T. Sayed, *Application of graphene in energy storage device–A review*. Renew. Sustain. Energy Rev. 135 (2021), pp. 110026.

[17] A. Kumar and C.H. Lee. Synthesis and biomedical applications of graphene: present and future trends. Advances in graphene science, 5772–5578, 2013.

[18] Z. Fadil, C.J. Raorane, H. Sabbah, R. El Fdil, A.A. Ifseisi, R. Boopathiraja and S.C. Kim, *Monte Carlo exploration of magnetic properties: graphene and borophene comparison*. J. Magnet. Magnet. Mater. 594 (2024), pp. 171910.

[19] R. El Fdil, Z. Fadil, E. Salmani, C.J. Raorane and H. Ez-Zahraouy, *Magnetic characteristics of the ferrimagnetic bilayer MXene-like nanostructure with interlayer exchange interactions: Monte Carlo study*. J. Magnet. Magnet. Mater. 580 (2023), pp. 170967.

[20] P. Koskinen, S. Malola and H. Häkkinen, *Evidence for graphene edges beyond zigzag and armchair*. Phys. Rev. B Condens. Matter Mater. Phys. 80(7) (2009), pp. 073401-1–073401-4.

[21] P. Koskinen, S. Malola and H. Häkkinen, *Self-passivating edge reconstructions of graphene*. Phys. Rev. Lett. 101(11) (2008), pp. 115502.

[22] D. Wei and F. Wang, *Relative stability of armchair, zigzag and reczag graphene edges on the Ru (0001) surface*. Surface Sci. 606(3-4) (2012), pp. 485–489.

[23] H.S. Moon, J.M. Yun, K.H. Kim, S.S. Jang and S.G. Lee, *Investigations of the band structures of edge-defect zigzag graphene nanoribbons using density functional theory*. RSC Adv. 6(46) (2016), pp. 39587–39594.
[24] S. Singh and I. Kaur, *Bandgap engineering in armchair graphene nanoribbon of zigzag-armchair-zigzag based Nano-FET: A DFT investigation*. Phys. E Low Dimens. Syst. Nanostruct. 118 (2020), pp. 113960.
[25] K. Gharbavi and H. Badehian, *Structural and electronic properties of armchair (7, 7) carbon nanotubes using DFT*. Comput. Mater. Sci. 82 (2014), pp. 159–164.
[26] A. Jabar and R. Masrour, *Magnetic properties of armchair graphene nanoribbons: a Monte Carlo study*. Chin. J. Phys. 64 (2020), pp. 1–8.
[27] W. Wang, Q. Li, D. Lv, R.J. Liu, Z. Peng and S. Yang, *Monte Carlo study of magnetization plateaus in a zigzag graphene nanoribbon structure*. Carbon 120 (2017), pp. 313–325.
[28] R. El Fdil, H. Sabbah, A.A. Alsayyari, Z. Fadil, C.J. Raorane, S.C. Kim and H. Ez-Zahraouy, *Monte Carlo Investigation of Hysteresis Cycles and Magnetization Plateau in C60 Fullerene-Like System Using the Blume–Emery–Griffiths Model*. Int. J. Theor. Phys. 64(4) (2025), pp. 109.
[29] Z. Fadil, C.J. Raorane, H. Sabbah, R. El Fdil, A.A. AlSayyari, S. Saadaoui and S.C. Kim, Investigating dielectric properties and vacancy effects in bismuthene nanosheets: a Monte Carlo study. J. Nanopart. Res. 27(1) (2025), pp. 1. https://doi.org/10.1007/s11051-024-06200-2.
[30] A.A.P. Khan, Z. Fadil, M. Danish, A. Khan, A.M. Asiri and C.J. Raorane, *Simulation of magnetization plateaus of stanene-like nanostructures at low temperatures*. Indian J. Phys. 98(3) (2024), pp. 913–919.
[31] N. Metropolis, A.W. Rosenbluth, M.N. Rosenbluth, A.H. Teller and E. Teller, *Equation of state calculations by fast computing machines*. J. Chem. Phys. 21(6) (1953), pp. 1087–1092.
[32] M. Blume, V.J. Emery and R.B. Griffiths, *Ising model for the λ transition and phase separation in He 3-He 4 mixtures*. Phys. Rev. A 4(3) (1971), pp. 1071–1077.
[33] J. Kple, F. Hontinfinde and E. Albayrak, *Staggered quadrupolar phase in the bond-diluted spin-1 blume-emery-Griffiths model*. Int. J. Theor. Phys. 59(12) (2020), pp. 3915–3935.
[34] Y. Al Qahoom, R. Aharrouch, K. El Kihel, H. Saadi, M. Madani and M. El Bouziani, *Blume–Emery–Griffiths model for mixed spin (1, 5/2) calculated by mean-field approximation*. Eur. Phys. J. B 96(11) (2023), pp. 142. https://doi.org/10.1140/epjb/s10051-023-00614-y.
[35] J. Sivardière and J. Lajzerowicz, *Spin-1 lattice-gas model. III. Tricritical points in binary and ternary fluids*. Phys. Rev. A 11(6) (1975), pp. 2101–2110.
[36] E.A. Bea, M.L. Trobo and A. De Virgiliis, *Critical behaviour of microemulsions: Monte Carlo simulations of the Widom model*. Phys. B Condens. Matter 553 (2019), pp. 113–119.
[37] D. Mukamel and M. Blume, *Ising model for tricritical points in ternary mixtures*. Phys. Rev. A 10(2) (1974), pp. 610–617.
[38] J. Sivardière and J. Lajzerowicz, *Spin-1 lattice-gas model. III. Tricritical points in binary and ternary fluids*. Phys. Rev. A 11(6) (1975), pp. 2101–2110.
[39] M. Ertaş, O. Canko and M. Keskin, *Dynamic phase transition in the kinetic spin-2 Blume–Emery–Griffiths model in an oscillating field*. J. Magnet. Magnet. Mater. 320(11) (2008), pp. 1765–1774.
[40] M. Ertaş and M. Keskin, *Dynamic phase transitions of the Blume–Emery–Griffiths model under an oscillating external magnetic field by the path probability method*. J. Magnet. Magnet. Mater. 377 (2015), pp. 386–394.
[41] M. Keskin and M. Ertaş, *Dynamic phase transition in the kinetic spin-5/2 Blume–Emery–Griffiths model in an oscillating external magnetic field*. Phase Trans. 83(5) (2010), pp. 349–367.
[42] M. Ertaş and M. Keskin, *Dynamic phase transitions and dynamic phase diagrams of the Blume–Emery–Griffiths model in an oscillating field: the effective-field theory based on the Glauber-type stochastic dynamics*. Phase Transit. 88(6) (2015), pp. 634–647.
[43] M.E.H.M.E.T. Ertaş and M. Batı, *Effect of odd parameter on phase diagrams and hysteresis features in a 2D kinetic spin-1 system*. Phys. A Stat. Mech. Appl. 669 (2025), pp. 130636.

[44] M. Keskin, M. Ertas and O. Canko, *Dynamic phase transition and multicritical dynamic phase diagrams of the kinetic spin-2 Ising model with repulsive biquadratic coupling under a time-dependent oscillating external field*. J. Korean Phys. Soc. 53(4) (2008), pp. 1807–1820.
[45] H. Ez-Zahraouy and A. Kassou-Ou-Ali, *Phase diagrams of the spin-1 Blume-Capel film with an alternating crystal field*. Phys. Rev. B 69(6) (2004), pp. 064415.
[46] L. Bahmad, A. Benyoussef and H. Ez-Zahraouy, *Order–disorder layering transitions of a spin-1 Ising model in a variable crystal field*. J. Magnet. Magnet. Mater. 251(1) (2002), pp. 115–121.
[47] A. Benyoussef and H. Ez-Zahraouy, *Magnetic properties of a transverse spin-1 Ising model with random crystal-field interactions*. J. Phys. Condens. Matter 6(18) (1994), pp. 3411–3420.
[48] A. Benyoussef, H. Ez-Zahraouy and M. Saber, *Magnetic properties of a transverse spin-1 Ising model with random longitudinal field*. Phys. A Statist. Mech. Appl. 198(3-4) (1993), pp. 593–605.
[49] O. Mounkachi, E. Salmani, H. El Moussaoui, R. Masrour, M. Hamedoun, H. Ez-Zahraouy and A. Benyoussef, *High blocking temperature in SnO2 based super-paramagnetic diluted magnetic semiconductor*. J. Alloys Compounds 614 (2014), pp. 401–407.
[50] N. Tahiri, H. Ez-Zahraouy and A. Benyoussef, *The effect of quantum transverse anisotropy on multilayer transitions in a spin-3/2 Blume–Capel model with RKKY interaction*. J. Superconduct. Novel Magnet. 26(10) (2013), pp. 3143–3150.
[51] L. Bahmad, A. Benyoussef and H. Ez-Zahraouy, *Monte Carlo study of order–disorder layering transitions in the Blume–Capel model*. Surface Sci. 552(1-3) (2004), pp. 1–7.
[52] N. Tahiri, H. Ez-Zahraouy and A. Benyoussef, *Multilayer transition in a spin-1 Blume—Capel model with RKKY interaction and quantum transverse anisotropy*. Chin. Phys. B 20(1) (2011), pp. 017501.
[53] I. Dani, N. Tahiri, H. Ez-Zahraouy and A. Benyoussef, *A Monte Carlo study of the spin-1 Blume–Emery–Griffiths phase diagrams within biquadratic exchange anisotropy*. Phys. A Statist. Mech. Appl. 407 (2014), pp. 295–302.
[54] H. Ez-Zahraouy, L. Bahmad and A. Benyoussef, *Phase diagrams of the Blume-Emery-Griffiths thin films*. Braz. J. Phys. 36 (2006), pp. 557–561.
[55] H. Ez-Zahraouy, *The bond diluted spin-1 Blume-Emery-Griffiths model in a transverse field*. Phys. Scripta 51(3) (1995), pp. 310–316.
[56] Z. Fadil, A. Mhirech, B. Kabouchi, L. Bahmad and W.O. Benomar, *Monte Carlo study of magnetization plateaus of a bi-layer graphyne-like structure*. Integr. Ferroelectr. 213(1) (2021), pp. 146–157.
[57] Z. Fadil, A. Mhirech, B. Kabouchi, L. Bahmad and W.O. Benomar, *Polarization and dielectric susceptibility of a monolayer coronene like nano-structure: Monte Carlo study*. Phys. Lett. A 384(30) (2020), pp. 126783.
[58] Z. Fadil, A. Mhirech, B. Kabouchi, L. Bahmad and W.O. Benomar, *Dielectric properties and compensation behaviors of a monolayer naphthalene-like nanoisland: Monte Carlo simulations*. Chin. J. Phys. 67 (2020), pp. 113–123.
[59] Z. Fadil, N. Maaouni, A. Mhirech, B. Kabouchi, L. Bahmad and W.O. Benomar, *Polarization and dielectric susceptibility of a monolayer coronene-like nano-structure: Monte Carlo study*. Int. J. Thermophys. 42(3) (2021), pp. 45.
[60] N. Maaouni, Z. Fadil, A. Mhirech, B. Kabouchi, L. Bahmad and W.O. Benomar, *Compensation behavior of an anti-ferrimagnetic core-shell nanotube like-structure: Monte Carlo Study*. Solid State Commun. 321 (2020), pp. 114047. https://doi.org/10.1016/j.ssc.2020.114047.
[61] Z. Fadil, M. Qajjour, A. Mhirech, B. Kabouchi, L. Bahmad and W. Ousi Benomar, *Blume-Capel model of a borophene layers structure with RKKY interactions: Monte Carlo simulations*. Ferroelectrics 573(1) (2021), pp. 141–153.
[62] N. Saber, Z. Fadil, A. Mhirech, B. Kabouchi, L. Bahmad and W. Ousi Benomar, *Magnetic properties and compensation temperature behaviors in the hexacene-like nanostructure: a Monte Carlo study*. J. Low Temp. Phys. 210(1) (2023), pp. 310–324.

[63] N. Saber, Z. Fadil, A. Mhirech, B. Kabouchi and L. Bahmad, *Magnetic properties and thermal behavior of the monolayer Rubrene-like nano-island: Monte Carlo simulations*. Solid State Commun. 362 (2023), pp. 115084.
[64] Z. Fadil, M. Qajjour, H. Eraki, A. Mhirech, B. Kabouchi, L. Bahmad and W. Ousi Benomar. Dielectric properties of carbon-like nanotube structure: Monte Carlo study. World Scientific Publishing Company, 2022.
[65] Z. Fadil, N. Maaouni, A. Mhirech, B. Kabouchi, L. Bahmad and W.O. Benomar, *Compensation temperature behavior in a nanotube core-shell structure with RKKY interactions: Monte Carlo simulations*. Braz. J. Phys. 50(6) (2020), pp. 716–724.

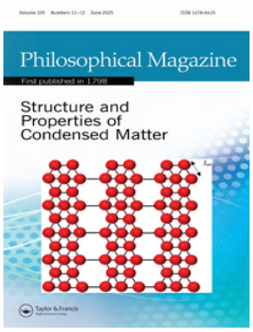

Philosophical Magazine

ISSN: 1478-6435 (Print) 1478-6443 (Online) Journal homepage: www.tandfonline.com/journals/tphm20

Investigating thermodynamic and magnetic behavior of graphullerene-like nanostructure using Monte Carlo techniques

S. Zriouel, A. Mhirech, B. Kabouchi, L. Bahmad, Z. Fadil, Fohad Mabood Husain & Chaitany Jayprakash Raorane

To cite this article: S. Zriouel, A. Mhirech, B. Kabouchi, L. Bahmad, Z. Fadil, Fohad Mabood Husain & Chaitany Jayprakash Raorane (2025) Investigating thermodynamic and magnetic behavior of graphullerene-like nanostructure using Monte Carlo techniques, Philosophical Magazine, 105:11-12, 609-622, DOI: 10.1080/14786435.2025.2449676

To link to this article: https://doi.org/10.1080/14786435.2025.2449676

PHILOSOPHICAL MAGAZINE
2025, VOL. 105, NOS. 11–12, 609–622
https://doi.org/10.1080/14786435.2025.2449676

Taylor & Francis
Taylor & Francis Group

Investigating thermodynamic and magnetic behavior of graphullerene-like nanostructure using Monte Carlo techniques

S. Zriouel[a], A. Mhirech[b], B. Kabouchi[b], L. Bahmad [b], Z. Fadil[b], Fohad Mabood Husain[c] and Chaitany Jayprakash Raorane[d]

[a]IMED-Lab, Study Group of Optoelectronic Materials, Faculty of Sciences and Technologies, Cadi Ayyad University, Marrakech, Morocco; [b]Laboratory of Condensed Matter and Interdisciplinary Sciences (LaMCScI). Research Unit Labelled CNRST, URL-CNRST-17. Faculty of Sciences, Mohammed V University in Rabat, Rabat, Morocco; [c]Department of Food Science and Nutrition, College of Food and Agriculture Sciences, King Saud university, Riyadh, Saudi Arabia; [d]School of Chemical Engineering, Yeungnam University, Gyeongsan, Republic of Korea

ABSTRACT

In the world of carbon-based materials, the effective synthesis of a graphullerene-like nanostructure with remarkable features is a noteworthy accomplishment. This insight holds great promise for advancing the development of a new category of materials. In this study, we examined the thermodynamic characteristics and magnetocaloric effects of a structure resembling graphullerene using Monte Carlo simulations. The current study provides a detailed analysis of how Hamiltonian parameters impact the thermodynamic properties and magnetocaloric quantities of the system. Moreover, our findings indicate that adjusting the magnetic field not only allows for critical regulation of temperature but also has a notable impact on magnetocaloric characteristics. This includes changes in magnetic entropy and the relative cooling capacity. Based on our results, it is strongly suggested that the graphullerene-like nanostructure holds great promise as a candidate for applications in magnetic refrigeration.

ARTICLE HISTORY
Received 7 June 2024
Accepted 27 December 2024

KEYWORDS
Monte Carlo simulations; graphullerene; magnetocaloric properties; square hysteresis loops; magnetic entropy change; relative cooling power (RCP)

1. Introduction

The field of magnetic nanostructures (0D, 1D, and 2D) appears to be becoming increasingly interesting, specifically a variety of nanostructures – like nanobelts [1], nanorods [2], nanowires [3,4], nanofilms [5], nanotubes [6,7], and nano-graphene [8] and fullerene-like structures [9]. It has been shown that these systems differ significantly from 3D (bulk) materials in terms of their physical properties, which have been extensively studied both theoretically and

CONTACT Z. Fadil fadilzakaria604@gmail.com Laboratory of Condensed Matter and Interdisciplinary Sciences (LaMCScI). Research Unit Labelled CNRST, URL-CNRST-17. Faculty of Sciences, P.O. Box 1014, Mohammed V University in Rabat, Morocco; Chaitany Jayprakash Raorane chaitanyaraorane22@ynu.ac.kr School of Chemical Engineering, Yeungnam University, Gyeongsan 38541, Republic of Korea

experimentally [10]. Two-dimensional materials, such as graphene [11,12], have made possible by the discovery of graphene a whole new world of materials that can separate gases, catalysis, inert coatings, and supporting membranes, among other applications [13,14]. The most used two-dimensional materials today are composed of periodic network structures formed from monatomic structural units [8,15]. The idea of constructing 2*D* structures using advanced structural units, like clusters, has not been extensively explored. Nanoclusters, also known as artificial atoms, can bond similarly to atoms and create sophisticated structures [16,17]. Two-dimensional structures assembled from nanoclusters are anticipated to exhibit exceptional topologies and unique characteristics, but no such structures have been reported thus far. Fullerene (C_{60}), a well-known carbon cluster, can undergo polymerisation under extremely high pressure, resulting in the formation of a layered structure of C_{60} through inter-cluster covalent bonds [18]. The polymeric C_{60} layer displays a consistent undulating topology in a two-dimensional plane, featuring carbon clusters organised in a repetitive arrangement. Furthermore, this layer possesses intriguing electronic [19,20] and magnetic [21] characteristics. However, the low yield and metastability of atomic-scale 2*D* polymeric C_{60} under ambient atmospheric pressure pose significant challenges in obtaining a stable and ordered structure, which impedes the study of its intrinsic properties.

Recently, a novel type of carbon has been found through the combination of two existing carbon forms [22,23]. The first one is the two-dimensional array of carbon atoms called graphene, which generated much excitement and speculation after its discovery in 2004 [8]. The second is fullerene [9], a carbon structure that forms a ball shape. The outcome of linking carbon spheres in a two-dimensional pattern is called graphullerene, while its three- dimensional solid form is known as graphullerite [22,23]. Unlike graphene and other two-dimensional materials that have specific properties due to their repeating elements and limited bonding geometries [8], graphullerene's super atomic structure lends it a high level of modularity. Graphullerene is made up of fullerene subunits that are arranged hexagonally and connected covalently. It is synthesised through a chemical vapour transport approach, wherein crystals of magnesium-doped fullerene polymers are first grown. Subsequently, single sheets of graphullerene are obtained by exfoliating them from the bulk material, followed by removal of magnesium using dilute acid [23]. Unlike other carbon-based materials, graphullerene exhibits a distinctive set of properties. There is a 1.6 eV electron transport band gap in this new semiconductor, as well as a high crystallinity and good thermodynamic stability [24,25]. Furthermore, it exhibits anisotropy in plane and anisotropic phonon modes and conductivity [25,26]. Carbon materials with medium band gaps and unique topologies are promising platforms for two-dimensional electronic devices due to the unique characteristics they possess. Undoubtedly, the integration of graphullerenes in novel optical and electronic devices will exhibit greater resistance to elevated currents

and temperatures, making them effective heat dissipators. This feature of thermal conductivity remains crucial in the progression of semiconductors, as more transistors are squeezed into smaller spaces. It is probable that graphullerene will supersede fullerene in numerous forthcoming solar, wind, battery, and sensor products, until the next significant advancement in carbon materials [25]. This newly discovered carbon form, known for its lightweight and high strength, is projected to enhance the durability and capability of photonic and electronic devices due to its tunable superlattice structure, which aligns with the direction of superconductors and electronics. The discovery of graphullerene implies that there is a vast potential for creating numerous other nanoscale hybrid carbon allotropes through synthetic design. Moreover, Monte Carlo simulations have been widely used to investigate the magnetic properties of various systems, such as the compensation and critical behaviour of Ising mixed-spin (1-1/2-1) three-layer systems with cubic structure [27], and ferrimagnetic triangular nanotubes with core-shell structure [28]. Detailed studies have explored compensation temperatures and phase diagrams in systems like mixed spin-1 and spin-1/2 Ising models on checkerboard square structure [29], as well as mixed spin-1/2 and spin-1 ferrimagnetic-centered rectangular structure [30]. These simulations provide insights into the complex magnetic behaviours and transitions in these systems.

On the other hand, there are various studies of magnetocaloric properties of 2D and 3D structures, the underlying physical mechanisms of the magnetocaloric effect (MCE) remain inadequately comprehended, despite the vast amount of experimental data available. Investigating magnetocaloric effect in carbon-based compounds, which frequently exhibit magnetic traits at the molecular level, assumes great significance in resolving fundamental queries pertaining to magnetism and condensed matter physics [9]. This is related to the challenge of procuring insights into magnetic phase transitions and the magnetic state of matter. At temperatures nearing room conditions, beyond the range of magnetic transitions, there is a significant and even giant magnetocaloric effect (MCE) in various substances, including graphene [31], high-spin complexes of porphyrins/phthalocyanines that are paramagnetic [32], polycaprolactone/MSMA composites for magnetic refrigeration applications [33]. Our current research is profoundly influenced by the compound, as we aim to conduct a comparative theoretical examination of its magnetic and magnetocaloric properties. Specifically, we are investigating the impact of various Hamiltonian parameters on thermodynamic quantities of graphullerene-like nanostructures, such as magnetisation, susceptibility, specific heat, and hysteresis loops, to explore its potential for significant applications. To address these inquiries, we employ Monte Carlo simulations, which allow us to tackle intriguing scientific questions that may be experimentally infeasible. Moreover, we will examine the magnetocaloric behaviour of graphullerene-like nanostructures in detail. Since the carbon atoms in the graphullerene structure are inherently

non-magnetic, each carbon atom in the structure has been replaced by an atom possessing a magnetic spin of *S*–1 in our approach. This choice balances computational feasibility with the ability to capture key magnetic characteristics, including magnetisation, susceptibility, and hysteresis behaviour. By introducing this modification, we effectively transform the graphullerene into a theoretical spin system, enabling comprehensive Monte Carlo simulations under varying parameters, such as external magnetic fields, exchange coupling constants, and crystal field effects.

The structure of this paper was outlined as follows: Section 2 presents the model and provides a detailed description of the formulation and methodology employed in our research. In Section 3,4 and 5 we presented and discussed the results obtained from our study. Finally, in the last section, we summarised the most significant findings detailed in this work and draw conclusions based on our research outcomes.

2. Model and technique

Using the Blume Capel model, we evaluated the magnetic and magnetocaloric properties of graphullerene-like nanomaterials [34]. A plane is formed by the covalent connections of each cluster cage of C_{60}. The crystal structure of the graphullerene-like nanostructure is schematically illustrated in Figure 1. Furthermore, according to the statistics of Fabian and Leonhardt, error bars are applied in all figures [35].

The Hamiltonian characterising our model can be expressed as follows:

$$\mathcal{H} = -J \sum_{\langle i,j \rangle} S_i S_j - h \sum_i S_i - \Delta \sum_i S_i^2. \tag{1}$$

- **Exchange Interaction** $-J \sum_{\langle i,j \rangle} S_i S_j$: This term represents the interaction between neighbouring spins S_i and S_j. All the spins were assumed to take values of $S = \pm 1; 0$. The exchange interaction J promotes alignment (or anti-alignment) of neighbouring spins, depending on whether it is positive (ferromagnetic) or negative (antiferromagnetic). In the context of graphullerene, a nanostructure composed of magnetic atoms, this term describes how the spins of the atoms interact with each other, influencing the overall magnetic properties of the material.
- **External Magnetic Field** $-h \sum_i S_i$: This term corresponds to the effect of an external magnetic field h on the spins S_i. The magnetic field tends to align the spins in its direction, which changes the system's overall magnetic state. For graphullerene, this term models the influence of an external field on the magnetic structure of the atoms, thereby altering the spin configuration.

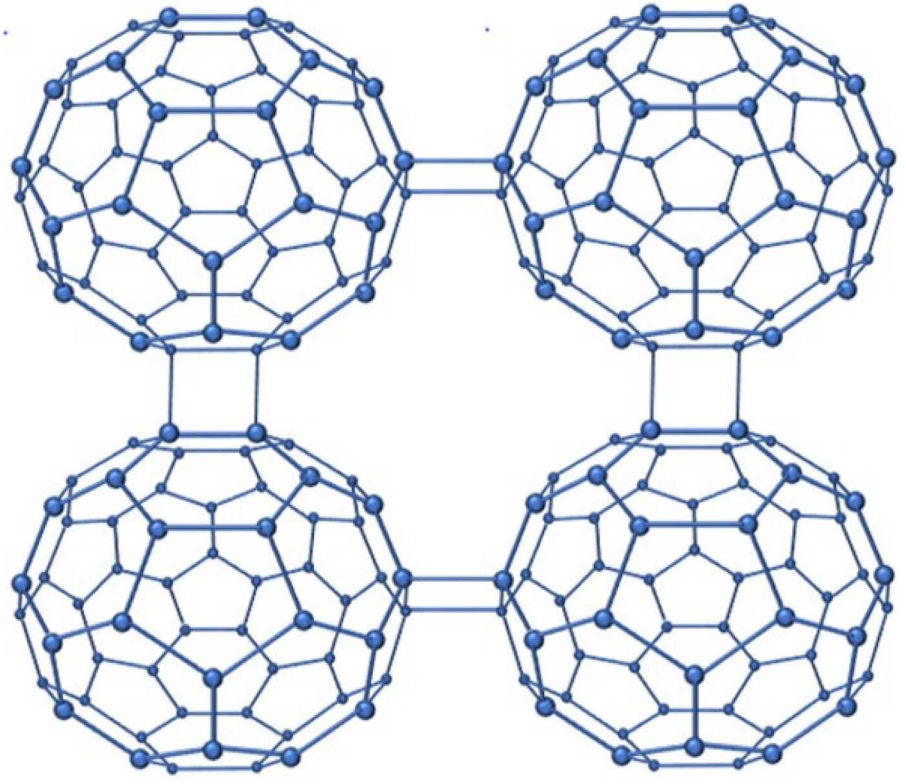

Figure 1. Schematic presentation of graphullerene-like nanostructure.

- **Crystal Field Parameter** – $\sum_i S_i^2$: This term represents the effect of the crystal field Δ, which modifies the spin energy depending on the local environment. In a nanostructure like graphullerene, the atoms are subject to forces from other atoms in the structure, and this term captures the effect of these forces on the spin energy levels. The parameter Δ determines the strength of this interaction.

It is worth mentioning that in subsequent calculations, the coupling J was taken as a unit of the system, i.e. $J = 1$, for ease of comparison and analysis. To simulate the system, we used the Metropolis Monte Carlo simulation algorithm [32], generating configurations by sequentially selecting lattice sites and attempting single-spin flips. The acceptance or rejection of these flips was determined based on the Metropolis algorithm.

Since graphullerene is a finite system, periodic boundary conditions (PBC) may not be the most suitable approach for this situation. Free boundary conditions are more effective in capturing the intrinsic characteristics of an individual graphullerene. To address this, we applied free boundary conditions to the overall graphullerene structure, while periodic boundaries were used for

each fullerene unit within the structure. This combination is essential for producing accurate results. The periodic boundaries within each fullerene allow for a more precise representation of internal properties, while the free boundaries for the overall structure account for edge effects. Additionally, because the system size ($N = 240$) is sufficiently large, edge effects and boundary conditions have a minimal impact on the properties of interest, allowing us to disregard finite-size effects.

We have run our simulations using a total of 10^6 Monte Carlo steps per spin to collect data. To ensure accuracy, we excluded the first 10^5 Monte Carlo steps from the data collection process. These initial steps allowed the system to reach thermal equilibrium, ensuring that the subsequent data accurately reflected the steady state of the system under the given physical parameters.

Our programme calculates the internal energy per site E:

$$E = \frac{1}{N}\langle \mathcal{H} \rangle \tag{2}$$

and the specific heat (C_m):

$$C_m = \frac{\beta^2}{N}\left(\left\langle E^2 \right\rangle - \langle E \rangle^2\right) \tag{3}$$

with $N = 240$ representing the number of spins in the system, and β defined $\beta = \frac{1}{k_B T}$, where T denotes the absolute temperature and k_B represents the Boltzmann's constant. In our calculations, we have set the value of Boltzmann's constant to be 1.

Several parameters, such as magnetisation and susceptibility, were also calculated to verify the accuracy of our calculations, including internal energy and specific heat. Magnetisation per site M, and its corresponding susceptibility χ were calculated as follows:

$$M = \frac{1}{N}\sum_{i=1}^{N_S}\langle S_i \rangle, \tag{4}$$

$$\chi = \beta\left(\langle M^2 \rangle - \langle M \rangle^2\right) \tag{5}$$

We also analyse the fourth-order cumulant of order parameter, the Binder cumulant [36], defined by:

$$U = 1 - \frac{\left\langle M^4 \right\rangle}{3\langle M^2 \rangle^2}, \tag{6}$$

In order to determine if this material is suitable for magnetic refrigeration, the magnetocaloric parameters, namely the magnetic entropy change ΔS and

relative cooling power *RCP*, can be calculated using the following equations:

$$\Delta S\,(T, h) = \int_0^h \left(\frac{\partial M}{\partial T}\right)_{h_i} dh_i, \tag{7}$$

$$RCP = \int_{T_1}^{T_2} \Delta S\,(T) dT, \tag{8}$$

Where $\left(\frac{\partial M}{\partial T}\right)_{h_i}$ represents the thermal magnetisation in a fixed magnetic field. T_1 and T_2 represent, respectively, the lower and upper temperatures that were associated with the two ends of the half maximum of $\Delta S_{\max}$.

It was interesting to utilise the reduced physical parameters in order to go beyond the classical energy and temperature units (*K*, *eV*, or Joule) in calculations. The reduced physical parameters were dimensionless. The reduced physical parameters will be used as follows for simplicity: $t = \mathrm{T}/J$, $h_r = \mathrm{h}/J$, and $\delta = \Delta/J$.

3. Results and discussions

In this section, we employed Monte Carlo simulations to investigate how different parameters of the Hamiltonian impact the magnetic and magnetocaloric properties of the system. We initiated our calculations by analysing the thermal variations of the total magnetisation and the corresponding susceptibility, which were crucial for characterising phase transitions and identifying the critical temperature. To assess the feasibility of using graphullerene for magnetic refrigeration, we computed the isothermal magnetic entropy change ΔS from the magnetisation isotherm $M\,(h_r, t)$ curves. Finally, we analysed the variations of the hysteresis behaviour as a function of temperature.

3.1. Magnetic properties

In the beginning, we investigated the influence of temperature on magnetisation and its corresponding susceptibility. 2. Phase transitions were examined in this study in order to demonstrate that there exists a critical temperature at which phase transitions occur. Figure 2a and b demonstrate how magnetic susceptibility varies with temperature. Temperature t causes the total magnetisation to decrease gradually from its saturation value to zero as it rises.

As the critical temperature approaches, a single peak is visible in the susceptibility χ curve. In accordance with standard findings, thermal fluctuations drove the phase transition between ferromagnetic and paramagnetic materials. To confirm the stability of the above-mentioned second-order phase transition

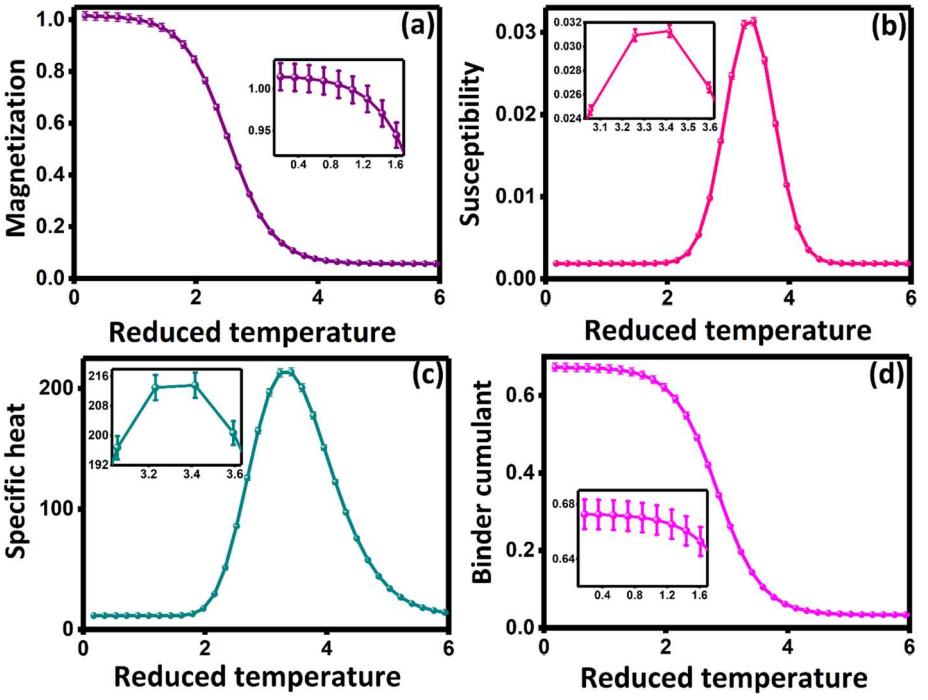

Figure 2. Temperature dependence of **(a)** magnetisation, **(b)** susceptibility, **(c)** specific heat, and **(d)** Binder cumulant for $\delta = 0$ and $h_r = 0$.

in the system, Figure 2c and d displayed the specific heat and Binder cumulant as a function of temperature, respectively. It was noteworthy that the behaviour of the specific heat corresponds evidently with that of the susceptibility shown in Figure 2b. Specifically, in the proximity of the critical temperature, the specific heat exhibits a peak and then decreases with increasing temperature, which were indicative of second-order phase transition characteristics. Consequently, the critical temperature obtained from the specific heat curve aligns well with that estimated from the magnetisation and susceptibility curves in Figure 2a and b. Moreover, to verify the correctness of the obtained critical temperature t_C, we have plotted the temperature dependence of the Binder cumulant U for the system in Figure 2d. As the temperature of the system rises, the Binder cumulant U consistently decreases from its saturated value to a small constant at the critical temperature, indicating a second-order phase transition from a ferromagnetic phase to a paramagnetic phase. As shown in the inset figure, the critical temperature t_C derived from the Binder cumulant U matches well with the estimate based on the susceptibility, providing clear evidence of the validity of the numerical outcomes.

To examine how crystal field affects magnetisation, susceptibility, and specific heat, we have illustrated the findings in Figure 3a–c, respectively. As shown in Figure 3a, the magnetisation remains constant for $\delta < -4$.

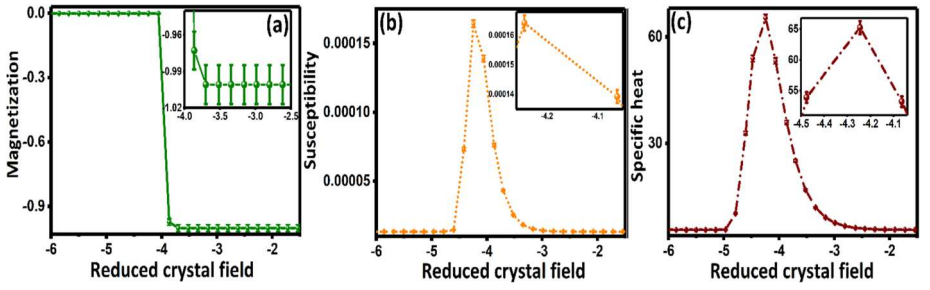

Figure 3. Crystal field dependence of **(a)** magnetisation, **(b)** susceptibility, and **(c)** specific heat at a fixed value of $t = 0.1$ and $h_r = 0$.

However, as soon as the crystal field reaches its critical value of $\delta_C = -4$, the magnetisation decreases discontinuously to saturate at a minimal value of $M = -1$ for $\delta > -4$. Therefore, the system undergoes a first-order transition at the critical crystal field value. This behaviour was supported by the curves of susceptibility and specific heat, which show pronounced peaks, indicating a first-order phase transition from an antiferromagnetic phase to a ferromagnetic phase at critical crystal field value.

In Figure 4, we presented the magnetisation M and the specific heat in relation to temperature for different values of external magnetic field, namely $h_r = 0$, 1, 2, and 3. All the magnetisation curves show a decrease from their saturation value $M = 1$ to small constant magnetisation as temperature T increases. Furthermore, with increasing the magnetic field, the slope of the magnetisation curves becomes less significant. On the other hand, the specific heat curves exhibit distinct peaks at critical temperatures, providing evidence of a second order phase transition. Furthermore, the height of the peaks decreases and moves towards higher temperatures when the magnetic field in the system increases. This behaviour can be attributed to the significant influence of the magnetic field on the alignment of spins in the system.

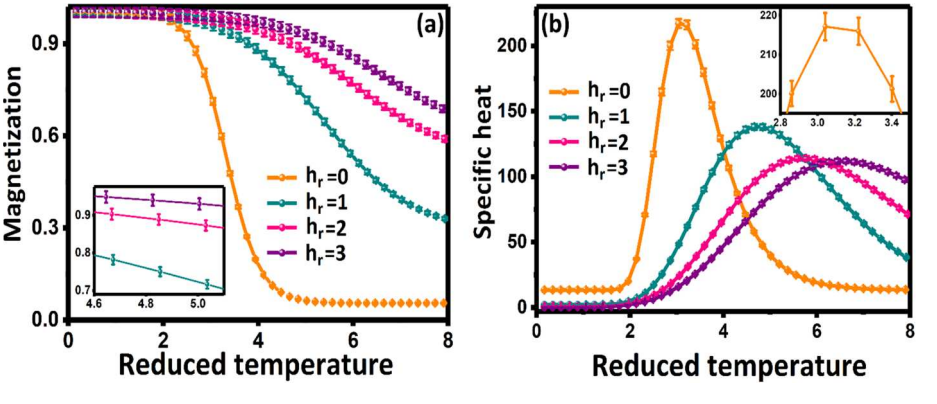

Figure 4. Magnetisation and specific heat versus temperature for various values of external magnetic field *hr* for $\delta = 0$.

3.2. Magnetocaloric properties

After completing these calculations, we examined the magnetocaloric properties of graphullerene-like nanostructure. Magnetic entropy change (ΔS) and relative cooling power (RCP) were used to characterise magnetocaloric effect (MCE). Based on the external magnetic field, graphene-like nanostructures exhibit varying magnetic entropy changes with temperature.

As can be seen in Figure 5, the value of ΔS increases with temperature until reaching its maximum value, then decreases near the critical temperature. As the magnetic field is enhanced, the maximum value of magnetic entropy increases due to the compound's second-order phase transition nature. Due to the alignment of the spins, when there is a higher external magnetic field, the system will be more ordered. A magnetic field external to a system enhances its magnetocaloric effect. Additionally, ΔS remains negative throughout the temperature range, indicating a magnetocaloric effect in the graphullerene-like nanostructure, which heats up when exposed to a magnetic field and cools down when removed. A refrigeration application may be possible with this material. In addition to the magnetic entropy change, relative cooling power (RCP) is another important factor that impacts magnetocaloric efficiency. Refrigeration systems use the RCP to determine how effectively heat is transferred between hot and cold reservoirs. Monte Carlo simulations were conducted to determine the behaviour of this factor, and the results are shown in Figure 5b. With increasing magnetic field values, the RCP increases linearly. As shown in Figure 5a, the linearity increased in correlation with the maximum entropy change. A magnetic refrigeration application could be possible with the material being studied based on these results.

Indeed, graphullerene may be a good candidate for applications in magnetic refrigeration, based on its magnetocaloric effects (MCE). These applications mainly concern systems capable of cooling efficiently by exploiting magnetic

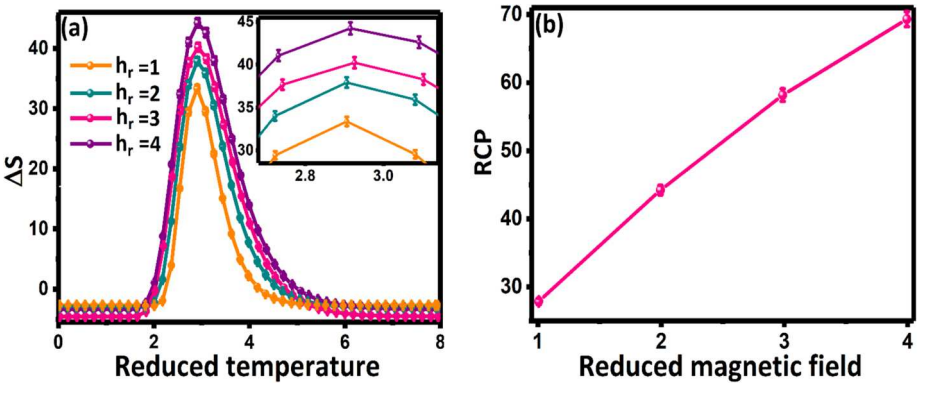

Figure 5. **(a)** Temperature dependence of magnetic entropy changes for several reduced magnetic fields, **(b)** the external magnetic field dependence of the *RCP* for $\delta = 0$.

entropy variations induced by an external magnetic field. However, as the results of the study show, the maximum value of the magnetocaloric effect is reached at very low temperatures. Such a material could be used in environments requiring low-temperature cooling, such as sophisticated medical devices like the superconducting magnets used in magnetic resonance imaging (MRI) [37,38]. However, their use in room-temperature contexts, common for domestic or industrial refrigeration, would require further adjustments to extend their effective temperature range.

3.3. Hysteresis cycles

In this subsection, we also explored how the temperature influences the hysteresis loops of graphullerene-like nanostructure, elucidating their correlation with this factor. In Figure 6, we analysed the hysteresis curves of a graphullerene-like nanostructure at specific temperatures. The curves demonstrated that all the magnetisation axes and external magnetic field hysteresis loops exhibit clear symmetry. At low temperature, the hysteresis loop adopts a square shape, indicating that the normal orientation acts as an easy axis. Consequently, the remanent magnetisation was equivalent to the saturation magnetisation. These results suggest that spins align more easily along magnetic fields as temperatures near ground state. The quadratic nature of hysteresis curves makes materials such as graphullerene highly appropriate for applications in high-energy storage capacitors. It was also noteworthy that the hysteresis loop area

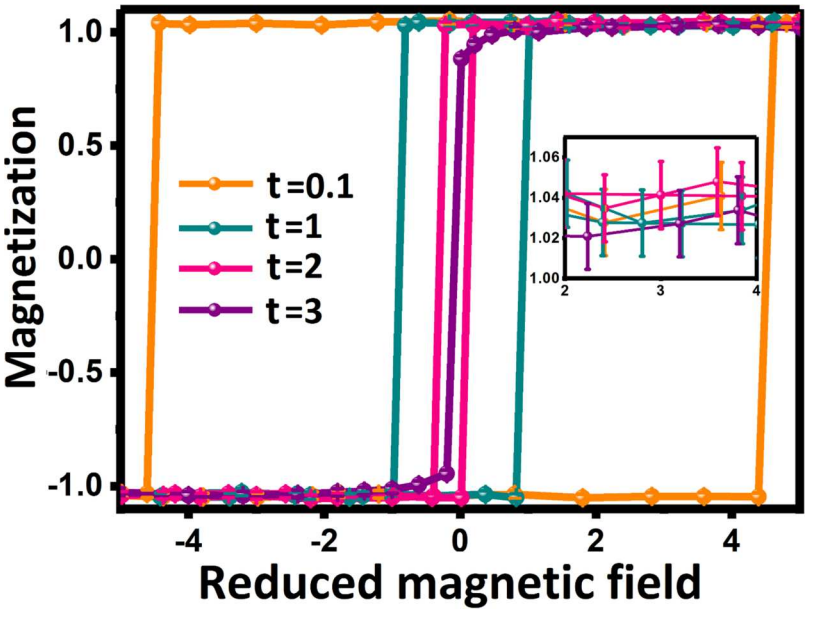

Figure 6. Magnetic hysteresis loops at different temperature values $t = 0.1$, 1, 2, and 3 for $\delta = 0$.

diminishes as the temperature increases, eventually vanishing as the temperature reaches its critical value t_C. Indeed, as the temperature is increased ($t = 3$), the hysteresis curve exhibits a linear behaviour, indicating that higher temperatures disrupt the system and lead to paramagnetic hysteresis. Ultimately, it was found that the coercive field, which indicates the field required to alter the magnetisation's sign, dwindles with an upsurge in temperature. This outcome corroborates the theoretical analysis of graphone nanoribbon [15].

4. Conclusions

In summary, we have employed Monte Carlo simulations with the standard Metropolis algorithm to investigate the magnetic, hysteretic, and magnetocaloric characteristics of graphullerene-like nanostructure. We calculated magnetic parameters, susceptibilities, specific heats, hysteresis loops, magnetic entropy changes, and relative cooling power (RCP) based on the system parameters. First, we have examined the impact of reduced temperature on magnetisation and its corresponding susceptibility to identify the type of phase transitions which take place within the system. Subsequently, we have presented the magnetic entropy change and the *RCP*, followed by an analysis of the hysteresis loops for the system. Our study has revealed several characteristic behaviours in the system. Furthermore, our results have indicated that the increase in the magnetic field will obviously lead to the increase in the maximum magnetic entropy change (ΔS max) and relative cooling power (*RCP*). Ultimately, our investigation has revealed that the ferromagnetic hysteresis loops exhibit a transition in shape from square to anhysteretic curves at specific temperature values. This finding provides important insights into the system's hysteretic behaviour and its dependence on temperature, suggesting that the system's hysteretic properties were influenced by temperature changes in a significant manner. All these results have significant implications for controlling the magnetic and magnetocaloric properties of graphullerene-like nanostructure through modulation of magnetic fields and temperature, which was crucial for potential magnetic refrigeration applications. On the other hand, this knowledge can contribute to the development of efficient and functional graphullerene-based devices with desired magnetic and magnetocaloric properties for various applications in nanotechnology and related fields.

Disclosure statement

No potential conflict of interest was reported by the author(s).

Funding

The authors thank the Researchers Supporting Project Number (RSPD2025R729), King Saud University, Riyadh, KSA. This research was supported by the Basic Science Research

Program through the National Research Foundation of Korea (NRF) funded by the Ministry of Education (2020R1I1A3052258).

Data and code availability

The investigation was made by Monte Carlo simulations under the Metropolis algorithm by a Fortran code.

ORCID

L. Bahmad http://orcid.org/0000-0003-0526-7145

References

[1] R.Q. Song, A.W. Xu, and S.H. Yu, J. Am. Chem. Soc. 129 (2007), p. 4152.
[2] E. Tirosh and G. Markovich, Adv. Mater. 19 (2007), p. 2608.
[3] M.J. Benitez, O. Petracic, E.L. Salabas, F. Radu, H. Tu¨ysu¨z, F. Schu¨th, and H. Zabel, Phys. Rev. Lett. 101 (2008), p. 097206.
[4] H. Gao, M. Staruch, M. Jain, P.X. Gao, P. Shimpi, Y. Guo, W. Cai, and H.J. Lin, Appl. Phys. Lett. 98 (2011), p. 123105.
[5] Y. Benhouria, I. Essaoudi, A. Ainane, and R. Ahuja, Chin. J. Phys. 53 (2015), p. 187.
[6] N. Maaouni, Z. Fadil, A. Mhirech, B. Kabouchi, L. Bahmad, and W. Ousi Benomar, Solid State Commun. 321 (2020), p. 114047.
[7] X.S. Qi, W. Zhong, Y. Deng, C.T. Au, and Y.W. Du, Carbon. N. Y. 48 (2010), p. 365.
[8] S. Zriouel, J. Magn. Magn. Mater. 493 (2020), p. 165711.
[9] A. Mhirech, S. Aouini, A. Alaoui-Ismaili, and L. Bahmad, J. Low. Temp. Phys. 192 (2018), pp. 65–74.
[10] V. Skumryev, S. Stoyanov, Y. Zhang, G. Hadjipanayis, and D. Givord, J. Nogues, Nature 423 (2003), p. 850.
[11] C. Lee, X. Wei, and J.W. Kysar, J. Hone. Sci. 321 (2008), pp. 385–388.
[12] Y. Zhang, Y.-W. Tan, H.L. Stormer, and P. Kim, Nature 438 (2005), pp. 201–204.
[13] A.K. Geim, Science 324 (2009), pp. 1530–1534.
[14] J.N. Coleman, M. Lotya, A. O'Neill, S.D. Bergin, P.J. King, U. Khan, K. Young, A. Gaucher, S. De, R.J. Smith, I.V. Shvets, S.K. Arora, G. Stanton, H.-Y. Kim, K. Lee, G.T. Kim, G.S. Duesberg, T. Hallam, J.J. Boland, J.J. Wang, J.F. Donegan, J.C. Grunlan, G. Moriarty, A. Shmeliov, R.J. Nicholls, J.M. Perkins, E.M. Grieveson, K. Theuwissen, D.W. McComb, P.D. Nellist, and V. Nicolosi, Science 331 (2011), pp. 568–571.
[15] S. Zriouel, Mater. Sci. Eng. B 267 (2021), p. 115087.
[16] H.-J. Zhai, Y.-F. Zhao, W.-L. Li, Q. Chen, H. Bai, H.-S. Hu, Z.A. Piazza, W.-J. Tian, H.-G. Lu, Y.-B. Wu, Y.-W. Mu, G.-F. Wei, Z.-P. Liu, J. Li, S.-D. Li, and L.-S. Wang, Nat. Chem. 6 (2014), pp. 727–731.
[17] P. Jena and Q. Sun, Chem. Rev. 118 (2018), pp. 5755–5870.
[18] V.D. Blank, S.G. Buga, G.A. Dubitsky, N. R. Serebryanaya, M.Y. Popov, and B. Sundqvist, Carbon. N. Y. 36 (1998), pp. 319–343.
[19] S. Okada and S. Saito, Phys. Rev. B 59 (1999), pp. 1930–1936.
[20] C.H. Xu and G.E. Scuseria, Phys. Rev. Lett. 74 (1995), pp. 274–277.

[21] T.L. Makarova, B. Sundqvist, R. Höhne, P. Esquinazi, Y. Kopelevich, P. Scharff, V.A. Davydov, L.S. Kashevarova, and A.V. Rakhmanina, Nature 413 (2001), pp. 716–718.
[22] L. Hou, X. Cui, B. Guan, S. Wang, R. Li, Y. Liu, D. Zhu, and J. Zheng, Nature 606 (2022), pp. 507–510.
[23] E. Meirzadeh, A.M. Evans, M. Rezaee, M. Milich, C.J. Dionne, T.P. Darlington, S.T. Bao, A.K. Bartholomew, T. Handa, D.J. Rizzo, R.A. Wiscons, M. Reza, A. Zangiabadi, N. Fardian-Melamed, A.C. Crowther, P.J. Schuck, D.N. Basov, X. Zhu, A. Giri, P.E. Hopkins, P. Kim, M.L. Steigerwald, J. Yang, C. Nuckolls, and X. Roy, Nature 613 (2023), pp. 71–76.
[24] G. Shen, L. Li, S. Tang, J. Jin, X. Chen, and Q. Peng, Crystals. (Basel) 13 (2023), p. 224.
[25] S. Zhao, X. Zhang, Y. Ni, Q. Peng, and Y. Wei, Carbon. N. Y. 202 (2023), pp. 118–124.
[26] B. Mortazavi, F. Shojaei, and X. Zhuang, Mater. Today Nano. 21 (2023), p. 100280.
[27] M. Gharaibeh, A. Obeidat, M. Qaseer, and M. Badarneh, Phys. A. 550 (2020), p. 124147.
[28] M. Gharaibeh, S. Alqaiem, A. Obeidat, A. Al-Qawasmeh, S. Abedrabbo, and M. Badarneh, Phys. A. 584 (2021), p. 126394.
[29] M. Gharaibeh, M. Badarneh, S. Alqaiem, A. Obeidat, M. Qaseer, and J. Magn, Magn. Mater. 540 (2021), p. 168458.
[30] A. Obeidat, M. Hassan, and M. Badarneh, IEEE Trans. Magn. 55 (2019), pp. 1–5.
[31] V.V. Korolev, A.G. Ramazanova, O.V. Balmasova, A.Y. Soloveva, E.Y. Buslaeva, S.P. Gubin, and M.S. Gruzdev, J. Magn. Magn. Mater. 476 (2019), pp. 604–607.
[32] V. V. Korolev, T. N. Lomova, D. V. Korolev, A. G. Ramazanova, E. G. Mozhzhukhina and E. N. Ovchenkova, *New Nanoscaled Paramagnetic Complexes (NPCs) Based on Porphyrins/Phthalocyanines for Environmental Chemistry*, in *Advanced Environmental Analysis: Applications of Nanomaterials*. Royal Society of Chemistry, Cambridge, 2016, pp. 14–47.
[33] V. Sánchez-Alarcos, D.L.R. Khanna, P. La Roca, V. Recarte, F.D. Lambri, F.G. Bonifacich, O.A. Lambri, I. Royo-Silvestre, A. Urbina, and J.I. Pérez-Landazábal, Polym. Compos. 46 (2025), pp. 427–437.
[34] W. Jiang, Y.N. Wang, A.B. Guo, Y.Y. Yang, and K.L. Shi, Carbon. N. Y. 110 (2016), pp. 41–47.
[35] K. Fabian and R. Leonhardt, Earth Planet. Sci. Lett. 297 (2010), p. 84.
[36] K. Binder, Z. Phys. B 43 (1981), p. 119.
[37] Y.E. Lvovsky, W. Stautner, and T. Zhang, Supercond. Sci. Technol. 26(9) (2013), p. 093001.
[38] A. Raza and S.S. Ali, Mater. Res. Found. 132 (2022), pp. 230–255.

PHILOSOPHICAL MAGAZINE

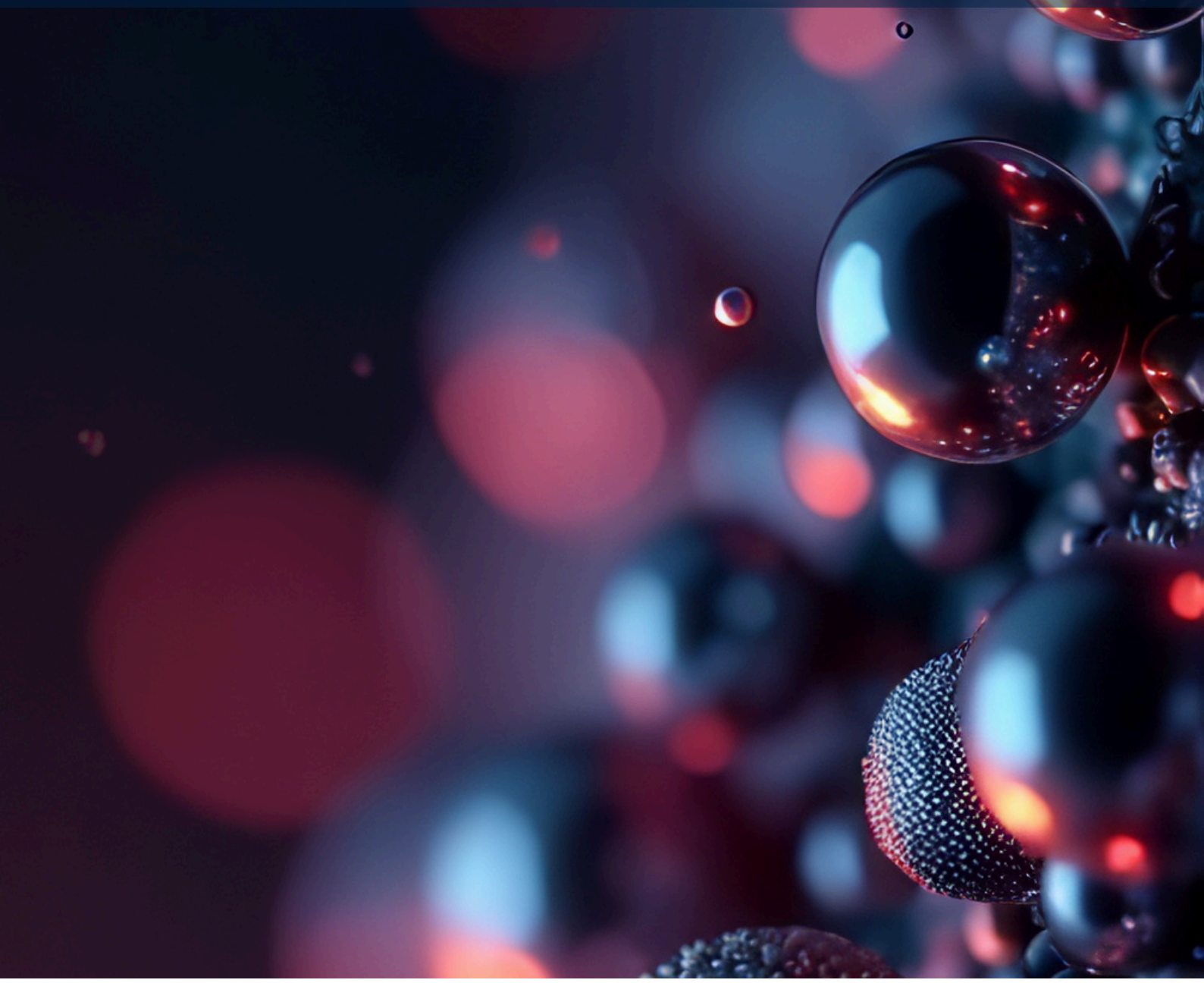

Contact us

Editorial Department | digitaleditor@philosophicalmagazine.com

Taylor & Francis
by informa